

Experimental investigation of the Nernst effect for thermomagnetic applications



Md Sabbir Akhanda

PhD Dissertation

Charles L. Brown Department of Electrical and Computer Engineering,
University of Virginia

Advisor: Dr. Mona Zebarjadi

May, 2024

Declaration

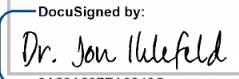
This is to certify that the thesis entitled "Experimental Investigation of the Nernst Effect for Thermomagnetic Applications" was conducted by Md Sabbir Akhanda in the Department of Electrical and Computer Engineering at the University of Virginia.

Neither this dissertation nor any part of this work has been submitted elsewhere for the award of a degree.

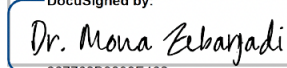
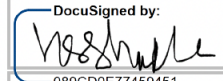
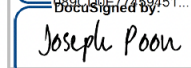
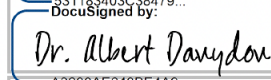
Approval Statement

This is to certify that the thesis submitted by Md Sabbir Akhanda, entitled "*Experimental Investigation of the Nernst Effect for Thermomagnetic Applications,*" has been approved by the committee for the partial fulfillment of the requirements for the degree of PhD in the Department of Electrical Engineering at the University of Virginia, in April 2024.

Committee Chair

Name	Department/ School/ Institution*	Signature
Dr. Jon Ihlefeld	MSE/ECE/SEAS/UVA	<small>DocuSigned by:</small>  <small>3A29A637EA8942C...</small>

Committee Members

Name	Department/ School/ Institution*	Signature
Dr. Mona Zebarjadi	ECE/SEAS/UVA	<small>DocuSigned by:</small>  <small>267763B9008E462...</small>
Dr. Nikhil Shukla	ECE/MSE	<small>DocuSigned by:</small>  <small>089C80E77459451...</small>
Joseph Poon	Physics	<small>DocuSigned by:</small>  <small>531183403C38479...</small>
Dr. Albert Davydov	NIST/MSED	<small>DocuSigned by:</small>  <small>A3288AE648BE4A9...</small>

* School or Institution if not School of Engineering

“To my parents, whose endless love and sacrifices have made my academic journey possible”

“To my dearest wife, Tonni. In you, I have found the perfect friend to walk alongside through life’s obstacles and joys.”

“To my little daughter, Fatiha. I love you more than you will ever be able to comprehend.”

“To Shorna, the sweetest little sister anyone can ever hope for.”

Acknowledgement

Reflecting on my time at the University of Virginia, I am overwhelmed with gratitude for the mentors, collaborators, family, and friends who stood by me during this journey. Their unwavering support was the cornerstone of my success, and I deeply appreciate their guidance and encouragement.

First and foremost, I would like to express my immense gratitude towards my advisor, Dr. Mona Zebarjadi. It has been my privilege to have her as my mentor. Throughout this academic journey, she has exemplified unwavering support, exceptional patience, and technical expertise, guiding me through challenges with grace and wisdom. I am truly thankful for her professionalism, and commitment to teaching me the process of understanding, analyzing, and solving complex problems. While her advisory skills were top-notch, it was her exceptional qualities as a person that left an even greater impact on me. I became a fan of her for life.

I extend my thanks to my esteemed PhD committee members, Dr. Jon Ihlefeld, Dr. Nikhil Shukla, Dr. Joe Poon, and Dr. Albert Davydov, for their invaluable guidance and insightful advice. Their feedback significantly contributed to the development of my dissertation and the formulation of future research directions.

Being a student at the University of Virginia, especially in the electrical engineering department, has been an enriching journey. I am deeply grateful to my colleagues in the E-Snail lab whose collaborative atmosphere enhanced my understanding of electrical engineering, physics, and materials science. I extend my heartfelt appreciation to the former and current members of the ESNAIL group, including Dr. Naiming Liu, Dr. Golam Rosul, Dr. Emad Razaee, Farjana Ferdous Tonni, Shuai Li, and Sourav Das. Our academic and non-academic exchanges have been both enlightening and enjoyable.

My sincere thanks go to the National Science Foundation (NSF) and the Department of Energy (DOE) for their generous financial support.

In closing, I want to acknowledge the immense support and understanding from my family members – my parents, my wife, and my siblings. I am truly blessed to have them in my life.

Abstract

Thermal to electrical energy conversion using thermoelectric devices built based on the Seebeck effect has been intensely explored over the past two centuries. These devices not only convert heat into electricity but also operate in reverse, acting as solid-state refrigerators or coolers by actively pumping heat. Thermomagnetic devices are alternatives to thermoelectric devices and are built based on the Nernst effect. When temperature gradient and magnetic field are applied perpendicular to each other in a given material, a transverse voltage develops due to the Nernst effect in the direction normal to the plane containing the magnetic field and temperature gradient vectors. The Nernst coefficient is then defined as the ratio of the transverse electric field to the longitudinal temperature gradient, normalized to the applied magnetic field. The material parameters influencing the response of the Nernst effects are relatively unexplored compared to the well-known Seebeck effect.

This PhD thesis presents several significant findings. Firstly, an evaluation of the applicability of Moreau's relation in predicting the magnitude and trend of the Nernst coefficient in the standard thermoelectric material, Bi_2Te_3 , a narrow-band gap semiconductor, is undertaken. According to this relation, the Nernst coefficient of a material can be written as the negative of the product of its Thompson coefficient (defined as the product of the temperature of the sample and the first derivative of its Seebeck coefficient with respect to the temperature), Hall coefficient, and electrical conductivity. Moreau's relation is found to predict reasonably well the magnitude of Nernst coefficient and the temperature at which it changes sign. However, it could not explain the non-linear relationship between the Nernst coefficient and the applied magnetic field observed at low temperatures. As predicted by the relation, an increase in the Nernst coefficient magnitude is observed as the mobility of the carriers increases at lower temperatures.

Secondly, a larger Nernst coefficient is observed in the high-temperature phase of 1T-TiSe_2 where the mobility is the lowest. 1T-TiSe_2 is a layered semimetal representing a distinctive class of materials that exhibits slight overlap between their valence and the conduction band, accompanied by a high degree of carrier compensation. We attribute this increase to an abrupt reconstruction of the Fermi surface driving a rapid increase in the size of electron-hole pockets which leads to an increased bipolar effect and enhanced

Nernst coefficient.

Thirdly, an enhanced Nernst signal peak in MoTe₂ is observed. MoTe₂ is a topological Weyl semimetal that exhibits both quadratic and linear dispersion in its band structure. Analyzing the transport data, we attribute this to the movement of the Fermi level in crossing the Dirac point. A similar study was carried out on PdTe₂, a Dirac semimetal. Even after changing the temperature from 2 – 400 K and the magnetic field from –9 T to +9 T, such band crossing was not observed. This highlights the importance of $E_{\text{Dirac point}} - E_F$ as an important selection parameter in recognizing potential topological semimetals for thermomagnetic applications.

Fourthly, a sign change in the Nernst coefficient during the antiferromagnetic (AF) - ferromagnetic (FM) transition of FeRh/Al₂O₃, a metal, is recorded. The differing signs in the two phases were attributed to an anisotropic mobility of spin-up and spin-down electrons in the AF phase. Additionally, despite the AF phase displaying higher mobility, the magnitude of the Nernst coefficient was higher in the FM phase owing to the contribution from its internal magnetization. A hysteresis loop was evident in the temperature-dependent Nernst coefficient response with a shape similar to that observed in the Seebeck coefficient but with a narrower width.

Lastly, a significant Nernst coefficient of $11.2 \mu\text{VK}^{-1}\text{T}^{-1}$ at 80 K is observed in the F4TCNQ-doped P3HT polymer which is comparable to the response in many inorganic materials. The basis for this is not yet clear due to the polymers exhibiting much more complex molecular structures than the inorganic materials. As of now, this remains an open question and is a potential starting point for future work.

The practical implications of this PhD thesis lie in identifying efficient thermomagnetic materials that can be used in building environmentally friendly waste-heat to useful energy converters.

Contents

Declaration	ii
Approval	iii
Dedication	iv
Acknowledgments	v
Abstract	vi
1 Introduction	1
1.1 Thermoelectrics	1
1.1.1 Seebeck Effect	2
1.2 Thermomagnetics	3
1.2.1 Nernst effect	3
1.2.2 Thermomagnetic modules	6
1.2.3 Brief history of the Nernst effect	8
1.2.4 Theory of the Nernst effect	10
2 Nernst effect in the narrow band gap semiconductor Bi_2Te_3	14
2.1 Background and context	14
2.2 Transport property characterization	17
2.3 Results and discussion	19
2.4 Conclusion	26

3	Nernst response in the CDW and the normal phase of 1T-TiSe₂	28
3.1	Background and context	28
3.2	Results and discussion	29
3.3	Conclusion	35
4	Nernst effect in the type II Weyl semimetal Mo_{1-x}W_xTe₂	36
4.1	Background and context	36
4.2	Results and discussion	38
4.2.1	Seebeck coefficient as a phase transition probe	38
4.2.2	Nernst coefficient at low-temperature	41
4.2.3	Thermoelectric properties at different W content	43
4.3	Conclusion	46
5	Nernst effect in the Dirac semimetal PdTe₂	48
5.1	Introduction	48
5.2	Single-crystal growth by Bridgman method	50
5.3	Results and discussion	53
5.4	Conclusion	56
6	Nernst response during the magneto-structural phase transition in FeRh	57
6.1	Background and context	57
6.2	Materials and methods	60
6.2.1	Sample preparation	60
6.2.2	Transport property measurements	62
6.2.3	Computational Methods	62
6.3	Results and discussion	65
6.3.1	Magneto-thermoelectric properties of the FeRh/Al ₂ O ₃ thin film	65
6.3.2	Substrate dependence of the transport parameters	74
6.4	Conclusion	76
7	Nernst effect in the F4TCNQ-doped P3HT polymer	78
7.1	Background and context	78
7.2	Results and discussion	79

7.3 Conclusion	87
8 Outlook	89
Bibliography	90

List of Figures

1.1	Carriers with energy above or below the Fermi level oppositely (S_1 and S_2 , shaded areas) contribute to net Seebeck coefficient.	2
1.2	Schematic illustration of the a) Hall Effect, b) Seebeck Effect, c) Nernst Effect. Uniform temperature throughout the material (represented by solid color in the figure) is required for the Hall effect measurement while a temperature gradient (represented by the color gradient in the figure) is needed for the Seebeck and the Nernst measurements. Here V_H , V_S , V_N represents Hall voltage, Seebeck voltage, and Nernst voltage respectively, and $\nabla_i T$ represents the temperature gradient along the length of the sample.	4
1.3	Schematic illustration of the power generation (a, c) and the refrigeration (b, d) mode of a thermoelectric (a, b) and a thermomagnetic (c,d) module.	7
1.4	Temperature dependence of the a) thermoelectric and b) thermomagnetic figure of merit of various materials collected from literature.	9
2.1	a) Band structure of Bi_2Te_3 with (black) and without (green) SOC effect. The presence of SOC lowers the bandgap and Bi_2Te_3 turns to a narrow-gap semiconductor. b) the projected Density of States (DOS) including SOC shows that valence and conduction bands are mainly formed by Te and Bi p-orbitals, respectively. c) Brillouin zone for Bi_2Te_3 crystal structure	18
2.2	Contribution of p-orbitals of Bi (a) and Te (b). Similar to projected DOS, p-orbitals of Bi and Te form valence and conduction bands. The color bar is identical for all projection. The valence band of Bi_2Te_3 is mostly of type Te-p (right figure) and the conduction band is mostly of type Bi-p (left figure)	19

2.3	Variation of electrical and thermal properties of single-crystal Bi_2Te_3 with temperature: a) Seebeck coefficient, b) Resistivity, c) Thermal conductivity, and d) Hall coefficient R_H and Hall mobility μ_H	20
2.4	Plot of the temperature dependence of a) Magneto-Seebeck and b) Magnetoresistance. Here, S_{xx} and ρ_{xx} are the Seebeck coefficient and resistivity measured along the length of the sample under zero magnetic field and ΔS_{xx} and $\Delta\rho_{xx}$ are the respective change in these quantities once a magnetic field is applied	22
2.5	a) Mounted sample on the TTO puck. b) Temperature dependence of Nernst coefficient (N/H) obtained from experiment and Moreau's relation. c) Nernst coefficient (N/H) at different hole concentration calculated using Eq. 5 and 6 with inputs from first-principles calculations. d) Magnetic field dependence of the Nernst coefficient (N)	24
3.1	Temperature dependent variation in the a) electrical resistivity (ρ), b) $(1/\rho).(d\rho/dT)$, c) the Seebeck coefficient (S), and d) the thermal conductivity (κ) of single crystal $1T\text{-TiSe}_2$. The red-colored vertical dotted lines mark $T = 200$ K while the blue-colored vertical dotted lines mark the maxima or minima of the T-dependent curves.	32
3.2	Temperature-dependent variation in a) the Thomson coefficient (τ) and b) the Nernst coefficient (N). c) Magnetic field-dependent variation in the Thomson coefficient (τ) and the Nernst coefficient (N).	33
3.3	Temperature-dependent a) thermoelectric, b) Thomson, c) thermomagnetic figure of merit (zT).	34
4.1	Temperature dependence of the a) monoclinic angle β , b) resistivity, c) Seebeck coefficient, and d) Thomson coefficient of MoTe_2 over the cooling (solid line) and warming (dashed line) half-cycles. Inset in Fig. 4.1a shows the crystal structure of T_d and $1T'$ phases of MoTe_2 with their respective β angle indicated. Inset in Fig. 4.1c shows a sample mounted on the sample holder (puck) for measurement.	39

4.2	a) Temperature and b) magnetic field dependence of the Nernst Coefficient of MoTe ₂	41
4.3	Temperature dependence of the Nernst coefficient at varying W concentration	43
4.4	Temperature dependence of (a-c) resistivity, (d-f) Seebeck coefficient and (g-i) Thomson coefficient of Mo _{0.98} W _{0.02} Te ₂ , Mo _{0.97} W _{0.03} Te ₂ and Mo _{0.92} W _{0.08} Te ₂ over the cooling (solid line) and warming (dashed line) half-cycles	44
4.5	Temperature dependence of the $d\rho/dT$ of Mo _{0.98} W _{0.02} Te ₂ , Mo _{0.97} W _{0.03} Te ₂ and Mo _{0.92} W _{0.08} Te ₂ over the cooling (solid line) and warming (dashed line) half-cycles	46
5.1	Schematic of a Bridgman-Stockbarger setup.	50
5.2	Motion controller and temperature controller for the Bridgman-Stockbarger growth.	52
5.3	As-grown single crystal of PdTe ₂	52
5.4	X-ray diffraction of the as-grown single crystal PdTe ₂	52
5.5	Temperature dependent variation of resistivity at (a) B = 0 T, and (b) varying magnetic field in PdTe ₂	53
5.6	Magnetoresistance $[(\rho_B - \rho_0)/\rho_0] \times 100$ of PdTe ₂ at varying temperature and magnetic field	54
5.7	Seebeck coefficient (S) of PdTe ₂ at varying temperature and magnetic field	55
5.8	Nernst coefficient (S) of PdTe ₂ at varying temperature and magnetic field	55
6.1	X-ray fluorescence study of FeRh/Al ₂ O ₃ , FeRh/SiO ₂ and FeRh/MgO revealing Fe:Rh Mass% of 38:62, 37:63 and 37.5:62.5 respectively.	61
6.2	X-ray reflectivity data for FeRh/Al ₂ O ₃ , FeRh/SiO ₂ and FeRh/MgO with FeRh film thickness of 35, 20 and 80 nm respectively.	63
6.3	Chemically-ordered phase with B2 (CsC1)-type crystal structure [space group 221 ($Pm\bar{3}m$)] illustrating magnetic configuration and density of states of the FM (a-b) & AF (c-d) phase, respectively. Iron and Rhodium atoms are shown in red and silver respectively.	65

6.4	Density of States of FM phase of FeRh using PBE, SCAN, and DFT+U+J functionals.	66
6.5	Density of States of AF phase of FeRh using LDA, GGA (PBE, PBEsol), MetaGGA (TPSS, SCAN), and DFT+U+J functionals	67
6.6	Temperature-dependent variations in the resistivity (ρ), $\rho.d\rho/dT$, Seebeck coefficient (S), and Thomson coefficient ($\tau = T.dS/dT$) of FeRh/Al ₂ O ₃ . The magnetic field dependence of the thermal hysteresis is shown by different colors as indicated in the legend of (a). The black arrows indicate temperature sweep in the upward and downward direction respectively around the phase transition. Inset of (c) is a schematic representation of the Seebeck coefficient measurement setup	68
6.7	Derivative of ln(DOS) for two phases according to Mott formula.	69
6.8	The temperature and magnetic field dependence of the Nernst thermopower (N) and the Nernst coefficient (N/B) of FeRh/Al ₂ O ₃ . The legends in (b) and (d) align with those in (a) and (c), respectively. The black arrows indicate temperature sweeping up and down around the phase transition. The inset of (d) depicts the Nernst coefficient measurement setup.	70
6.9	Temperature-dependent magnetization of FeRh/Al ₂ O ₃ films in a magnetic field up to ± 3 T at 350 K. The measurement was taken using a PPMS system with a vibrating sample magnetometer (VSM) (Quantum Design, Inc. USA).	72
6.10	Variations in resistivity (ρ), Seebeck coefficient (S), and Thomson coefficient (τ) of FeRh/SiO ₂ (a-c) and FeRh/MgO with changing temperature. The legends in Figures 3b and 3c align with those in Figure 3a whereas the the legends in Figures 3e and 3f align with those in Figure 3d. The black arrows denote the temperature sweeping up and down around the phase transition.	73
6.11	Effects of tensile and compressive strain on the DOS of AF phase of FeRh. 4% tensile and compressive strain was applied along in-plane and out-of-plane simultaneously and vice-versa. The degree of strain along with the lattice parameter is also given.	76

7.1	Chemical structures of a) P3HT and b) F4TCNQ. c) schematic of the channel die; P3HT is inserted into the channel equipped with 2 spacers and flows along x-axis upon applying force along y-axis accompanied by heating to 100 °C d) WAXS images of P3HT bar along e) z-axis and x-axis f) before and g) after doping with F4TCNQ. h) integrated WAXS diffractogram of the images along x-axis	80
7.2	Electrical conductivity and Seebeck Coefficient of S1 and S2 obtained from measurements repeated over an extended period of time	81
7.3	Temperature dependence of a) electrical conductivity and b) Seebeck coefficient of Sample 1 (S1) and Sample 2 (S2) measured over an extended period. Fig. 2b follows the same legend as shown in Fig. 2a. Inset of Fig. 2b shows the schematic of the Seebeck Coefficient measurement connections.	82
7.4	FTIR absorption of a) F4TCNQ anion (blue) and neutral (pink), b) thin film of P3HT doped with F4TCNQ cooled down to 80 K from 300 K (solid lines from black to light blue) and re-heated up to 300 K (dotted black) . .	83
7.5	Temperature dependence of power factor of Sample S1 and Sample S2 measured over an extended period	85
7.6	Temperature dependence of the Nernst coefficient of Sample 1 (S1) compared with few inorganic and organic materials	86

Chapter 1

Introduction

1.1 Thermoelectrics

The Thermoelectric (TE) effect is the direct conversion of temperature difference to electricity. The thermoelectric performance of a material is evaluated by its dimensionless figure of merit, $z_{TE}T$, defined as $\sigma S^2T/\kappa$ where σ is the electrical conductivity, S is the Seebeck coefficient, κ is the thermal conductivity, and T is the average temperature of the material. TE modules can operate both in power generation and refrigeration mode making them an ideal candidate for a multitude of applications. These modules do not emit any greenhouse gas during their operation. Having no moving parts, they are silent in operation and require very low maintenance. The first observation of cooling using a Bi_2Te_3 thermocouple about seventy-five years ago inspired a surge of interest in the field of thermoelectric energy conversion [1]. Identifying suitable new materials and enhancing the thermoelectric properties of the already recognized ones have been the major research drive of the thermoelectric research community since then [2–14]. Significant progress was made in the 1950s. Heavily doped semiconductors were identified as good TE materials and commercialization of TE modules started using materials like Bi_2Te_3 and its alloys. Between 1960-1990 only incremental progress was made in the field. In the early 1990s, concepts like phonon-glass/electron-crystal (PGEC), and the incorporation of low-dimensional materials revived the field [15–17]. These concepts have grown parallelly and independently since then. In recent times, these ideas appear to be coming together with the inclusion of nanomaterials in bulk thermoelectric materials [18, 19].

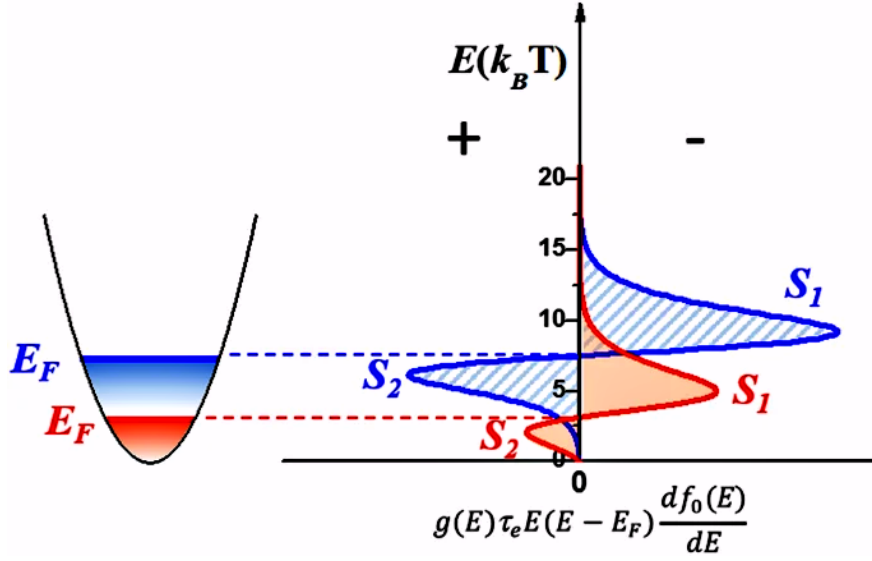


Figure 1.1: Carriers with energy above or below the Fermi level oppositely (S_1 and S_2 , shaded areas) contribute to net Seebeck coefficient.

1.1.1 Seebeck Effect

Thermoelectric power generation or refrigeration mode relies on the Seebeck effect in which a longitudinal electric voltage is generated in response to a temperature gradient Fig. 1.1 (reproduced from ref. [20]). According to the Boltzmann transport theory, the equation of the Seebeck coefficient, S , of a single-carrier (electron or hole) can be written as [21]:

$$S = \frac{1}{T} \frac{\int_0^{\infty} g(E) \tau_e E (E - E_F) \frac{df_0(E)}{dE} dE}{e \int_0^{\infty} g(E) \tau_e E \frac{df_0(E)}{dE} dE} \quad (1.1)$$

where, $g(E)$ is the density of states (DOS), τ_e is the relaxation time, E_F is the Fermi level, $f_0(E)$ is the Fermi-Dirac distribution function, e is the charge of the carriers and $\frac{df_0(E)}{dE}$ is the Fermi window. Only carriers within the vicinity of the the Fermi window contribute to the transport. Since, $e \int_0^{\infty} g(E) \tau_e E \frac{df_0(E)}{dE} dE$ is essentially the electrical conductivity of a material and always positive, the sign of S is always determined by the term $\left[g(E) \tau_e E (E - E_F) \frac{df_0(E)}{dE} \right]$ in the numerator. Carriers above and below the Fermi level give rise to S of opposite polarity.

$$S_1 = \int_{E_F}^{\infty} g(E) \tau_e E (E - E_F) \frac{df_0(E)}{dE} dE > 0 \quad (1.2)$$

$$S_2 = \int_{-\infty}^{E_F} g(E) \tau_e E (E - E_F) \frac{df_0(E)}{dE} dE < 0 \quad (1.3)$$

Total S of a material is the direct addition of these two contributions. For a material like metals where the Fermi level is deep inside the conduction band and nearly symmetric DOS above and below the Fermi level should result in a low S .

1.2 Thermomagnetism

1.2.1 Nernst effect

When a magnetic field is applied perpendicular to an imposed temperature gradient, there will be a secondary transverse voltage, the so-called Nernst voltage. The Nernst thermopower is then defined as the ratio of the transverse electric field to the longitudinal temperature gradient in the presence of a mutually orthogonal magnetic field. We refer to the Nernst coefficient as the slope of the Nernst thermopower with respect to the magnetic field (defined per magnetic field). Similar to the Seebeck voltage, the Nernst voltage can serve as the basis for thermal-to-electrical energy conversion. Just as the Seebeck effect is the thermal analog of the electrical resistivity, the Nernst effect is the thermal analog of the Hall effect. In the Hall effect, an electrical current is applied along the sample, and a magnetic field is present in the out-of-plane direction. In the Nernst effect, the electrical current is replaced by a thermal current. Hence the Nernst coefficient has features of both the Seebeck and Hall coefficients (see Fig. 1.2).

Let us assume the elements of the magneto-thermoelectric transport tensor as S_{ijk} , where i indicates the direction of the applied flux or temperature gradient, $-\nabla_i T$; j indicates the direction of the induced electric field, \vec{E}_j ; and k indicates the direction of the externally applied magnetic field, \vec{H}_k (if present). Because a magnetic field is not always present in characterizing thermoelectric transport, such as for the conventional Seebeck effect, the third index can be dropped in the absence of an externally applied magnetic field. With this labeling in mind, S_{xx} indicates a zero-field Seebeck coefficient, while S_{xyz} indicates a Nernst thermopower, both in units of $V.K^{-1}$. From this notation, it becomes apparent that the Nernst thermopower configurations are the off-diagonal components of the magneto-Seebeck tensor ($\vec{E}_j = [S(\vec{H})]\nabla T$). This notation also holds for the electrical resistivity and thermal conductivity transport tensors. To provide notation simplicity, alternatives like S in place of S_{xx} , N in place of S_{xyz} and N/B in place of

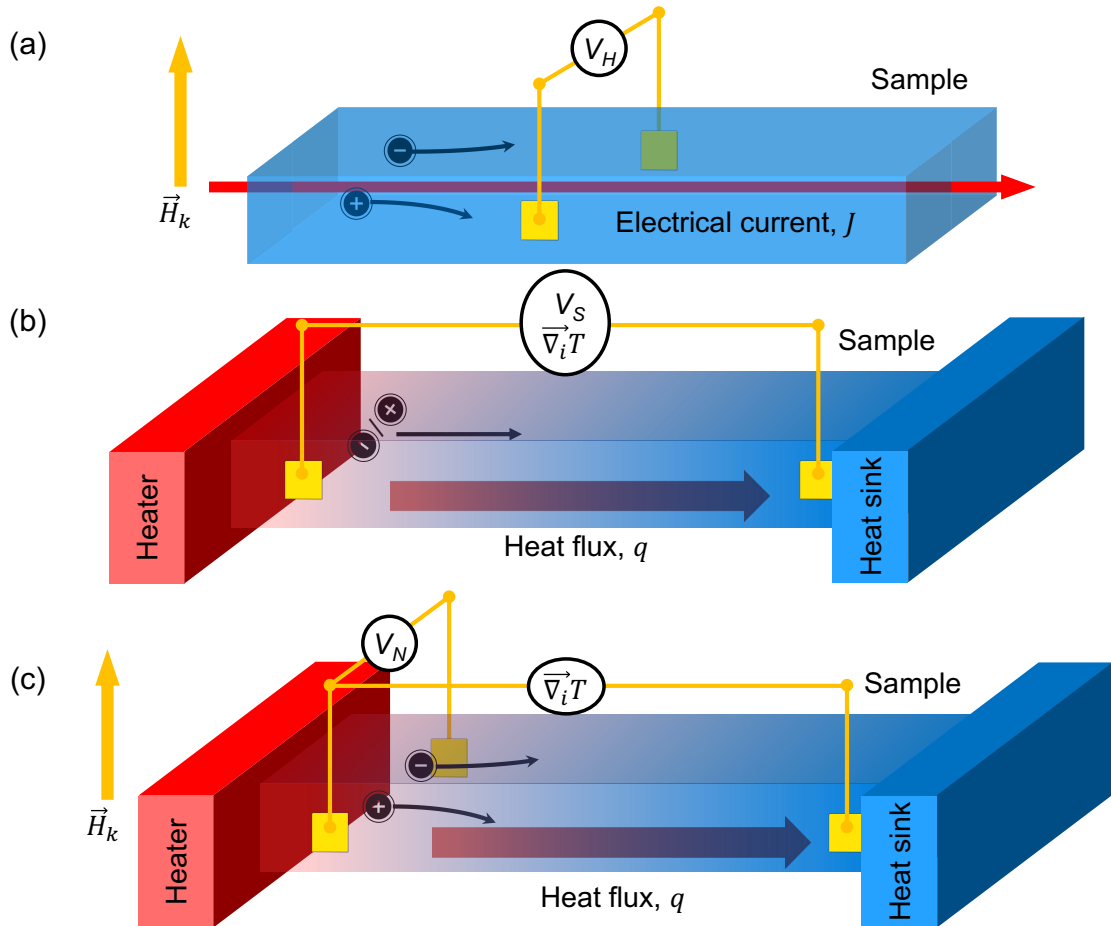


Figure 1.2: Schematic illustration of the a) Hall Effect, b) Seebeck Effect, c) Nernst Effect. Uniform temperature throughout the material (represented by solid color in the figure) is required for the Hall effect measurement while a temperature gradient (represented by the color gradient in the figure) is needed for the Seebeck and the Nernst measurements. Here V_H , V_S , V_N represents Hall voltage, Seebeck voltage, and Nernst voltage respectively, and $\nabla_i T$ represents the temperature gradient along the length of the sample.

Nernst coefficient will be used where needed in the dissertation.

A thermoelectric module can work in two distinct modes of operation: power generation and heat management. The latter includes refrigeration [22], active cooling [23], and thermal switching [24], all of which are based on the manipulation of heat with electricity using the Peltier effect. The Peltier effect is the thermodynamic inverse of the Seebeck effect wherein an electrical current passed through a heterojunction results in cooling or heating of the material within proximity of the junction. The Peltier coefficient is defined as the ratio of the electronic thermal current to the electrical current. Conceptually, we understand the cooling or heating to be the result of electrical current conservation at the junction which results in thermal current discontinuity when the Peltier coefficient varies across the junction. The Ettingshausen coefficient is the transverse analogue of the Peltier coefficient in the presence of a magnetic field and is the basis of thermomagnetic cooling. The Nernst and the Ettingshausen effects are therefore the basis of thermomagnetic power generation and heat management, respectively. In general, the Kelvin-Onsager relation relates the Peltier tensor (π_{ijk}) to the Seebeck tensor (S_{ijk}) as:

$$\pi_{ijk}(H_k) = TS_{ijk}(-H_k) \quad (1.4)$$

where i, j, k are directions as defined previously and T is the temperature. At zero magnetic field, we recover $\pi_{xx} = TS_{xx}$ relating the longitudinal Seebeck and Peltier coefficients. At nonzero magnetic fields, the off-diagonal elements of the Peltier tensor represent the Ettingshausen coefficients and the off-diagonal elements of the Seebeck tensor represent the Nernst thermopowers. These relations are valid in the linear transport regime when electrical and thermal currents are linearly proportional to the electric field and temperature gradient. Since the Peltier and Ettingshausen coefficients are related to Seebeck and Nernst thermopowers as described, they have the same dependence on the material's parameters such as electronic structure and scattering rates, and they follow the same physics. Hence, in the linear transport regime, it is sufficient to limit our discussion to the Seebeck and Nernst effects. The Nernst thermopower is also often referred to as the Nernst-Ettingshausen thermopower as a reminder of both the power generation and the cooling modes of thermomagnetic modules.

1.2.2 Thermomagnetic modules

The efficiency of a thermomagnetic power generator and the coefficient of performance of a thermomagnetic cooler are increasing functions of the material's thermomagnetic figure of merit defined as:

$$z_{TM}T = \left(S_{xyz}^2 \sigma_{yyz} T \right) / \kappa_{xxz} \quad (1.5)$$

where σ_{yyz} is the electrical conductivity along the y -direction (direction of the Nernst voltage), κ_{xxz} is the thermal conductivity along the direction of the applied thermal gradient, and T is the average temperature of the material. The form of the thermomagnetic figure of merit, $z_{TM}T$, replicates that of the thermoelectric figure of merit, zT , while accounting for the fundamental differences in geometry between the two. Traditional thermoelectric effects are longitudinal, with collinear heat and electrical flux, making it difficult to decouple thermal and electrical transport properties. For instance, the electrical conductivity of metal is proportional to its thermal conductivity; this builds the paradigm that a simultaneous electrical conductor and thermal glass is not possible in a strong metal where the electrons are both heat and electrical charge carriers. In contrast, in a thermomagnetic module, electrical and thermal conductivity are measured orthogonally to one another. Hence, it is possible to decouple the transport by designing an anisotropic conductor with large in-plane electrical conductivity and low cross-plane thermal conductivity. The 2D layered materials are a good example where the cross-plane thermal conductivity is weak due to the weak van der Waals interactions between the layers while the in-plane electrical conductivity can be strong in metallic and semimetallic layered structures.

A typical thermoelectric module requires alternating n-type and p-type legs connected electrically in series and thermally in parallel, as shown in Fig. 1.3, to return the electrical current to an isothermal plane. In contrast, thermomagnetic modules can be designed with a single type of material since the resultant electric field is inherently in an isothermal plane, resulting in a simplified module design involving fewer interconnections with significantly decreased contact resistance. Furthermore, traditional thermoelectric modules utilize single-carrier materials since the Seebeck effect is an even

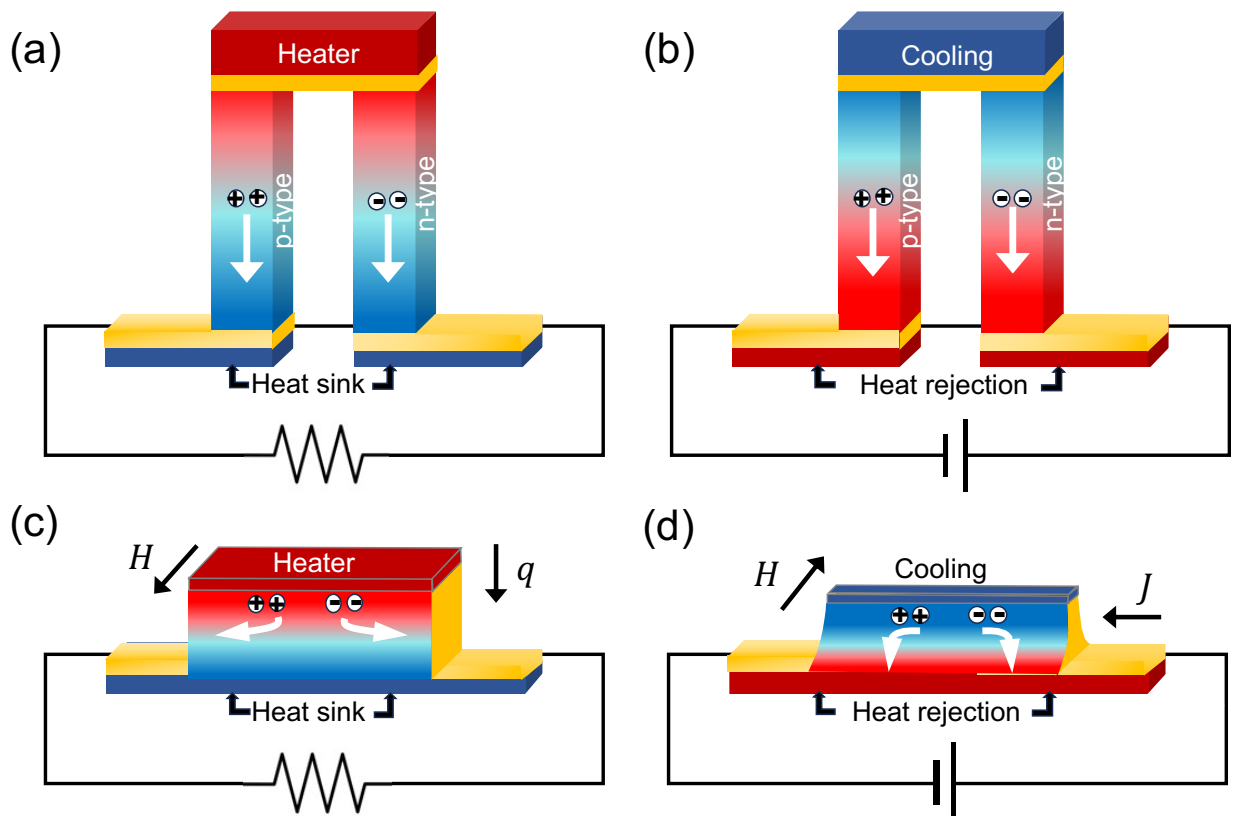


Figure 1.3: Schematic illustration of the power generation (a, c) and the refrigeration (b, d) mode of a thermoelectric (a, b) and a thermomagnetic (c,d) module.

function of charge carrier polarity, meaning both positively and negatively charged carriers move in the same direction, causing them to cancel out one another. Contrastingly, the Nernst effect is an odd function of charge carrier polarity since the magnetic field causes oppositely signed charge carriers to separate such that the contributions from both polarities of charge carriers effectively add. Thus, traditional thermoelectric materials are semiconductors, and traditional thermomagnetic materials are semimetals.

The typical structures of a single thermoelectric and a single thermomagnetic module operating in power generation and refrigeration modes are shown in Fig. 1.3(a)-(d). The performance of both modules varies depending on the size and shape of the legs used as they have a direct relationship with the module's electrical and thermal resistance. The geometry of a thermomagnetic leg has been optimized by various authors over the years. A trapezoid with arc sides, also referred to as the infinite-stage shape [see Fig. 1.3(d)] proposed by Harman, is considered the optimum shape for thermomagnetic modules used for heat management [25]. Harman used idealistic assumptions like temperature-

independent material properties and therefore temperature-independent current density in his derivation. More recently, Mobarak et al. [26] considered a temperature-dependent material parameter model and found a slightly modified version of the same shape (thinner in the middle) that has a higher coefficient of performance at larger temperature differentials.

The operating temperatures of thermoelectric modules are also different than those of thermomagnetic ones. The Seebeck coefficient and zT tend to increase with temperature. While there have been many reports of thermoelectric materials with $zT > 1$ at high temperatures, there are only a handful of materials with zT values near 1 at room temperature and none at temperatures below 200 K. Figure 3(a) summarizes some important traditional thermoelectric materials with high zT ($\text{AgPb}_{10}\text{SbTe}_{12}$ [27], $\text{AgPb}_{18}\text{SbTe}_{20}$ [27], B doped SiGe [28], $\text{Bi}_x\text{Sb}_{2-x}\text{Te}_3$ [29], $\text{Bi}_2\text{Te}_{2.79}\text{Se}_{0.21}$ [30], CsBi_4Te_6 [31], $\text{Mg}_2\text{Si}_{1-x}\text{Sn}_x$ [32], Na-Pb-Sb-Te [33] and PbTe-SrTe-Na [34]). In contrast, the Nernst thermopower tends to be maximized at low temperatures. Among the known thermomagnetic materials, many display their maximum $z_{TM}T$ at temperatures below room temperature. Only a handful of materials with $z_{TM}T$ have been reported, some of which are summarized in Fig. 3(b) (Bi_2Te_3 [35], $\text{Bi}_{97}\text{Sb}_3$ [36], $\text{Bi}_{99}\text{Sb}_1$ [36], Cd_3As_2 [37], $\text{PrFe}_4\text{P}_{12}$ [38], URu_2Si_2 [39], $\text{Li}_{0.9}\text{Mo}_6\text{O}_{17}$ [40], NbP [41], NbSb_2 [42], PtSn_4 [43], WTe_2 [44] and ZrTe_5 [45]).

1.2.3 Brief history of the Nernst effect

Initial studies of the Nernst effect and its measurement can be traced back to the late 19th century from the works of German physicists Albert von Ettingshausen and Walther Nernst, who first observed the development of a transverse voltage in a bismuth sample subjected to a heat current placed perpendicularly in a magnetic field [46]. Further extending their studies, they observed the same phenomena in metals such as copper, silver, and gold, and demonstrated that it can be a versatile probe in elucidating the electronic and thermal transport properties of metallic systems. Their works inspired many scientists to explore this effect in a wide range of materials including metals [47–50], semimetals [26, 51–53], and narrow gap semiconductors [54–57].

In the early 20th century, experimental measurements of the Nernst effect expanded to include rare metals such as molybdenum, tungsten, indium, cerium, tantalum, thal-

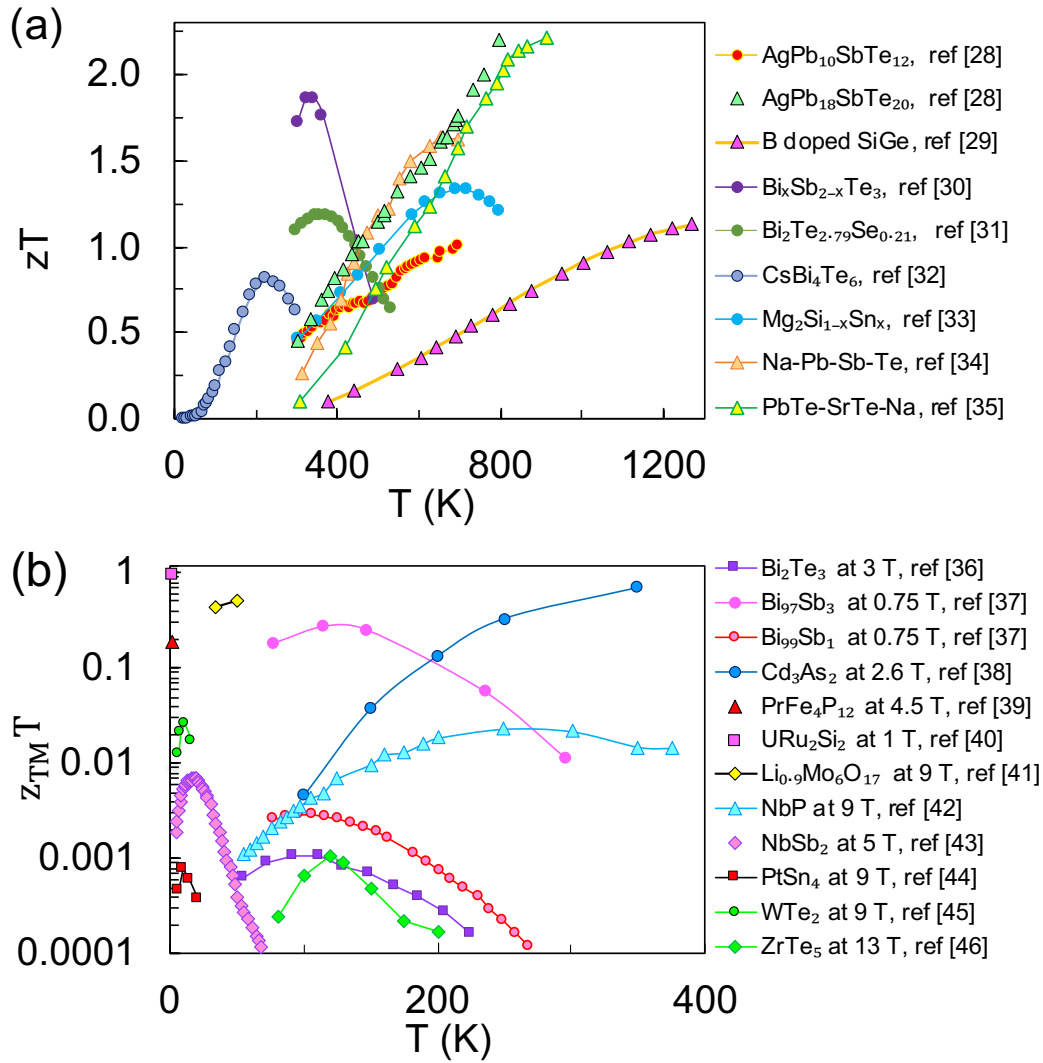


Figure 1.4: Temperature dependence of the a) thermoelectric and b) thermomagnetic figure of merit of various materials collected from literature.

lithium, and lithium [58], as well as nickel, cobalt [59], tellurium, soft iron [60], and alloys such as iron-cobalt [59], monel, nichrome [58], tellurium-antimony, tellurium-bismuth, tellurium-lead, antimony-silver, and copper-phosphorus [61]. Later in the 1950s, semimetals, a class of materials with co-existing electron and hole pockets (e.g., antimony, bismuth) became the focus of intensive study, as they exhibit characteristics that are intermediate between metals and non-metals, leading to unique magnetoresistance and thermomagnetic properties [52, 62]. At the same time, the exploration of the Nernst effect extended to semiconductors, such as germanium with a positive Nernst coefficient under 175 K and negative above this temperature [63], silicon with a Nernst

coefficient of around $-570 \mu\text{V.K}^{-1}$ at 50 K [64], lead selenide, lead telluride [65], bismuth telluride [66, 67], and antimony-cadmium [58].

In parallel with the exploration of new materials, there have been investigations of the potential use of the Nernst effect in making devices, such as power generators, refrigerators, and sensors. Harman introduced and explored the infinite-stage Nernst-Ettingshausen refrigerator, optimizing its geometry for optimal performance [25, 68, 69]. Other researchers extended Harman's theoretical optimization to geometries optimized for practical applications [26, 70], such as Guthrie et al. [70] who explored the geometry of this Nernst-Ettingshausen refrigerator at room temperature with single crystal bismuth. Wright explored the prospect of a Nernst-Ettingshausen generator made out of a semiconductor and defined a thermomagnetic figure of merit [71]. Concurrently, the theoretical aspects of anisotropic Nernst-Ettingshausen devices and their operational characteristics were explored [72]. In recent decades, the field of experimental Nernst measurements has witnessed significant advancements. Researchers have explored exotic materials such as topological insulators and low-dimensional systems, thereby further expanding the understanding of the Nernst effect [73–75]. Behnia has provided a comprehensive review of the effect in metals, superconductors, and semiconductors [76, 77]. Additionally, novel measurement techniques and equipment have allowed for more precise and comprehensive characterization of the Nernst effect [78–80].

1.2.4 Theory of the Nernst effect

The Nernst theory has been developed over more than a century. In 1900, Moreau [81] developed a phenomenological model for the Nernst coefficient which was shown valid in many metals [82]. According to this relation, the Nernst thermopower of a material can be defined as the negative of the product of its Thomson coefficient (defined as the product of the temperature of the sample and the first derivative of its Seebeck coefficient with respect to the temperature, $(\tau_{xxz} = T \frac{dS_{xxz}}{dT})$, Hall coefficient R_H , and electrical conductivity σ_{xxz} :

$$S_{xyz} = -\tau_{xxz}\sigma_{xx}R_H \quad (1.6)$$

Sondheimer studied the galvanometric and thermomagnetic effects in metals with s and d bands [83]. Sommerfeld and Frank [84] obtained an electronic distribution func-

tion in the presence of a magnetic field by solving the Boltzmann transport equation and linear response theory to derive an equation for the Nernst coefficient in metals. Putley extended the Sommerfeld-Frank formalism to semiconductors and mixed conductors [65, 85]. Theoretical predictions of the Nernst thermopowers of PbTe and PbSe appeared to be reasonably close to experimental values. Price [67] developed a model for the Nernst thermopower in the case of isotropic two-band semiconductors using Boltzmann statistics. He found that the Nernst thermopower can be expressed as a function of electrical conductivity, Hall and drift mobilities, the Seebeck coefficient of each band, and the diffusion coefficient. Delves studied the symmetry of thermomagnetic properties of semiconductors and semimetals within the relaxation time approximation (RTA) and multi-valley band structure [52]. Nakamura et al. studied the thermomagnetic effect in semiconductors using a Maxwell-Boltzmann-like distribution function for both parabolic [86] and non-parabolic [87] dispersions and compared the theory with experiments. Clayhold studied the Nernst effect in anisotropic materials and found that the value of the Nernst thermopower depends on the correlation between the Hall angle and thermopower at different points on the Fermi surface [49]. Pikulin et al. [88] compared the value of the Nernst thermopower in cuprate superconductors calculated using constant relaxation time approximation (CRTA) and momentum-dependent relaxation time approximation. They found that in the combined presence of band and scattering anisotropy, the CRTA is a poor approximation and can result in an error significant enough to result in a Nernst coefficient of the wrong sign. Using semiclassical approaches, Behnia [76] proposed two routes toward large Nernst thermopower in metals: the presence of multiple bands and energy-dependent Hall angle or energy-dependent mobility.

More recently, Zebarjadi et al. [89] have developed a simple description of the Nernst theory using an RTA and power laws to describe the energy dependence of the scattering rates. They have shown that within an isotropic single-band model, the Nernst thermopower is zero under the CRTA. A nonzero Nernst thermopower in this case is the result of energy-dependent relaxation times and is proportional to the difference between thermal and Hall mobilities multiplied by the Seebeck coefficient. Within the anisotropic bands, the Nernst thermopower is nonzero even within the CRTA, and it

is proportional to the difference in the Seebeck coefficient of x and y directions. They conclude that identical electron and hole bands that are anisotropic (in the crystallographic directions perpendicular to the magnetic field) with large s -parameters and zero or overlapping bands are the best candidates for good thermomagnetic materials [89].

The models described here are only valid for weak magnetic field regimes. The Boltzmann equation breaks down at large magnetic fields when cyclotron frequency ω_c multiplied by the relaxation times (τ) is much larger than unity ($\omega_c\tau \geq 1$) where the response is nonlinear. In addition, when $\hbar\omega_c > k_B T$, then the splitting of the Landau levels is greater than the thermal energy, and the wave number is not a good quantum number. The Fermi surface breaks into one-dimensional Landau levels and leads to quantum oscillations of transport properties with respect to the magnetic field. Periodic oscillations with respect to $1/H$ (Schubnikov-de Haas effect) are observed in many magnetoresistance measurements. These oscillations are also observed in Seebeck and Nernst measurements of some samples [90, 91]. Several theoretical works have explored and explained these oscillations. Landau levels and their dependence on electric fields and their effect on Nernst oscillations are discussed in graphene [92] and bismuth [93], for example, theoretically.

Accurate calculations of the Nernst thermopower without fitting parameters are a challenge that has not yet been fully addressed. The Seebeck coefficient calculations based on first principles have advanced significantly in the past decade. First-principles-based codes such as BoltzWann [94] and BoltzTrapz [95] have been developed and significantly contributed to the prediction power of the thermoelectric community. The Seebeck coefficient is not sensitive to the details of scattering parameters. Hence, even within the CRTA approximation, accurate Seebeck coefficient values can be predicted merely based on the full electronic band structure. The Nernst coefficient however is very sensitive to the details of scattering rates as the Nernst coefficient is proportional to the carrier mobility. It is also a tensor response and the direction of the magnetic field relative to the crystal directions plays an important role. Therefore, accurate numerical calculations of the Nernst coefficient are a challenge. This challenge has been addressed recently by Rezaei et al. [96, 97]. They have developed a module to be added to the BoltzWann code in which the effect of the magnetic field on transport properties is in-

cluded within CRTA [96]. They have then shown that if scattering rates can be added properly, for instance using the AMSET code [98], to reproduce the mobility correctly, the same rates can be used to predict and reproduce the experimental Nernst values in semiconductors [97]. We note that to extend this to semimetals and metals, the correct inclusion of scattering rates in these materials is required; to extend this to magnetic materials and materials with a nonzero Berry curvature, the inclusion of the anomalous Nernst effect is required.

Chapter 2

Nernst effect in the narrow band gap semiconductor Bi_2Te_3

Collaborators and Personal Contributions: Single-crystals used in this study were grown by Dr. Sergiy Krylyuk from Dr. Albert Davydov's group at the National Institute of Standards and Technology. First-principal calculation was done by S. Emad Rezaei under the supervision of Dr. Keivan Esfarjani of MSE, UVA. The Nernst theory here was done by Dr. Mona Zebarjadi. The electrical, thermoelectric, and thermomagnetic characterizations were all done by Md Sabbir Akhanda under the supervision of Dr. Mona Zebarjadi.

2.1 Background and context

Despite the discovery of numerous other thermoelectric materials to this date, Bi_2Te_3 and its alloys (with Sb_2Te_3 for p-type and with Bi_2Se_3 for n-type conductivity, respectively) are still the dominant materials used in commercial thermoelectric modules for near room-temperature applications [99]. Hence, it is no surprise that a large number of articles are focused on the study of Bi_2Te_3 thermoelectric transport properties [100–104]. Bismuth Sesquitelluride Bi_2Te_3 is a layered material and inherently has low thermal conductivity [105]. At the same time, it is a topological material with a complex band structure [106]. Many detailed first-principles studies have been reported so far to better understand the electronic band structure and consequently thermoelectric properties of the Bi_2Te_3 family [106–114]. Due to spin-orbit interaction, Bi_2Te_3 has band inversion with

band extrema that are not at the high symmetry Γ point [106]. The resulted valleys have small effective masses and high valley degeneracy, making the electronic band structure of Bismuth Sesquitelluride Bi_2Te_3 ideal for thermoelectric applications. Various reports on the Seebeck coefficient and the Hall measurement of doped samples pointed to the necessity of a six-valley band model to properly describe the relationship between the Hall coefficient and the carrier concentration [115–118]. While examining the thermal conductivity behavior at a temperature range of 77 K to 380 K, Satterthwaite and Ure reported a sharp rise in the thermal conductivity around room temperature and above due to ambipolar diffusion of electrons and holes [105]. Goldsmid found that the lattice thermal conductivity of doped Bi_2Te_3 is independent of its electrical conductivity [119]. He reported that doping with halogen atoms is an exception and results in the reduction of lattice thermal conductivity due to the large cross-section of phonon-halogen atom scattering.

While the thermoelectric properties of Bi_2Te_3 have been well-studied to attain a higher figure of merit, the thermomagnetic properties lack the same research depth. When a magnetic field is applied in the z -direction, i.e., normal to the basal (0001) crystal plane in Bi_2Te_3 , the thermomagnetic figure of merit, $z_{TM}T$ is defined as $(N^2\sigma_{yy}T)/\kappa_{xx}$ where N is the Nernst coefficient in the unit of $\mu\text{V}/\text{K}$, σ_{yy} is the electrical conductivity in the y -direction, κ_{xx} is the thermal conductivity along the direction of the applied thermal gradient, and T is the average temperature of the material [120]. The Nernst coefficient in the thermomagnetic transport is the transverse equivalent of the Seebeck coefficient S_{xx} in the thermoelectric transport. Thermomagnetic power generators and coolers are an alternative to thermoelectric modules. They have several advantages compared to their thermoelectric counterparts such as exhibiting higher energy conversion efficiency for the same zT (adiabatic) (applicable when the zT (adiabatic) is greater than 0.2) [121, 122], better suitability for energy conversion in the case of thin films, and simpler design as the module can be made using only one material compared to two (n-type and p-type) in case of a thermoelectric module [52, 122]. The potential that the transverse thermomagnetic properties hold in energy conversion can duly be stressed by taking the Dirac semimetal Cd_3As_2 as an example. In a recently published paper, it has been reported that, primarily due to its large Nernst coefficient, Cd_3As_2 has a trans-

verse thermomagnetic $z_{TM}T \approx 0.5$ at room temperature which is more than twice its longitudinal thermoelectric $z_{TE}T$ [37]. The study of the Nernst effect is also important in spintronics. It has recently been shown that the Nernst voltage can be a source of spurious signal in spin-orbit torque measurements in topological insulators [123]. The magnetization dynamics can be controlled by thermally driven spin Nernst torque [124]. Therefore, taking a closer look at the thermomagnetic properties of Bi_2Te_3 is evidently fitting. To our best knowledge, only a few attempts have been made to study the Nernst effect in Bi_2Te_3 so far. Mansfield and Williams in 1958 measured the Nernst coefficient of Bi_2Te_3 under a magnetic field of 1.4 T and reported a slow increase in the coefficient with decreasing temperature [56]. In 1966, Champness and Kipling measured the Nernst coefficient for an n-type Bi_2Te_3 under a constant magnetic field of 1.88 T applied parallel to the cleavage plane and concluded that the electron to hole mobility ratio of their sample decreases up to room temperature [125]. In 1997, Zhitinskaya *et al.* used the Nernst measurement at 300 K in the weak magnetic field regime as a means to predict the degree of inhomogeneity present in the Bi_2Te_3 crystal [55]. All these studies revealed useful information but do not provide a complete picture of the Nernst effect covering both wide magnetic fields and a large temperature range.

In this work, we report the measurement of the Nernst coefficient of Bi_2Te_3 over a wide range of magnetic fields and temperatures. We have observed a change in the sign of the Nernst coefficient (N) as predicted by the Moreau's relation[126] [Eq.(2.1)] around the same temperature at which the Seebeck coefficient peaks.

$$N = TR_H \sigma \frac{\partial S}{\partial T} \quad (2.1)$$

We have also observed a non-linear behavior of the Nernst coefficient versus H in the high magnetic field regime ($\mu H > 1$). The measurement of thermoelectric properties, Hall coefficient, magneto-Seebeck, and magnetoresistance have been included in this report to provide a more complete perspective. We used First-principles calculations and analytical solutions of the Boltzmann transport equation (BTE) using the constant relaxation time approximation and in the presence of an externally applied magnetic field to calculate magneto-transport responses. In the absence of the magnetic field, theoretical Seebeck coefficients accurately reproduce the experimental ones. The presence of the magnetic field introduces the magneto-Seebeck, the magnetoresistance, and the Nernst

signal. Finally, the Nernst signal was calculated using phenomenological models. The trends seen in the theoretical result agrees with that of the experiment, but these are not in quantitative agreement primarily due to the use of constant relaxation time approximation (CRTA) during the theoretical calculations.

2.2 Transport property characterization

A $8.7 \times 3.9 \times 1.5 \text{ mm}^3$ ($L \times W \times H$) sized sample was cut from the central part of the ingot. Gold-plated flat copper wire of 0.5 mm width was used to make contact electrodes. A two-component silver-filled epoxy was used to glue the contact wires to the sample. The thermoelectric properties of the sample, at a temperature range 55 K to 380 K and magnetic field of -3 T to 3 T , were measured by the one-heater and two-thermometer configuration using the thermal transport option (TTO) of the VersaLab (Quantum design Inc.). The applied magnetic field was perpendicular to the direction of the thermal gradient and the cleavage plane. To establish a thermal gradient along the length of the sample, a resistive heater was attached to one end of the sample. Another contact attached at the opposite end of the sample was clamped to the cold foot of the TTO puck which acted as a heatsink. Thus, the temperature difference is applied between two parallel heat sink and heat source placed 8.7 mm apart, implying that the slow transverse voltage measurements are done under nearly isothermal conditions, and the reported Nernst coefficients are the isothermal values rather than the smaller adiabatic values. Two TTO shoes placed 3.4 mm apart were employed to measure the temperature and the voltage difference simultaneously. For the Seebeck measurement over the entire range of temperature, an adaptive measurement mode was used that maintained the temperature difference within (1 to 3)% of the sample temperature. Taking into account the geometrical factor of the sample and Versalab system specification, the estimated errors in the Seebeck, thermal conductivity, and resistivity measurement were about 5%, 10%, and 3% respectively. Nernst measurement was also carried out using the one-heater two-thermometer configuration in the temperature range of 55 K to 300 K. Magnetic field with a step increase of 1 T was applied up to 3 T in both z and $-z$ directions. Transverse voltage was measured by two voltage probes attached to two

gold-coated copper contacts placed perpendicular to the thermal gradient and the magnetic field directions. The estimated error in the Nernst measurement was $\approx 10\%$ (the main error sources include fitting errors of Versalab software, error in measurement of the sample size, non-uniformity of the temperature gradient, and instrumental errors). To determine the carrier concentration, a four-probe Hall measurement was carried out using the electrical transport option (ETO) of VersaLab (Quantum design Inc.) in the temperature range of 50 K to 380 K. In this measurement, two voltage leads were placed transversely to the direction in which the current and the magnetic field were applied. The estimated error in the measurement was $\approx 5\%$. The thermal gradient and magnetic field applied in all measurements described above were parallel and perpendicular to the material's cleavage plane, respectively.

The same techniques have been employed to analyze samples discussed in the subsequent chapters. To prevent repetition, I will refrain from reiterating these specifics there.

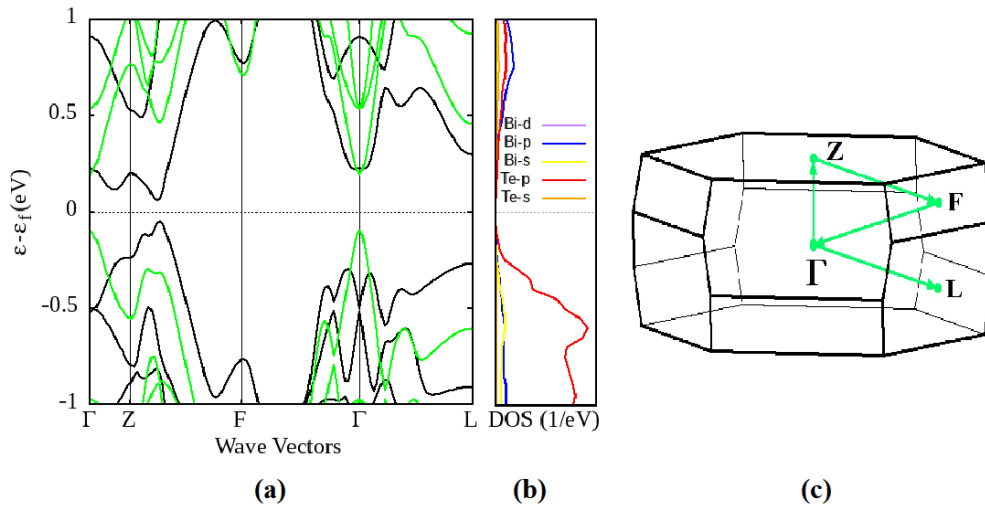


Figure 2.1: a) Band structure of Bi_2Te_3 with (black) and without (green) SOC effect. The presence of SOC lowers the bandgap and Bi_2Te_3 turns to a narrow-gap semiconductor. b) the projected Density of States (DOS) including SOC shows that valence and conduction bands are mainly formed by Te and Bi p-orbitals, respectively. c) Brillouin zone for Bi_2Te_3 crystal structure

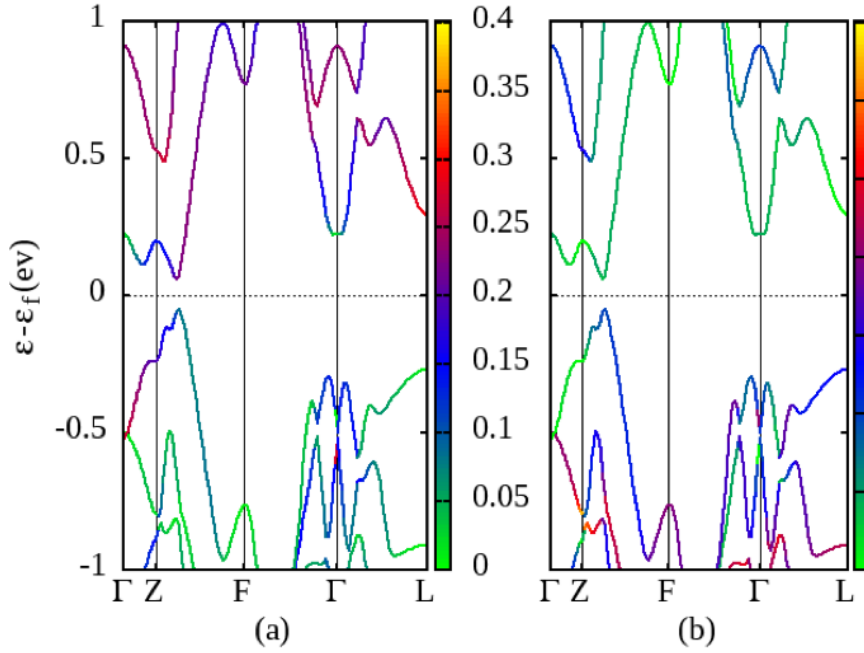


Figure 2.2: Contribution of p-orbitals of Bi (a) and Te (b). Similar to projected DOS, p-orbitals of Bi and Te form valence and conduction bands. The color bar is identical for all projection. The valence band of Bi_2Te_3 is mostly of type Te-p (right figure) and the conduction band is mostly of type Bi-p (left figure)

2.3 Results and discussion

The Spin-orbit coupling (SOC) effect plays an important role in the electronic structure calculations [127]. Fig. 2.1 (a) compares the band structure of Bi_2Te_3 with and without SOC. The inclusion of SOC results in a significant reduction in the bandgap from 0.29 eV to 0.11 eV and a significant change in the effective mass values. For example, at the Γ point, the conduction band effective mass increases from $0.15m_0$ to $0.7m_0$ after introducing SOC effects. Finally, band inversion happens at Γ point in the presence of the SOC effect. Our results are in agreement with previous calculations [128] and the obtained bandgap of 0.11 eV is close to the experimentally measured bandgap of 0.15 eV [129].

The contribution of each atomic orbital to the total density of states is shown in the Fig. 2.1b. The valence band is dominated by p-orbitals of tellurium and the conduction band is mostly composed of p-orbitals of bismuth, which is in agreement with the pro-

jected band structure (Fig. 2.2). The color bar in Fig. 2.2 indicates the contribution of a specific orbital in each band from the lowest (green) to the highest (yellow) contribution (e.g. in Fig. 2.2a valence band is more blue-red which shows a high contribution of p-orbitals of Bi). In this figure, band inversion of the Bi-p orbitals can be seen: the valence band acquires a Bi-p component near the Γ point.

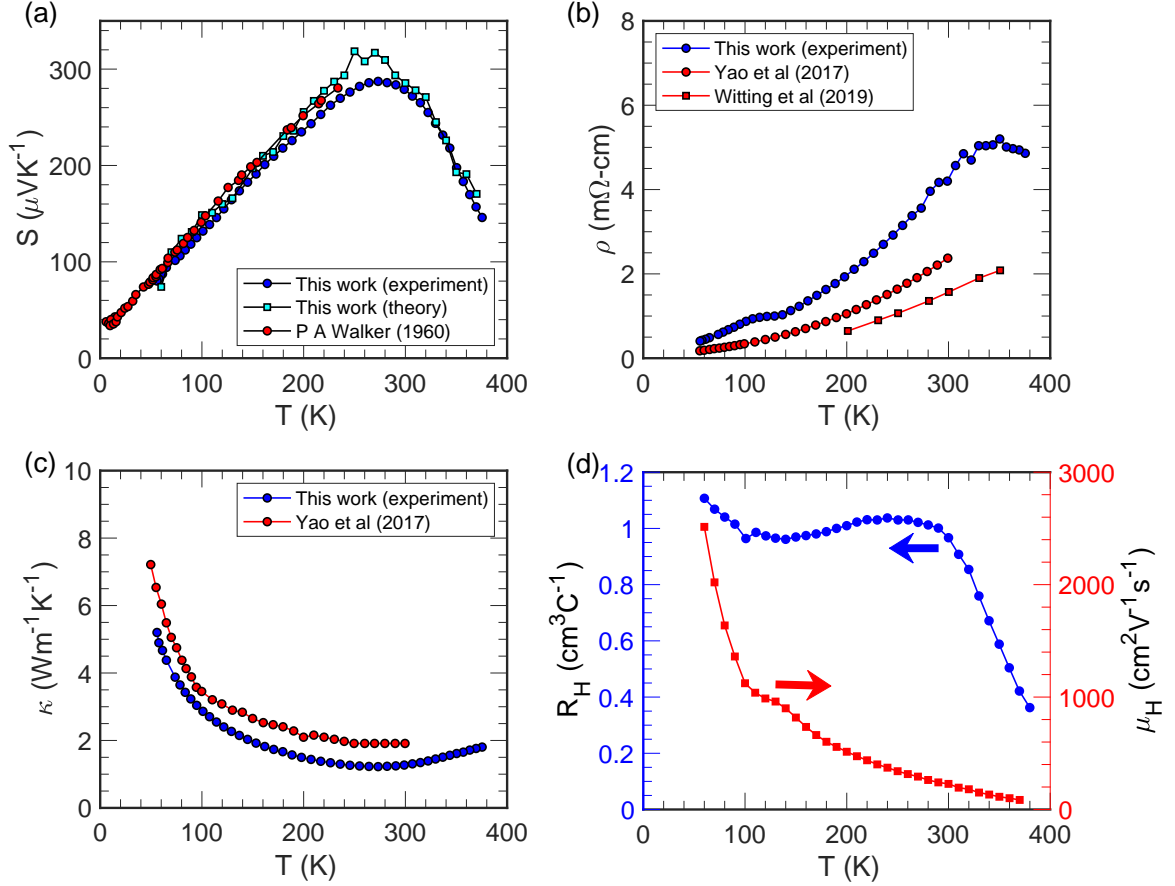


Figure 2.3: Variation of electrical and thermal properties of single-crystal Bi_2Te_3 with temperature: a) Seebeck coefficient, b) Resistivity, c) Thermal conductivity, and d) Hall coefficient R_H and Hall mobility μ_H .

Temperature dependence of the transport coefficients including the Seebeck coefficient, S , the electrical and thermal conductivity, the Hall coefficient, and the carrier mobility is shown in Fig. 2.3. Our measured sample has mobility of $227 \text{ cm}^2\text{V}^{-1}\text{s}^{-1}$ at 300 K which is very close to the ones reported by other sources on similar samples [105, 117, 130]. Carrier concentrations were computed from experimental Hall coeffi-

cient values, for which the corresponding chemical potentials were estimated through the first-principles calculations followed by Seebeck coefficient computation of each chemical potential. Experimentally measured Seebeck values were reproduced by first-principles calculations (explained in the computational detail sub-section). It is noteworthy to say that small deviations between theory and experiments could come from constant relaxation time approximation assumption.

The Seebeck coefficient trend over the entire temperature range can be divided into two distinct regions as also noted by many previous reports on Bi_2Te_3 [101, 115, 131]. The separation roughly lies around 273 K where the Seebeck coefficient reaches its peak value of $+287 \mu\text{V}/\text{K}$. Below 273 K, the carrier concentration does not change significantly as evidenced by a weak change of the Hall coefficient (Fig. 2.3d). In this range, as temperature increases, the carrier mobility decreases due to the increase in the electron-phonon scattering rates. Hence, we observe a metallic behavior where resistivity increases with temperature. In this regime, since the free carrier density is almost fixed, as we increase the temperature, the quasi-Fermi level moves closer to the middle of the gap increasing the Seebeck coefficient. Beyond 273 K, intrinsic carriers excited across the bandgap dominate conductivity. In this region, we see a decrease in the Seebeck coefficient with increasing temperature as both electrons and holes are generated (the bipolar effect). The resistivity starts to decrease due to the increase in carrier concentration. The sign of the Seebeck coefficient remains positive throughout the entire temperature range which is a confirmation that the sample is nominally p-type doped. Bi_2Te_3 is known as a topological insulator [106]. However, Bi_2Te_3 single crystal is naturally p-type and its bulk energy bands are characterized by a small bandgap and are strongly influenced by spin-orbit interactions. Hence, it is difficult to observe an electrically insulating bulk [132]. In particular, in the temperature range of our study, the sample behaves as a metal rather than an insulator. We also note that even though our calculations only included the bulk states, they can describe the Seebeck coefficient in agreement with the experiment (as shown in Fig. 2.3a). We expect the surface states are dominant at much lower temperatures [133] and much lower thicknesses [134]. In semiconductors, total thermal conductivity has contributions from phonons, electrons, and bipolar transport [135]. In the temperature range of 55 K to 200 K, thermal transport is dominated by phonon

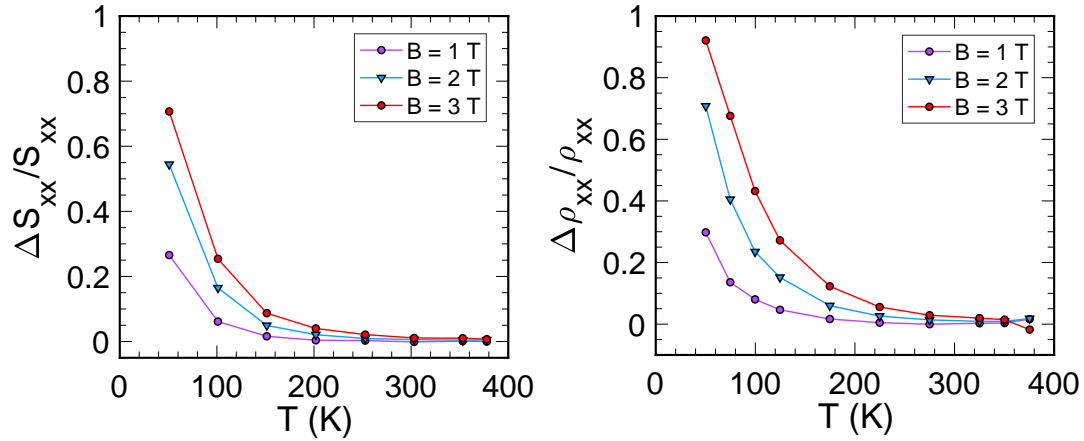


Figure 2.4: Plot of the temperature dependence of a) Magneto-Seebeck and b) Magnetoresistance. Here, S_{xx} and ρ_{xx} are the Seebeck coefficient and resistivity measured along the length of the sample under zero magnetic field and ΔS_{xx} and $\Delta\rho_{xx}$ are the respective change in these quantities once a magnetic field is applied

thermal conductivity. As we increase the temperature, we see a decreasing trend in the thermal conductivity due to the increase in anharmonic phonon scattering as shown in Fig. 2.3c. At higher temperatures (above 300 K), the bipolar contribution becomes significant and results in a rise in the total thermal conductivity. Fig. 2.3d shows the measured Hall coefficient and the extracted carrier Hall mobility. We need to point out that at temperatures above 273 K, where bipolar conduction starts, the extracted Hall mobility is very different from the drift mobility and we cannot separately extract the drift mobility of electrons and holes. The Hall coefficient is proportional to the inverse of the difference between the number of holes and electrons, while the electrical conductivity is the sum of the electron conductivity and hole conductivity. The Hall mobility is extracted by dividing the electrical conductivity by the Hall carrier concentration.

Fig. 2.4 shows the temperature dependence of the magneto-Seebeck and the magnetoresistance of the sample in the magnetic field range of 1 T to 3 T applied perpendicular to both the thermal gradient and the cleavage plane. Each data points were obtained by applying the magnetic field both in positive and negative directions and then averaging the corresponding ΔS_{xx} and $\Delta\rho_{xx}$ responses. The change in the Seebeck coefficient and the resistivity are always positive below 375 K. These results are consistent with the previously reported data [125]. The decrease in the value of the magneto-Seebeck

and magnetoresistance versus temperature can be attributed to the reduced mobility at higher temperatures.

Fig. 2.5a shows the sample mounted on a TTO puck for the Nernst measurement. Temperature dependence of the Nernst coefficient is shown in Fig. 2.5b. Here also, for each data points, the magnetic field was applied both in positive and negative directions and the responses were averaged. The Nernst signal, similar to the magneto-Seebeck and magnetoresistance, increases as we decrease the temperature. In the same graph, we have also plotted the Nernst coefficient of this material calculated using the Moreau's relation [81]. According to this relation, the Nernst coefficient of a material can be written as the negative of the product of its Thompson coefficient (defined as the product of the temperature of the sample and the first derivative of its Seebeck coefficient with respect to the temperature) [136], Hall coefficient, and electrical conductivity. Moreau's relation predicts a change in the sign and a zero Nernst signal at the same temperature at which the Seebeck coefficient peaks (≈ 273 K for this sample). Our experimental data show that the Nernst signal changed its sign at about 255 K which is in close agreement with Moreau's prediction. The difference stems from the inaccuracy of the Moreau's relation as well as error bar in the measurements of the involved transport coefficients (the Seebeck coefficient, Hall coefficient, the electrical conductivity, and the Nernst coefficient). We note that Moreau's relation is only accurate for metals. However, as shown, it can still closely replicate the results of Bi_2Te_3 , a narrow-gap semiconductor. Above 255 K, the Nernst coefficient is positive and maintains a linear relationship with the applied magnetic field. But below 255 K, the linearity ceases quickly and non-linear behavior of the Nernst coefficient versus the magnetic field slowly emerges (Fig. 2.5d). This non-linear behavior intensifies as we go down in temperature. Moreau's relation cannot account for this non-linearity. The basis of this behavior becomes apparent when the Boltzmann Transport Equation under a magnetic field is solved. The following formalism is developed after Behnia [137] and following Smith's [138] notation. Electrical current density under an external magnetic field (H) can be written as:

$$\begin{bmatrix} J_x \\ J_y \end{bmatrix} = \begin{bmatrix} \sigma(H)_{xx} & \sigma(H)_{xy} \\ \sigma(H)_{yx} & \sigma(H)_{yy} \end{bmatrix} \begin{bmatrix} E_x \\ E_y \end{bmatrix}$$

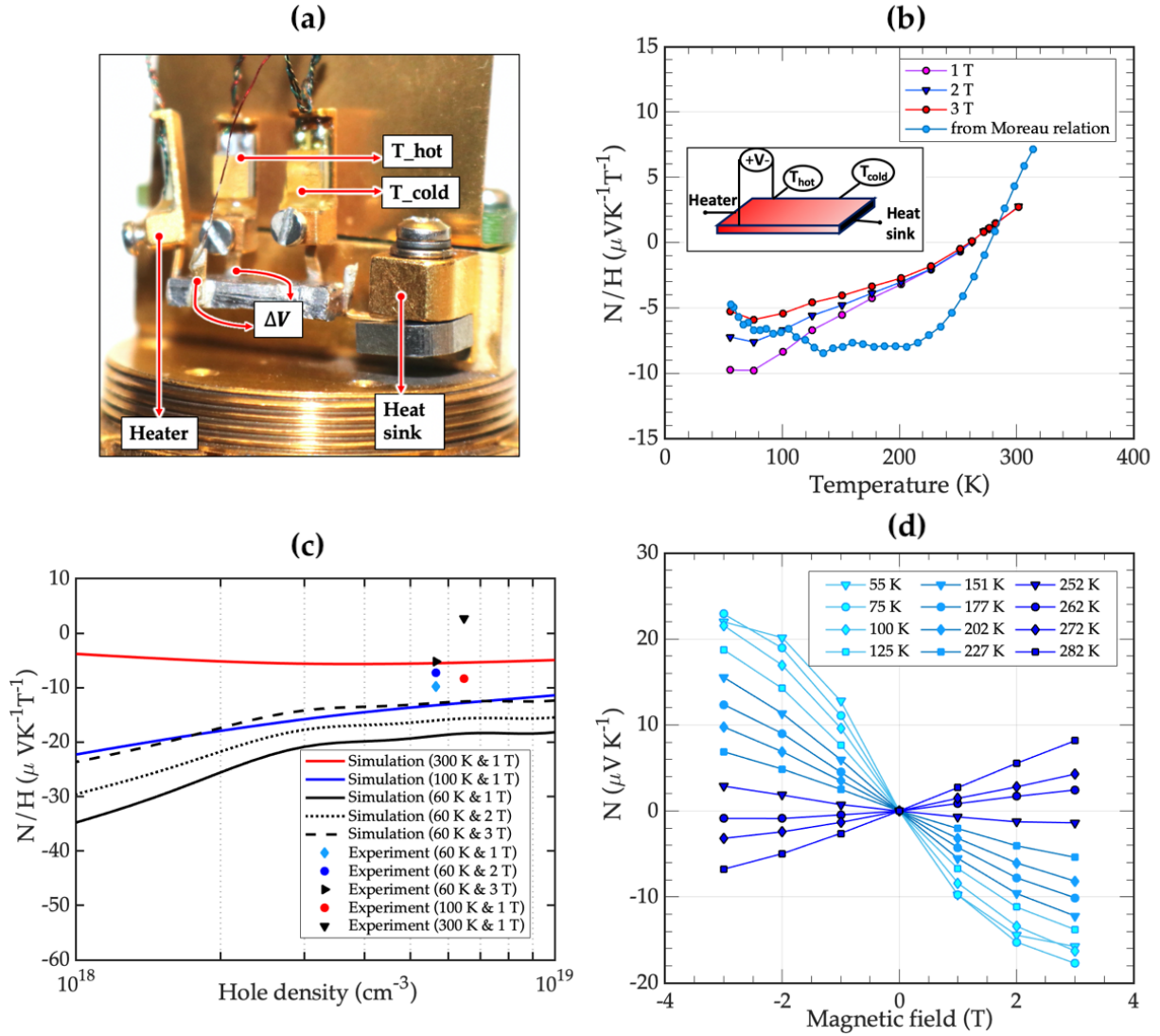


Figure 2.5: a) Mounted sample on the TTO puck. b) Temperature dependence of Nernst coefficient (N/H) obtained from experiment and Moreau's relation. c) Nernst coefficient (N/H) at different hole concentration calculated using Eq. 5 and 6 with inputs from first-principles calculations. d) Magnetic field dependence of the Nernst coefficient (N)

$$+ \begin{bmatrix} B(H)_{xx} & B(H)_{xy} \\ B(H)_{yx} & B(H)_{yy} \end{bmatrix} \begin{bmatrix} -\frac{\partial_x T}{T^2} \\ -\frac{\partial_y T}{T^2} \end{bmatrix} \quad (2.2)$$

Assuming there is no temperature gradient along the y -direction (isothermal condition for the Nernst coefficient), for a rhombohedral single crystal of Bi_2Te_3 , which is an isotropic structure, Eq. (2.2) can be simplified as follows:

$$J_x = \sigma_{xx} E_x + \sigma_{xy} E_y - \frac{B_{xx}(H)}{T^2} \partial_x T \quad (2.3)$$

$$J_y = \sigma_{yx} E_x + \sigma_{yy} E_y - \frac{B_{yx}(H)}{T^2} \partial_x T \quad (2.4)$$

where σ and $B(H)$ are the response function tensors defined as:

$$\sigma_{ij} = q^2 \int \tau v_i v_j \left(-\frac{\partial f_0^k}{\partial E} \right) \frac{d^3 k}{4\pi^3} \quad (2.5)$$

$$[B(H)] = \frac{q}{T} \int (E_k - \mu) \frac{\partial f_0^k}{\partial E} \frac{\tau}{(1 + \mu H)^2} \times$$

$$\begin{bmatrix} v_x^2 & v_x v_y - v_x^2 \mu H & v_z v_x \\ v_x v_y + v_y^2 \mu H & v_y^2 & v_z v_y \\ v_z v_x & v_z v_y & v_z^2 (1 + \mu^2 H^2) \end{bmatrix} \frac{d^3 k}{4\pi^3} \quad (2.6)$$

The Nernst coefficient is defined under open-circuit conditions when the electrical current is zero in all directions and the magnetic field is applied only along the z -axis. In these circumstances, eliminating E_x using Eq. (2.3) and Eq. (2.4), and using the definition of the isothermal Nernst coefficient, we find:

$$N_{xyz} = \frac{E_y}{\partial_x T} = \frac{1}{T^2} \frac{\sigma_{xx} B_{yx} - \sigma_{yx} B_{xx}}{\sigma_{xx} \sigma_{yy} - \sigma_{yx} \sigma_{xy}} \quad (2.7)$$

To estimate the Nernst coefficient, we used the band structure and the differential conductivity calculated using first-principles calculations as described in the computational details section. The experimental mobility was used in Eq. (2.5). The Nernst

coefficient computed from Eq. (2.6) is plotted in Fig. 2.5c and compared with the experimental data. The current calculation is performed under constant relaxation time approximation, assuming that the relaxation times do not change under an externally applied magnetic field. However, Smith *et al.* [138] have shown that the changes in the relaxation times versus the magnetic field add another term in the Nernst coefficient. Hence, we believe that the main discrepancy between the theory and experiment is the constant relaxation time approximation used in the theory. Finally, we note that Fig. 2.5c confirms that the general trend an increase in the Nernst coefficient at lower carrier concentrations, lower temperatures, and larger magnetic fields as reported in other materials [77] is also valid for this material. The non-linearity vs magnetic field, as can be seen in Fig. 2.5d, is strongest at the lowest measured temperature, 55 K, pointing to the suitability of the Nernst effect in cryogenic energy conversion application.

2.4 Conclusion

In summary, we have studied the Nernst coefficient, magneto-Seebeck, and magnetoresistance of single-crystal Bi_2Te_3 under the effect of an external magnetic field (< 3 T) and temperature (55 K to 380 K). The Nernst coefficient changes its sign at about 255 K as predicted by the Moreau's relation. It shows a non-linear trend versus the applied magnetic field at low temperatures. The non-linearity gradually increases as the temperature decreases. The magnitudes of the magneto-Seebeck and magnetoresistance were also found to increase as the temperature was decreased. First-principles calculations along with constant relaxation time approximation (CTRA) were used within the framework of BoltzTrap to calculate the Seebeck coefficient and it is in close agreement with the experimentally measured values. The formalism developed by Behnia and Smith was used to calculate the Nernst coefficient of the sample. The theoretical calculations can successfully explain the trends observed in the experiment but are not in quantitative agreement. The discrepancy is attributed to the use of CRTA. Our experimental data and theoretical calculation confirm that the material under study shows the general trend of exhibiting higher values of the Nernst and magneto-Seebeck coefficients at higher mobility values. Our theoretical results show that the magnitude of the Nernst

coefficient is larger at lower temperatures, lower carrier concentrations, and larger magnetic fields. These observations could prove useful in evaluating the Nernst coefficient in other materials having similar band structures as that of Bi_2Te_3 .

Chapter 3

Nernst response in the CDW and the normal phase of 1T-TiSe₂

Collaborators and Personal Contributions: The single crystals employed in this study were procured from HQ Graphene, a crystal growth company located in the Netherlands. All electrical, thermoelectric, and thermomagnetic characterizations were conducted independently by Md Sabir Akhanda, under the supervision of Dr. Mona Zebarjadi.

3.1 Background and context

Semimetals represent a distinctive class of materials that exhibits slight overlap between their valence and the conduction band, accompanied by a high degree of carrier compensation. The presence of two types of carriers, electrons, and holes, results in a smaller Seebeck coefficient compared to conventional semiconductors. Consequently, semimetals have often been overlooked in thermal-to-electrical energy conversion applications utilizing thermoelectric principles. However, the presence of the high carrier compensation renders them promising candidates for alternative thermal-to-electrical energy conversion routes such as thermomagnetic devices based on the Nernst effect. Additionally, the occurrence of a phase transition can induce sharp changes in materials properties corresponding to a large Thomson response. Consequently, semimetals undergoing phase transitions emerge as compelling candidates for exploring the relevant transport parameters governing these two effects.

Here we study 1T-TiSe₂, a layered semimetal with the space group $P\bar{3}m1$. The hexagonal unit cell comprises one Ti and two Se atoms, with a near-identical Se-Se distance within and between layers. Upon cooling, the material undergoes a CDW phase transition at around 200 K [139–141]. Accompanied by this transition, a doubling of lattice parameters to those in the high-temperature phase occurs [139, 141]. Band-type Jahn-Teller mechanism [142, 143], excitonic electron-hole interaction [144], and a combination of both [145] have been argued to drive this transition. A degree of uncertainty seems to be prevalent regarding the band gap in these two phases. Early works claim stoichiometric 1T-TiSe₂ is a semimetal due to the overlap of Se-4p valence band in Γ and the Ti-3d conduction band in L direction [146, 147]. Few studies classify 1T-TiSe₂ as semiconductors in both phases [148–150]. Despite historical discrepancies, modern research tends to converge toward similar conclusions. At elevated temperatures, a positive or negative (i.e., overlap) indirect gap between Se-4p and Ti-3d bands exists which, upon cooling the system, increases or leads to a gap opening, due to the CDW state-induced distortions at the low temperature [151–153].

This study aims to explore the thermoelectric potential of 1T-TiSe₂ by investigating three key effects: the Seebeck effect, the Nernst effect, and the Thomson effect. Thermoelectric devices primarily rely on the Seebeck effect for energy conversion, whereas thermomagnetic devices harness the Nernst effect. While traditional thermoelectric devices rely solely on the Seebeck effect and require both n-type and p-type materials, thermomagnetic devices exploit the Nernst effect and can operate with a single material. By leveraging the unique properties of 1T-TiSe₂ and its phase transition dynamics, this research seeks to elucidate its suitability for efficient thermal-to-electrical energy conversion across multiple thermoelectric phenomena.

3.2 Results and discussion

Temperature-dependent thermoelectric property measurements can provide useful insights into the underlying transport mechanism, serving as foundational knowledge in analyzing the behavior of the Thomson coefficient and the Nernst coefficient within a material. Fig. 3.1(a-d) shows the T-dependent variation in the resistivity (ρ), its derivative

to the first order, the Seebeck coefficient (S), and the thermal conductivity (κ) of TiSe_2 . In Fig. 3.1(a), a distinct peak signifies the transition between the high-temperature normal phase and the low-temperature charge density wave (CDW) phase. The normal phase exhibits either a negligible bandgap on the order of 10 meV or a small overlapping band [154]. Consequently, thermally activated carriers involving the generation of electrons and holes dominate the charge transport in this region. With the number of electrons and holes approximately the same but, holes exhibiting an order of magnitude higher mobility [154], holes-dominated transport is seen in this bipolar region. In a system with two types of charge carriers, the total electrical conductivity (σ) is the combined effect of both electrons and holes:

$$\sigma = \sigma_n + \sigma_p$$

Likewise, the Seebeck coefficient (α) is a weighted average of the individual Seebeck coefficients associated with electrons and holes:

$$\alpha = \frac{\alpha_n \cdot \sigma_n + \alpha_p \cdot \sigma_p}{\sigma_n + \sigma_p}$$

Since the Seebeck coefficients for electrons and holes have opposite signs, the resulting α can be relatively small.

The heat flow in this two-carrier system also has contribution from this bipolar effect as shown below:

$$\mathbf{j}_{n,p} = \beta_{n,p} \mathbf{E} - \kappa'_{n,p} \nabla T$$

Here: - $\mathbf{j}_{n,p}$ represents the heat flow due to electrons or holes. - $\beta_{n,p}$ accounts for the electric field's effect on the heat current. - $\kappa'_{n,p}$ is the thermal conductivity associated with electrons or holes.

The total electronic thermal conductivity (λ) in this system is:

$$\lambda = \lambda_n + \lambda_p + \frac{\sigma_n \sigma_p}{\sigma_n + \sigma_p} (\alpha_n - \alpha_p)^2 T$$

This equation reveals an intriguing aspect: the total electronic thermal conductivity is not simply the sum of the individual thermal conductivities of electrons and holes.

There exists an additional term related to the bipolar flow, which can significantly exceed the contributions from either λ_n or λ_p [155].

With the onset of the CDW transition, as we go lower in T , a reduction in the electron and hole concentration is observed as reported by [154]. This reduction is attributed to the condensation of electrons and holes into the CDW pair state [154] leading to a gradual increase in resistivity until a peak is reached. The derivative of ρ as seen in Fig. 3.1(b) has a sharp minimum which marks the CDW phase transition temperature (T_{CDW}). Concurrently, around the temperature where the reduction ceases, both electrons and holes experience enhancement in mobility [154]. This causes a gradual decrease in resistivity as we go toward lower temperatures. Simultaneously, the concentration of electrons rises by an order of magnitude in this phase making the transport electron dominated [154]. A two-band model with a small overlap in the normal phase and a narrow bandgap in the CDW phase [150, 151] has been reported to explain this resistivity trend [154]. Temperature-dependent Seebeck coefficient (S) further supports this conclusion. As we see in Fig. 3.1(c), S of TiSe_2 at the high temperature is positive, aligning with the hypothesis of a hole-dominated transport at this phase. The magnitude of S is relatively small compared to conventional semiconductor thermoelectric materials. It changes its sign at around 365 K. These observations point to a high degree of carrier compensation and competition between the electron and hole in deciding the sign of S . A gradual sign change and increase in the magnitude of S in the negative direction as temperature decreases further supports the conclusion that the system is transitioning from hole-dominated to electron-dominated transport. Ultimately, S reaches a maximum of $173 \mu\text{V.K}^{-1}$, a remarkably high value that supports the existence of a band gap in the CDW phase. Temperature-dependent thermal conductivity (Fig. 3.1(d)) exhibits an exponential increase as we go lower in temperature from the start of the CDW phase which is probably due to a decrease in the anharmonic phonon scattering [35]. Above T_{CDW} temperature, a small and consistent linear increase in thermal conductivity can be observed. This further affirms the hypothesis of the generation of thermally activated carriers and consequently a bipolar transport in this region.

Thomson and Nernst effect, two relatively less explored thermal to-electrical conversion phenomena recently attracted increased attention in phase change materials

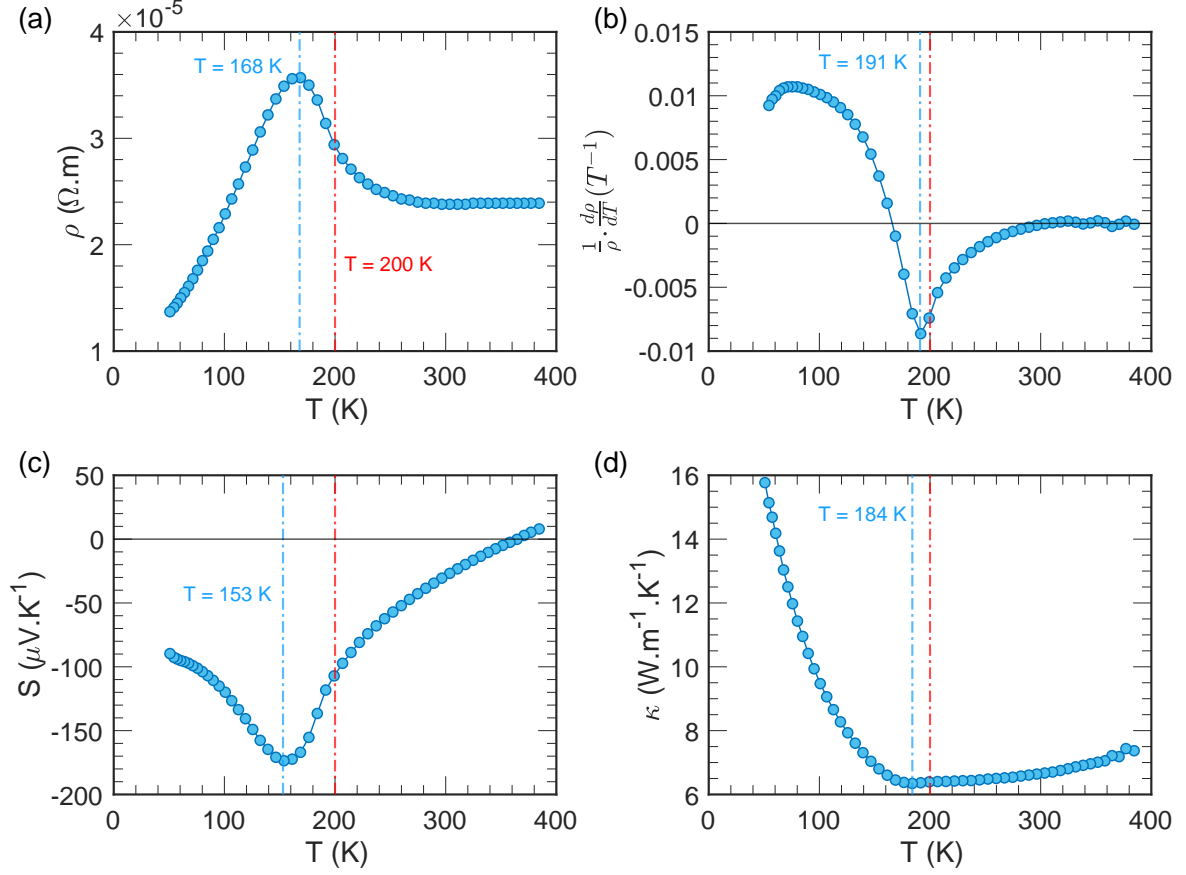


Figure 3.1: Temperature dependent variation in the a) electrical resistivity (ρ), b) $(1/\rho) \cdot (d\rho/dT)$, c) the Seebeck coefficient (S), and d) the thermal conductivity (κ) of single crystal 1T-TiSe₂. The red-colored vertical dotted lines mark $T = 200$ K while the blue-colored vertical dotted lines mark the maxima or minima of the T-dependent curves.

and semimetals respectively [35, 41, 156, 157]. Temperature-dependent responses of these two effects are plotted in Fig. 3.2(a-c). The Thomson coefficient (τ) as plotted in Fig. 3.2(a) is defined as the product of the average sample temperature and the first derivative of the Seebeck coefficient. While the magnitude of S monotonically changes from $-26 \mu V \cdot K^{-1}$ to $-8 \mu V \cdot K^{-1}$ between 300 K to 385 K, the τ show a relatively flat response with an average magnitude of $147 \mu V \cdot K^{-1}$. With the commencement of the CDW phase which induces an even sharper change in the Seebeck coefficient, the scenario improves even more. The sharpest dS/dT is recorded at 184 K where we also see the τ to reach its maximum of $450 \mu V \cdot K^{-1}$. Other than FeRh, this value exceeds the τ peak in

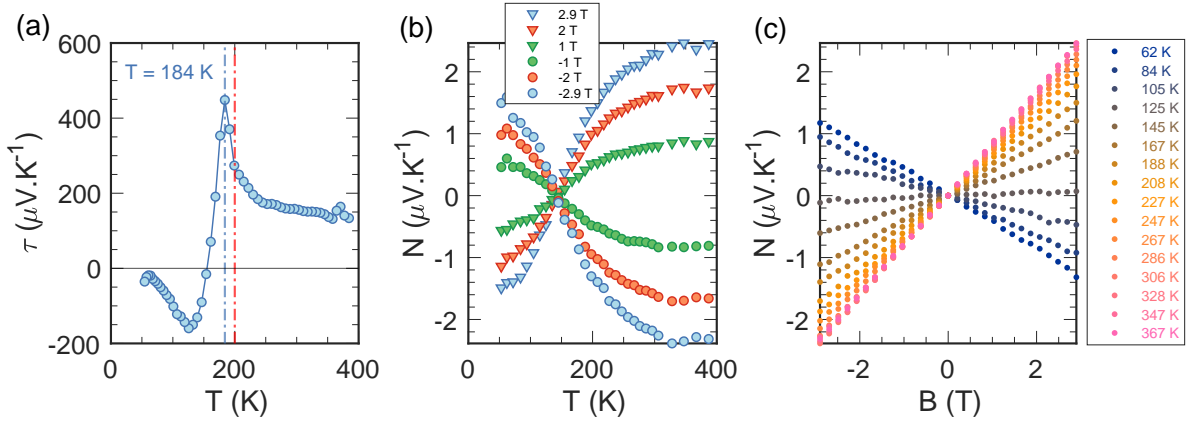


Figure 3.2: Temperature-dependent variation in a) the Thomson coefficient (τ) and b) the Nernst coefficient (N). c) Magnetic field-dependent variation in the Thomson coefficient (τ) and the Nernst coefficient (N).

other materials such as Ni ($16 \mu\text{V}\cdot\text{K}^{-1}$), $\text{Bi}_{88}\text{Sb}_{12}$ ($45 \mu\text{V}\cdot\text{K}^{-1}$), p-type Bi_2Te_3 ($150 \mu\text{V}\cdot\text{K}^{-1}$), MoTe_2 ($111 \mu\text{V}\cdot\text{K}^{-1}$) [35, 157–159]. τ of TiSe_2 surpasses that of Seebeck coefficient as that observed in MoTe_2 . Using the Thomson figure of merit $(\tau^2 T)/\kappa\rho$ defined by Zebajadi et al. [160] we obtain a $zT(\text{Thomson})$ peak of 0.173 (see Fig. 3.3). Compared with the thermoelectric zT (see Fig. 3.3), this is approximately a 10 times enhancement. At even lower temperatures, with the change in the S trend, τ changes direction too, eventually flipping its sign at 154 K where S peaks and ultimately reaching a negative peak of $160 \mu\text{V}\cdot\text{K}^{-1}$ at 125 K. Interestingly, temperature-dependent Nernst coefficient (see Fig. 3.2(b)) changes sign approximately around 150 K which is also very close to the temperature at which S peaks (154 K). This matches with the prediction made by Moreau [126]. From the magnetic dependent behavior (see Fig. 3.2(c)), we see the N to remain linear. Under Jones-Zener expansion, a non-linear behavior can arise if the product of mobility and applied magnetic field far exceeds 1 [161]. Consequently, we can conclude that the mobility of carriers is not high enough in both the normal and CDW phase, an observation that matches with other's Hall measurements [154, 162]. These Hall measurements predict higher mobility in the CDW phase compared to the normal phase. To be precise, for electrons, the enhancement is by more than an order of magnitude, and for holes, it is by a few times. Historically, mobility enhancement has been reported to drive an increment in N [42, 163, 164]. But, strikingly, we see a larger

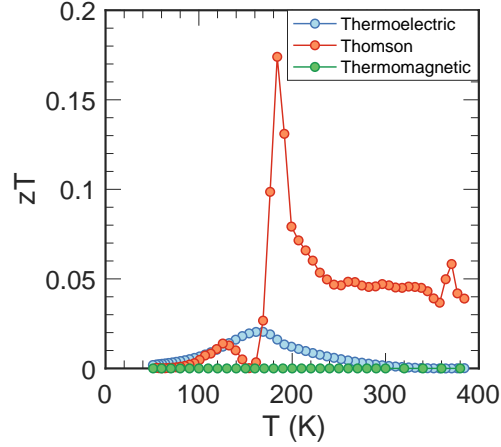


Figure 3.3: Temperature-dependent a) thermoelectric, b) Thomson, c) thermomagnetic figure of merit (zT).

N in the normal phase where the mobility is the lowest. Thus, a clear argument can be made that this enhancement did not stem from mobility. Interestingly enough, this 150 K also marks the temperature where an abrupt reconstruction of the Fermi surface commences driving a rapid increase in the electron-holes pockets in the normal phase as reported by Knowles et al. [154]. This leads to an increased bipolar effect which is advantageous for the Nernst configuration as opposed to the Seebeck configuration. Thus, TiSe_2 sets a clear example of bipolar conduction-induced Nernst coefficient in semimetal. Though it is generally assumed that the bipolar effect is advantageous for the Nernst effect a clear experimental demonstration is not common in the field since N is often complicated by other material parameters. The only other reports that we could find that reports such a clear demonstration of the influence of the bipolar effect is in the case of the quasi-One-dimensional metal $\text{Li}_{0.9}\text{Mo}_6\text{O}_{17}$ [40] by Cohn et al. and for the case of Cd_3As_2 semimetal [37]. $\text{Li}_{0.9}\text{Mo}_6\text{O}_{17}$ shows a diminishing N trend with increasing temperature, a common observation the field [39, 163–167]. On the contrary, we see an increasing trend going as high as 367 K, another interesting and very uncommon observation. The only other study that reported such an increasingly high N response is in Cd_3As_2 . This unique behavior questions the conventional thinking that the Nernst response is expected to be higher at lower temperatures and provides encouragement for the design of high-temperature thermomagnetic devices built based on the Nernst

effect.

3.3 Conclusion

In conclusion, 1T-TiSe₂ presents an interesting case for thermal-to-electrical energy conversion through multiple thermoelectric phenomena. The material transitions from hole-dominated to electron-dominated transport upon cooling, reaching a peak of $173 \mu\text{V.K}^{-1}$ in the CDW phase. The Thomson zT exhibits a tenfold enhancement compared to the thermoelectric zT . The Nernst coefficient (N) also presents a unique behavior, increasing as temperature decreases, indicating the influence of bipolar transport. These findings open avenues for designing high-performance thermomagnetic devices, particularly leveraging the Nernst effect, in semimetals like 1T-TiSe₂.

Chapter 4

Nernst effect in the type II Weyl semimetal $\text{Mo}_{1-x}\text{W}_x\text{Te}_2$

Collaborators and Personal Contributions: Single-crystals used in this study were grown by Dr. Sergiy Krylyuk from Dr. Albert Davydov's group at the National Institute of Standards and Technology. The electrical, thermoelectric, and thermomagnetic characterizations were all done by Md Sabbir Akhanda under the supervision of Dr. Mona Zebarjadi.

4.1 Background and context

Transition metal dichalcogenides (TMDCs) are a large family of layered materials with the chemical formula MX_2 where M is a transition metal (e.g., Mo, W, Nb, Ta, Ti, Zr, Hf, etc.) and X is a chalcogen atom (e.g., S, Se, Te) [168]. Each unit layer is composed of three sheets of atoms arranged in the $X - M - X$ configuration with the metal atoms in the middle and the chalcogen atoms on the two sides. The layers are held together by a weak van der Waals interaction [169]. Depending on coordination in $X - M - X$ layers and stacking orders along the c -axis, TMDCs can exist in different phases like 1T, 2H, 3R, and T_d . Over 40 different TMDCs have been discovered so far [170]. These materials together with their different polymorphs have been found to show diverse electronic and photonic properties. In recent years, some of the TMDCs that are lacking either space or time inversion symmetry have been experimentally proven to host the Weyl semimetallic state, a non-trivial symmetry-protected topological phase of matter characterized by a

pair of degenerate Weyl cones of opposite chirality with linear dispersion around the Weyl nodes in the bulk and Fermi arcs on the surface [171–173]. These TMDCs are particularly interesting because of the many topologically induced exotic properties such as extremely large magnetoresistance [174–180], superconductivity [181–187], and planar and spin-Hall effect [188–190] observed in the Weyl semimetals so far. The crystalline to crystalline polymorphic structural transitions reported in some of these materials has helped garner even more interest from emerging fields like neuromorphic computing [191], and phononic and thermal logic devices [192]. In particular, MoTe_2 [193–196], and $\text{Mo}_{1-x}\text{W}_x\text{Te}_2$ alloys [197, 198] are known to be type II Weyl semimetals (i.e., the Weyl cones are tilted in the momentum space leading to the breaking of the Lorentz symmetry) [199, 200] exhibiting a crystalline-to-crystalline phase transition and are the focus of this paper.

MoTe_2 has three polytypes: $2H$ (space group $P6_3/mmc$), $1T'$ (space group $P2_1/m$) and T_d (space group $Pmn2_1$) [201–203]. The semiconducting $2H$ phase is the thermodynamically preferred state at room temperature. The monoclinic $1T'$ phase is naturally stable above 900 °C but can also be stabilized at room temperature by employing techniques such as rapid cooling, tellurization rate control, or appropriate precursor selection for the chemical vapor deposition [204]. Upon cooling, the $1T' - \text{MoTe}_2$ undergoes a first-order phase transition around 250 K to the orthorhombic T_d phase which is a type-II Weyl semimetal [182, 203, 205, 206]. The degree of substitution of molybdenum by tungsten controls the phase in which the $\text{Mo}_{1-x}\text{W}_x\text{Te}_2$ alloys exist at room temperature (pure $1T'$: $x \leq 0.1$, mixed $1T' + T_d$: $0.1 < x < 0.6$ and pure T_d : $x \geq 0.6$) [207].

Here, we study pure MoTe_2 and $\text{Mo}_{1-x}\text{W}_x\text{Te}_2$ alloys with $0 \leq x \leq 0.08$ and at first demonstrate the potential of the Seebeck coefficient as an efficient tool for probing the thermal hysteresis induced by a phase transition from the $1T'$ phase to the T_d phase. Three separate measurements: X-ray diffraction (XRD), electrical resistivity, and Seebeck coefficient are presented to support this case. Then, we report a topologically induced enhancement of the Nernst coefficient in the temperature range of 2 K – 50 K and phase-transition induced enhancement of the Thomson coefficient. Finally, we report the effect of W substitution on the thermoelectric transport behavior of the $\text{Mo}_{1-x}\text{W}_x\text{Te}_2$ alloys.

4.2 Results and discussion

4.2.1 Seebeck coefficient as a phase transition probe

We employ three different measurements (XRD, electrical resistivity, and Seebeck coefficient) to investigate the thermal hysteresis induced by the $1T' - T_d$ structural phase transition in MoTe_2 (see Fig. 4.1). The hysteresis observed in the monoclinic β - angle during temperature-dependent XRD measurements is a direct probe of structural phase transition. As shown in Fig. 4.1a, during the cooling half-cycle, the β -angle remains constant up to 260 K and then gradually changes from 93.92° to 90° between 260 K and 210 K indicating the presence of both phases in this temperature range. It remains at 90° , a signature of the orthorhombic T_d phase, up to 130 K. On the warming half-cycle, the sample goes through the reverse $T_d - 1T'$ transition with β -angle changing its value gradually from 90° to 93.92° within the temperature range of 257 K to 300 K. This range is different from what we observed in the cooling half-cycle. Thus, tracking the β -angle over the full thermal cycle, we obtain a hysteresis extending over the temperature range of 210 K to 300 K [208]. It is to be noted that, tracking the β -angle, Clarke et al. reported a hysteresis over a shorter temperature range (233 K to 280 K) compared to this work [203]. Using the van der Waals density functional method, it has been shown that the T_d phase is energetically more stable than the $1T'$ phase and the energy difference between these two phases in MoTe_2 is 0.4 meV per unit cell. Calculation of free energy of the two systems (to include the temperature effects) showed a lower energy of $1T'$ phase at temperatures above 150 K. While the 150 K is lower than the experimentally measured phase transition temperature, the calculations confirm the structural phase transition. The origin of the phase transition is related to the interlayer bonding states near the Fermi energy and can be tuned by charge doping [208].

Dahal et al. studied the $1T' - T_d$ phase transition in MoTe_2 using resistivity data [209]. They defined the phase-transition temperature (T_s) as the temperature where $\frac{d\rho(T)}{dT}$ maxima occurs and reported $T_s \approx 249$ K in the cooling half-cycle [209]. They observed a thermal hysteresis extending from 150 K to 300 K (their highest measured temperature). However, at 300 K their hysteresis loop did not converge meaning that the hysteresis probably would have ended at a higher temperature. The thermal hysteresis loop we

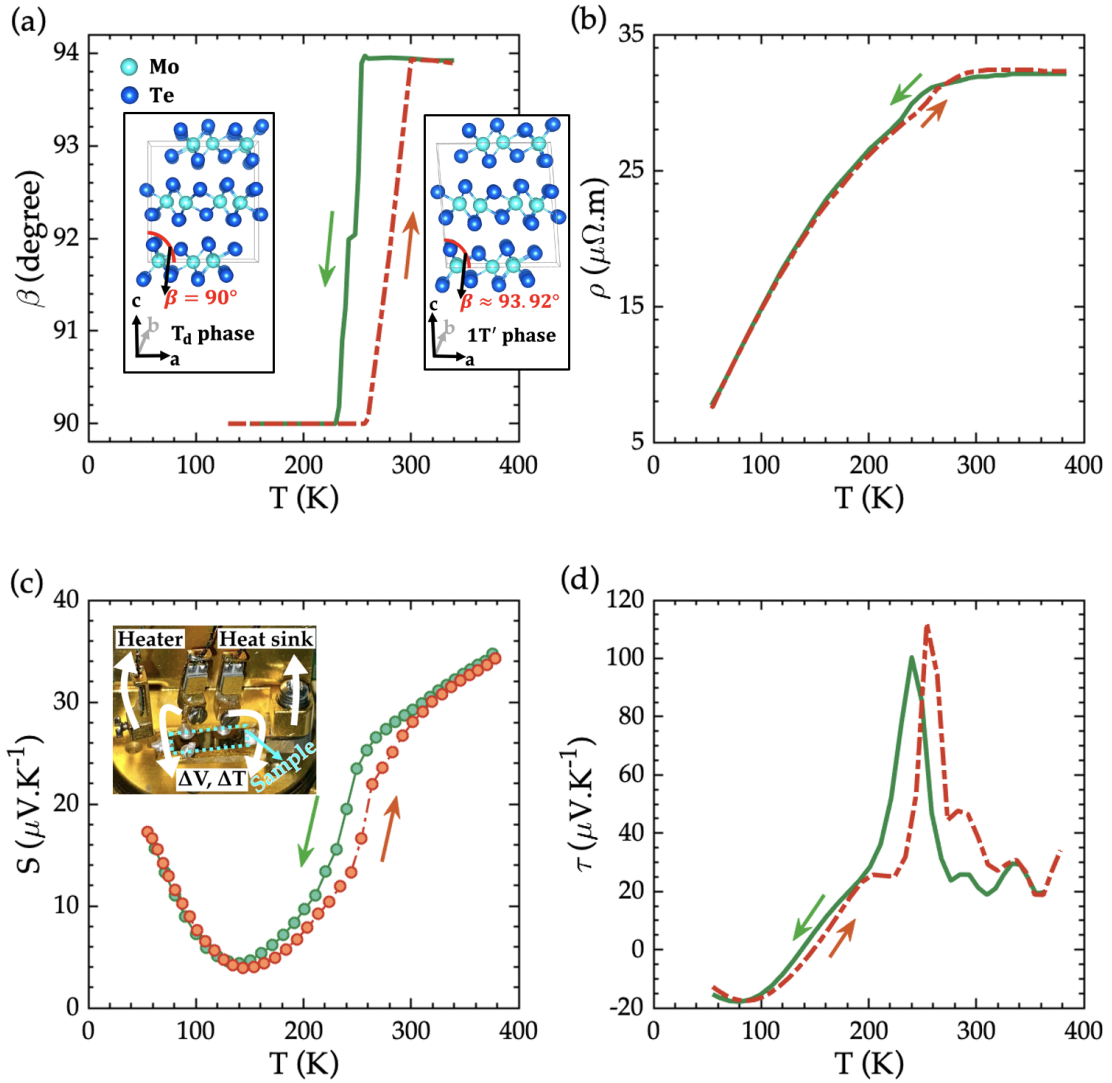


Figure 4.1: Temperature dependence of the a) monoclinic angle β , b) resistivity, c) Seebeck coefficient, and d) Thomson coefficient of MoTe₂ over the cooling (solid line) and warming (dashed line) half-cycles. Inset in Fig. 4.1a shows the crystal structure of T_d and $1T'$ phases of MoTe₂ with their respective β angle indicated. Inset in Fig. 4.1c shows a sample mounted on the sample holder (puck) for measurement.

observed in the temperature-dependent resistivity measurement (Fig. 4.1b) is slightly different from the one reported by Dahal et al. and extends from ~ 230 K to ~ 330 K. The magnitude of the change in resistivity across the thermal hysteresis is small as evident from the graph because both $1T'$ and T_d phases are semimetallic. When the change in electrical resistivity is small, e.g., a semimetal-semimetal phase transition in MoTe₂, the probability of the measurement errors playing a deteriorating effect increases, making

it challenging to study the phase transition. Thus, resistivity measurement does not always best portray the underlying changes. On the contrary, as seen in Fig. 4.1c, the effect of such phase change on the magnitude of the Seebeck coefficient obtained from a temperature-dependent measurement is noticeably pronounced and resulted in a clear hysteresis spanning from approximately 134 K to 345 K. This is a clear indication that the Seebeck coefficient is a better probe than resistivity for studying temperature-driven structural phase changes in materials. It is known that while the electrical conductivity is influenced both by the band structure and the carrier lifetimes, the Seebeck coefficient to the first-order approximation, depends only on the band structure and is not sensitive to the details of the lifetimes. Both the T_d and $1T' - MoTe_2$ phases contain multiple electron and hole pockets [174] and the balance in the electron-hole contribution is modified through the phase transition. This is not observable in resistivity measurement as both electrons and holes contribute a positive resistance. It shows well in the Seebeck measurement as the electrons and holes have different Seebeck signs and therefore the Seebeck measurement can determine the relative change in the electron-hole concentration effectively. Thus, the Seebeck coefficient both theoretically and as shown experimentally in Fig. 4.1c, is a better probe for studying the temperature-dependent phase change in $MoTe_2$. It is important to acknowledge here that, though the effect of the carrier lifetime is secondary, we cannot completely discard it playing a role in the Seebeck coefficient measurement.

Phase-transition-induced enhanced variation in the Seebeck coefficient results in a large Thomson coefficient in $MoTe_2$. Similar enhancements have been recently reported in the case of $FeRh$ [156]. Thomson heating/cooling is a nonlinear response and is proportional to the product of an applied electrical current and temperature gradient. The Thomson coefficient τ of a material at a given temperature T , is defined as the product of the sample temperature and the first derivative of the Seebeck coefficient with respect to T [210]. The Thomson effect enables cooling/heating in homogenous samples, allowing for simpler device design. This effect is usually small compared to the normal Seebeck effect and hence has not been studied widely. As seen in Fig. 4.1d, the steep variation in the Seebeck coefficient due to phase change results in a τ of $111 \mu V K^{-1}$ at 254 K (warming half-cycle). The presence of hysteresis is reflected in peaks appearing at different

temperatures of the cooling and warming half-cycles. Our observed magnitude is significantly greater than what was reported for Ni ($-16 \mu\text{VK}^{-1}$) and $\text{Bi}_{88}\text{Sb}_{12}$ ($45 \mu\text{VK}^{-1}$) and is comparable to the one observed in a p-type Bi_2Te_3 ($150 \mu\text{VK}^{-1}$) [157, 211]. We note that the Seebeck coefficient values of Ni, $\text{Bi}_{88}\text{Sb}_{12}$ and p-type Bi_2Te_3 are larger than their respective Thomson coefficients. This is not the case for MoTe_2 studied here that demonstrates Thomson coefficient values that are an order of magnitude larger than the Seebeck coefficient.

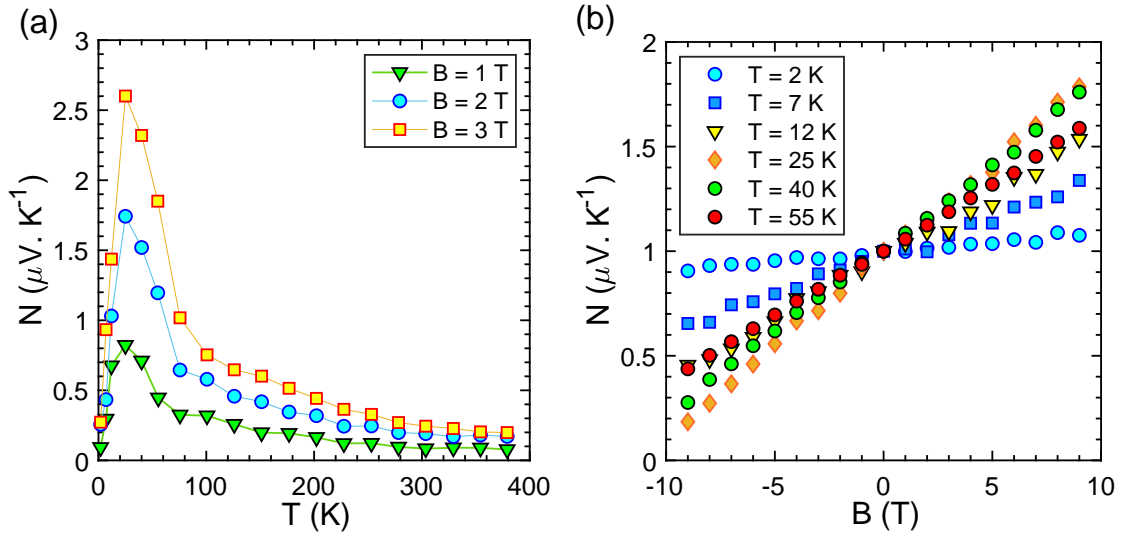


Figure 4.2: a) Temperature and b) magnetic field dependence of the Nernst Coefficient of MoTe_2

4.2.2 Nernst coefficient at low-temperature

The Nernst effect is important thermomagnetic effect for directly converting thermal energy to electrical energy and cooling. In this effect, a voltage is generated in response to the presence of a magnetic field applied perpendicular to a thermal gradient such that the direction of the voltage, thermal gradient, and magnetic field are all orthogonal to each other [46]. Since, the Lorentz force exerted by the magnetic field pushes mobile carriers with opposite charges to the opposite sides, the contribution of the electrons and holes are additive in setting the magnitude of the Nernst coefficient (N). Consequently, two-carrier systems like Dirac and Weyl semimetals are promising candidates

for thermomagnetic applications [37, 163, 164, 212]. Similar to the Thomson modules, the Nernst modules can use a single homogenous material. This is in contrast to the thermoelectric modules that are always using a p-n pair.

Here, we investigated the temperature and magnetic field dependence of the Nernst coefficient (N) of MoTe_2 from 380 K to 2 K (see Fig. 4.2). At room temperature (300 K), the magnitude of N is $\approx 0.084 \mu\text{VK}^{-1}\text{T}^{-1}$. With decreasing temperature, the value of N increases and ultimately peaks at ≈ 25 K. At this temperature, the value of N is found to be $0.82 \mu\text{VK}^{-1}\text{T}^{-1}$ which is about 10 times larger than that observed at 300 K. Further decrease in the temperature leads to a rapid decrease in N . Since the Nernst coefficient increases at lower temperatures due to higher mobility [35, 89], this rapid decreasing trend is not generally expected [38] and serves as an indication that there are additional factors to be considered. To understand the origin of the peak, a closer look at the band structure of MoTe_2 is required. The semimetallic MoTe_2 has several electron and hole pockets that can be described by quadratic dispersion [174, 175]. Being a Weyl semimetal, the band structure also exhibits linear dispersion around the Weyl nodes. The peak around 25 K marks the region where linear dispersion dominates over the quadratic ones. In the temperature range of 380 K to approximately 100 K, the N is dominated by quadratic bands while in the temperature range from 100 K to 2 K, the effect of linearly dispersive bands gradually appears. In this region, with decreasing temperature, the Fermi level shifts more towards the Dirac point causing the N to rise. When the Fermi level is close to the Dirac point at ≈ 25 K, the enhanced mobility of the charge carriers [174] leads to the largest value of N observed. Further decrease in temperature (25 K to 2 K) moves the Fermi level away from the Weyl point resulting in a subsequent decrease in N . Similar theoretical argument in the case of single-crystal NbP, a Weyl semimetal, has been able to well-replicate the experimental data [164]. Since the phase transition effects and the low-temperature topological effects appearing in MoTe_2 are separated by a sizable temperature gap, we do not anticipate one affecting the other. The addition of W shifts the phase transition to a higher temperature as reported in the literature [209], further ruling out any interplay between these two effects when W is added. With W addition, we did not observe any noticeable change in the temperature dependence of the Nernst coefficient (see Fig. 4.3). The magnetic field dependence of the

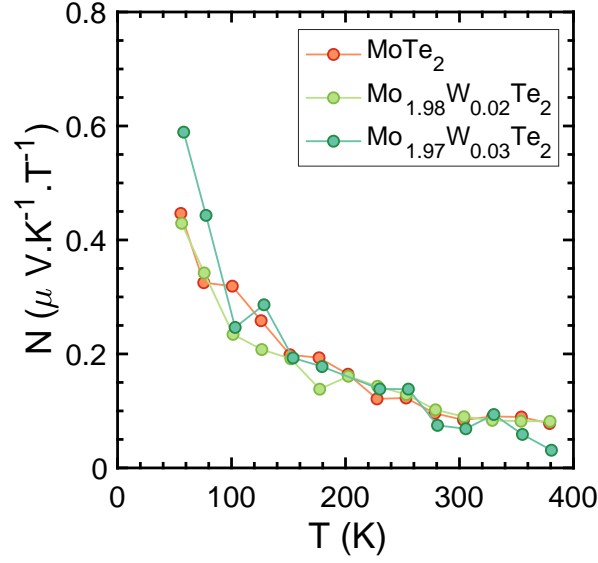


Figure 4.3: Temperature dependence of the Nernst coefficient at varying W concentration

Nernst coefficient is plotted in Fig. 4.2b. Using the Jones-Zener expansion, one can show that N enters into a non-linear response region when the product of carrier mobility (μ) and magnetic field (B) is much larger than unity [161]. The Nernst coefficient of MoTe_2 , as can be seen in Fig. 4.2b, maintains a linear response in the entire range of the applied magnetic field (up to 9 T). This observation conveys that the mobility of electrons and holes is not high in MoTe_2 , as in e.g., NbP [164]. It is not uncommon to see such a quasi-linear unsaturated behavior of N in semimetals [164]. In fact, this behavior is also observed in WTe_2 , a material at the other end of the $\text{Mo}_{1-x}\text{W}_x\text{Te}_2$ alloy spectrum [163].

4.2.3 Thermoelectric properties at different W content

In order to investigate the effect of W addition, $\text{Mo}_{1-x}\text{W}_x\text{Te}_2$ alloys with $x = 0, 0.02, 0.03, 0.08$ that are in the pure $1T'$ phase at room temperature [207] and then transition to the T_d phase at lower temperatures were studied. The addition of W results in a consistent drop in the resistivity of all the samples which is consistent with previous measurements [209, 213, 214]. The temperature dependence of the resistivity of these samples is shown in Fig. 4.1b and Fig. 4.4(a-c). As the sample temperature is increased from 50 K, an increasing trend ($\frac{d\rho(T)}{dT} > 0$) is observed in the resistivity. At room temperature, the resistivity of $1T' - \text{MoTe}_2$ is $32 \mu\Omega.m$ compared to $(7.5 - 10) \mu\Omega.m$ [181, 209, 214] and

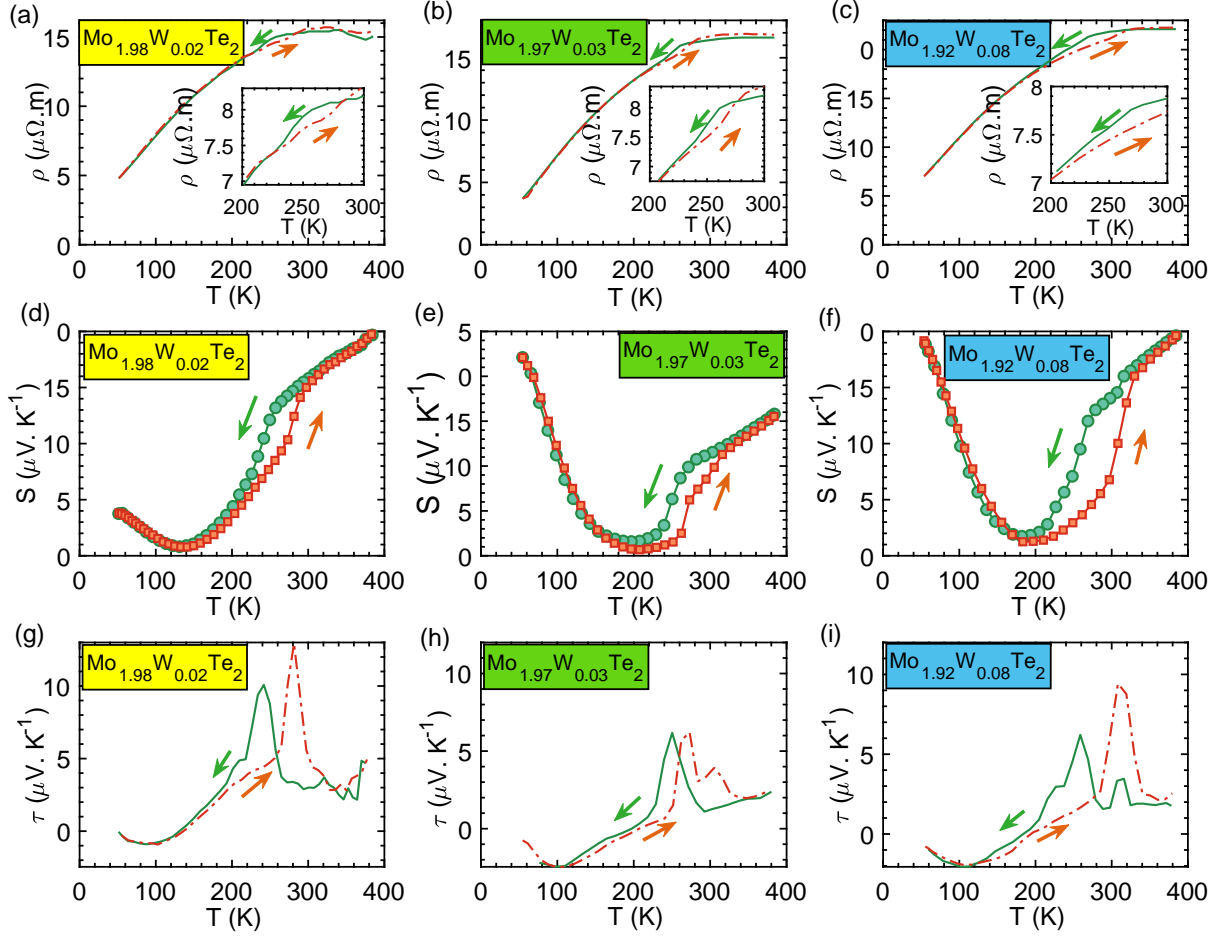


Figure 4.4: Temperature dependence of (a-c) resistivity, (d-f) Seebeck coefficient and (g-i) Thomson coefficient of $\text{Mo}_{0.98}\text{W}_{0.02}\text{Te}_2$, $\text{Mo}_{0.97}\text{W}_{0.03}\text{Te}_2$ and $\text{Mo}_{0.92}\text{W}_{0.08}\text{Te}_2$ over the cooling (solid line) and warming (dashed line) half-cycles

$95 \mu\Omega.m$ [215] which were reported previously for similar samples. Between 200 K to 300 K, all the samples show hysteresis as a consequence of the T_d to $1T'$ phase transition. The center of the hysteresis loop shifts to higher temperatures with an increased molar fraction of W which is consistent with an earlier study [209]. Using $d\rho(T)/dT$ maxima for the cooling half-cycle, $1T' - T_d$ transition temperatures T_s of 240 K, 241 K, 250 K, and 258 K are estimated for MoTe_2 , $\text{Mo}_{0.98}\text{W}_{0.02}\text{Te}_2$, $\text{Mo}_{0.97}\text{W}_{0.03}\text{Te}_2$ and $\text{Mo}_{0.92}\text{W}_{0.08}\text{Te}_2$, respectively (see Fig. 4.5). The shift in T_s occurs due to the interlayer contraction or expansion having the ability to enhance or weaken the hybridization of the Te p_z orbital [214]. Since the atomic size of W is slightly larger than the size of Mo, the addition of W increases the interlayer distance and weakens the hybridization. This results in an

increase in the kinetic energy of the electrons and consequently total energy of the $1T'$ system [216]. As a result, the energy gap between the T_d and $1T'$ phase increases causing a shift of the phase change to a higher temperature.

The temperature dependence of the Seebeck coefficient of all four samples from 55 K to 380 K is shown in Fig. 4.1c and Fig. 4.4(d-f). For all the samples, S is positive at 380 K and follows a resembling trend over the entire temperature range investigated. The magnitude of S for all these samples is small due to the semimetallic nature of the samples and the bipolar transport. For MoTe_2 and $\text{Mo}_{0.98}\text{W}_{0.02}\text{Te}_2$, S is positive throughout the entire temperature range. For the remaining two samples, we observe S to flip sign at an intermediate temperature (110 K – 305 K for $\text{Mo}_{0.97}\text{W}_{0.03}\text{Te}_2$ and 78 K – 320 K for $\text{Mo}_{0.92}\text{W}_{0.08}\text{Te}_2$). The density functional theory (DFT) study has revealed that MoTe_2 has three interconnected hole pockets and four disconnected electron pockets with the electronic band structure remaining temperature independent from 20 K to 130 K [174, 175]. The net size of the hole pockets has been reported to be larger than the net size of the electron pockets [175]. Additionally, with increasing temperature, the size of the electron pockets remains fairly constant while the hole pockets experience the largest change. Taking all these into account, qualitatively we can comment that our experimental results are in agreement with the DFT results as the S of the four samples exhibited predominantly positive behavior over the measured temperature range. The Fermi level changes with temperature, modifying the overall number of electrons and holes contributing to the transport. The valley observed in the Seebeck coefficient at the intermediate temperature is indicative of the competing nature of the electron hole-pockets as the temperature is changing. Like temperature, W addition can also result in moving the Fermi level. From Fig. 4.4(d-f), we can see that the addition of W has gradually lowered the Seebeck coefficient minima recorded in the intermediate temperature range for $\text{Mo}_{0.98}\text{W}_{0.02}\text{Te}_2$, $\text{Mo}_{0.97}\text{W}_{0.03}\text{Te}_2$ and $\text{Mo}_{0.92}\text{W}_{0.08}\text{Te}_2$. Hence, the addition of W increases the contribution of the electron pockets possibly by lowering the size of the hole pockets, consequently lowering the overall Seebeck coefficient. The change in the relative electron-hole pockets can also be attributed to the Lifshitz transition as argued in Ref. [174]. Accordingly, a topological reconstruction of the Fermi surface induces an anomaly in the Seebeck coefficient resulting in a change in the slope of the

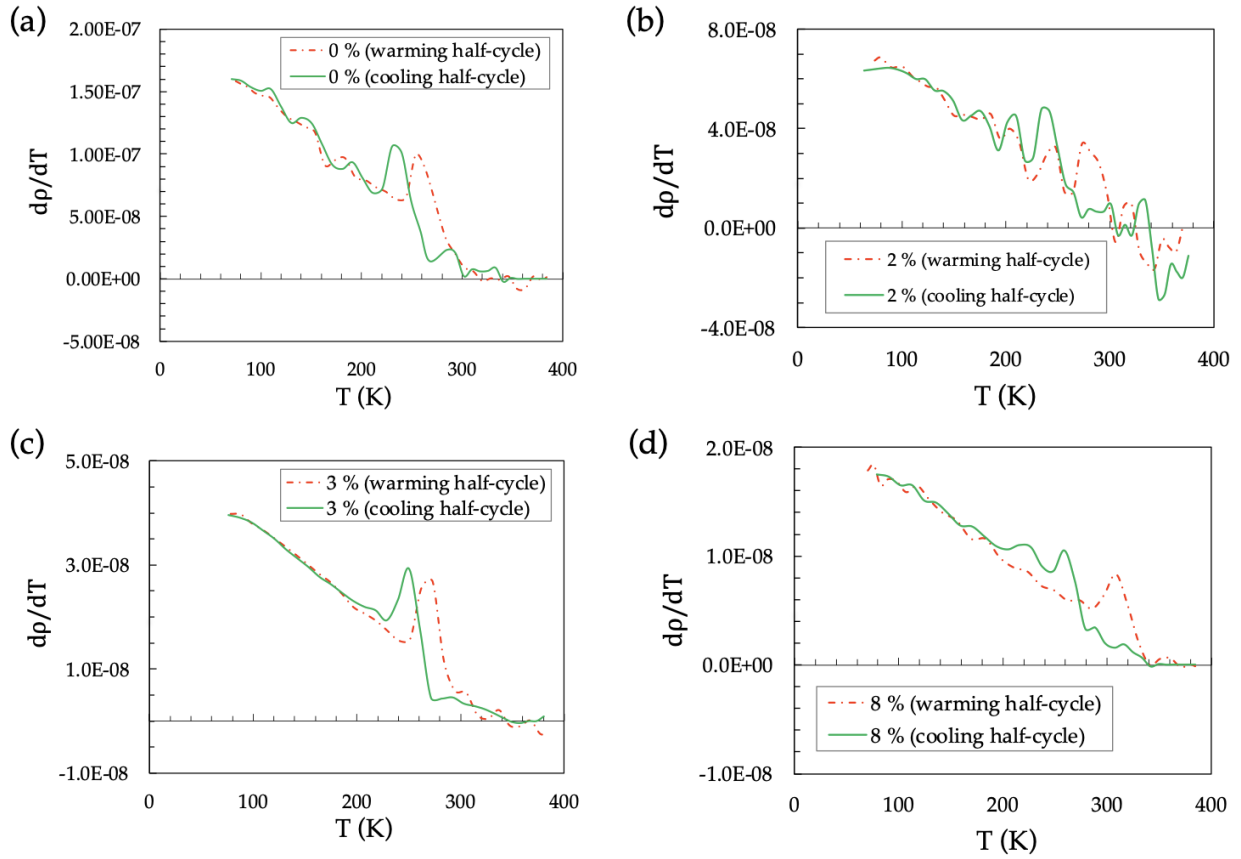


Figure 4.5: Temperature dependence of the $d\rho/dT$ of $\text{Mo}_{0.98}\text{W}_{0.02}\text{Te}_2$, $\text{Mo}_{0.97}\text{W}_{0.03}\text{Te}_2$ and $\text{Mo}_{0.92}\text{W}_{0.08}\text{Te}_2$ over the cooling (solid line) and warming (dashed line) half-cycles

Seebeck coefficient with respect to temperature, dS/dT . Thomson coefficient as shown in Fig. 4.4(g-i) remained higher than the Seebeck coefficient even after the addition of W. $\text{Mo}_{0.98}\text{W}_{0.02}\text{Te}_2$ exhibited the highest Thomson coefficient among these three alloys. The peak of the Thomson coefficient shifts to higher temperatures by increasing the W fraction following the same trend as of the phase transition temperature.

4.3 Conclusion

We demonstrated that the Seebeck coefficient measurement is a better alternative than the resistivity measurement in probing the temperature-dependent $1T' - T_d$ phase transition in MoTe_2 . This is because the carrier lifetime plays a major role in resistivity compared to the Seebeck coefficient. Centering around the temperature where the phase transition occurs, a high Thomson coefficient is observed. The absolute value of the

Thomson coefficient in MoTe_2 is significantly larger than that of the Seebeck coefficient. The Nernst coefficient in MoTe_2 , has a topologically induced peak value of $0.82 \mu\text{VK}^{-1}\text{T}^{-1}$ at approximately 25 K that occurs as a consequence of the position of the Fermi level coinciding with the position of the Dirac points. Investigating the effect of W substitution on the thermoelectric properties of $\text{Mo}_{1-x}\text{W}_x\text{Te}_2$, we observed that an increased W content, from $x = 0.02$ to $x = 0.08$, made the samples more electron-dominant as is evident in the Seebeck measurements, and consistently lowered the resistivity of both $1T'$ and T_d phases. Seebeck coefficient measurement revealed the competing nature of the electron and hole pockets as we change the temperature or alloy MoTe_2 with W.

Chapter 5

Nernst effect in the Dirac semimetal

PdTe_2

Collaborators and Personal Contributions: The single crystals utilized in this study were grown through collaborative efforts between Md Sabbir Akhanda and Dr. Sergiy Krylyuk at the National Institute of Standards and Technology. While Md Sabbir Akhanda contributed to material selection and conducted a literature survey on growth methods, offering preliminary information, Dr. Krylyuk, with his expertise in crystal growth, managed all manual tasks and decision-making processes to refine the parameters and oversee the crystal growth. Md Sabbir Akhanda closely shadowed and whenever necessary assisted Dr. Krylyuk, benefiting from valuable training throughout. Additionally, under the guidance of Dr. Mona Zebarjadi, Md Sabbir Akhanda independently conducted all the Seebeck, and Nernst characterizations. The resistivity measurements below 50 K were performed by Md Sabbir Akhanda and Dr. John Schneeloch in Dr. Despina Louca's lab at the Physics department (UVA).

5.1 Introduction

PdTe_2 is a layered material belonging to the transition metal dichalcogenide family. One Pd atom and two Te atoms of the unit cell are arranged in a hexagonal crystal structure with a lattice constant of $a=4.0365$ and $c=5.1262$ Å [217]. In 2016, Huang et al. predicted the existence of type-II Dirac fermion in PtSe_2 , PtTe_2 , PdTe_2 , and PtBi_2 using first-principles calculations and effective Hamiltonian analysis [218]. In the following

year, employing angle-resolved photoemission spectroscopy and De Haas–van Alphen oscillations, the realization of type-II Dirac fermion in PdTe₂ was confirmed experimentally. [217, 219]. Recently, the thermoelectric properties of hexagonal PdTe₂ structures were theoretically explored [220] following the successful experimental fabrication [221] of PdTe₂ films by Liu et al. The hexagonal monolayer exhibits an indirect band gap of 0.17 eV and a thermoelectric figure of merit (zT) of 0.8 at room temperature. Liu et al. utilized a bottom-up approach to grow high-quality PdTe₂ films on SrTiO₃ (001) by molecular-beam epitaxy [221]. During their investigation into electronic and superconducting characteristics using scanning tunneling microscopy, transport experiments, and first-principles calculations, they observed a shift from the narrow-gap semiconducting state in monolayers to a metallic state in multilayer films, with all multilayer films demonstrating robust superconductivity. DC magnetization and ac susceptibility measurement by Leng et al. reached the same conclusion [222]. Guo et al. investigated the electronic and thermoelectric characteristics of hexagonal PdTe₂ under uniaxial and biaxial strains through first-principles calculations. They found that both types of strain can decrease the bandgap and affect the Pd-d and Te-p orbitals near the Fermi level, prompting a shift from semiconducting to a metallic behavior [223]. Using ab initio calculations, Li et al. investigated the lattice and electronic thermal conductivity of PdTe₂ revealing a room temperature total thermal conductivity of approximately 35 W.m⁻¹.K⁻¹ along the a-axis wherein the lattice thermal conductivity remains below 2 W.m⁻¹.K⁻¹, contributing only around 5% [224].

While it is very encouraging to see an increase in the number of studies on PdTe₂ focusing on the Seebeck effect device-based applications, its thermomagnetic side based on the Nernst effect remains unexplored. Topological semimetals hold promise in thermomagnetic applications due to their unique electronic band structure characterized by linear dispersion. By tuning the Fermi level to cross the Dirac-dispersion point, considerable enhancement in mobility can be achieved. This mobility enhancement in turn can induce an increment in the Nernst response in materials. With this goal in mind, here we study the magnetic field and temperature-dependent variation in the transport properties of PdTe₂, a Dirac semimetal, in the bulk form.

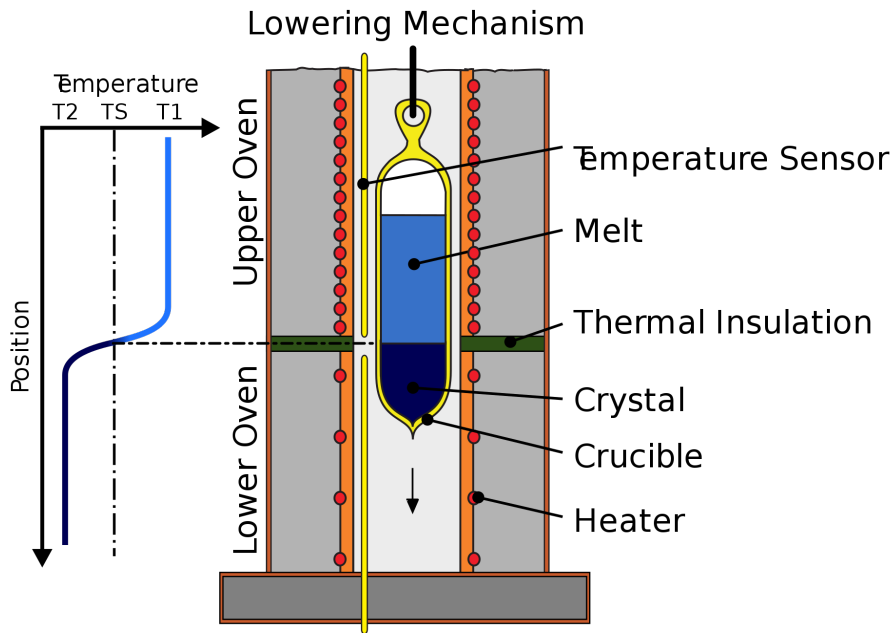


Figure 5.1: Schematic of a Bridgman-Stockbarger setup.

5.2 Single-crystal growth by Bridgman method

The single-crystal used in this study was grown by the Bridgman method. Named after Harvard physicist Percy Williams Bridgman and MIT physicist Donald C. Stockbarger, the Bridgman–Stockbarger method is a method of producing single-crystal ingots from polycrystals [225–227]. The method involves heating the polycrystals above its melting point followed by a slow cooling process from one end where a seed crystal is located. The process can be accomplished in both horizontal and vertical orientation. A schematic of the setup is shown in Fig. 5.1 below [source:wikipedia]:

Since the process of preparing the vacuum-sealed ampule used here is the same as the one described for the CVT growth, it has not been included here to avoid repetition.

Technical details of the experiment

- A tube that can snugly fit in the furnace should be selected for making the ampules.
- The ampules like should be made of materials like quartz that can withstand high temperatures. Glass is not preferred since they have a lower melting point (around 600°C) and a high coefficient of expansion. A high coefficient of expansion can

cause unsuitable pressure inside the ampule (too much pressure will stress the sample, too low pressure might not provide the sufficient condition to trigger the reaction).

- One end of the ampule should have a sharp pointy end. This will provide a stable ground for forming a single-crystal seed. In the sharp pointy end, misaligned (concerning the direction of the length of the ampule) grains get obstructed by the walls and die out. Ultimately the one that remains is a single-crystal seed in the tube-parallel direction.
- The ampule is hung freely while the furnace is moved upward to engulf the ampule.
- Then the temperature of it was set to 590°C. It was kept at this temperature for 4-5 hours. This is for the PdTe₂ polycrystalline ingot to melt and mix well and reach an equilibrium.
- After that, the furnace (not the hanging ampule) will be slowly moved upward at a rate of 1 mm/hour. It needs to move a total of 17 cm (170 mm). So, the total time this process would take is $170/24 = 7$ days.
- The setup that we used is the AEROTECH UNIDEX 511 (motion controller) and Omega CN7200 (temperature controller) (see Fig. 5.2).
- Something should be placed (like a bucket filled with cotton) exactly below the ampule so that in the event of a broken ampule, the melted compound does not spill on the floor.
- The ampule needs to be supported by a long straight quartz rod/tube so that the area of interest can be inserted well enough inside the furnace. This rod is supported by a thin wire (eg Ni-Cr) which at no point enters the furnace.

Outcome of the experiment

Single-crystal PdTe₂ of high quality were formed (see Fig. 5.3) as confirmed by XRD measurement (see Fig. 5.4).



OMEGA releases CN7200 1/4 DIN temperature controller

Figure 5.2: Motion controller and temperature controller for the Bridgman-Stockbarger growth.

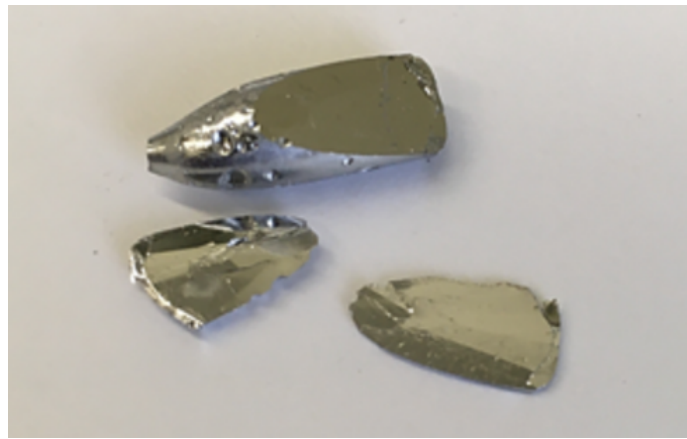


Figure 5.3: As-grown single crystal of PdTe₂

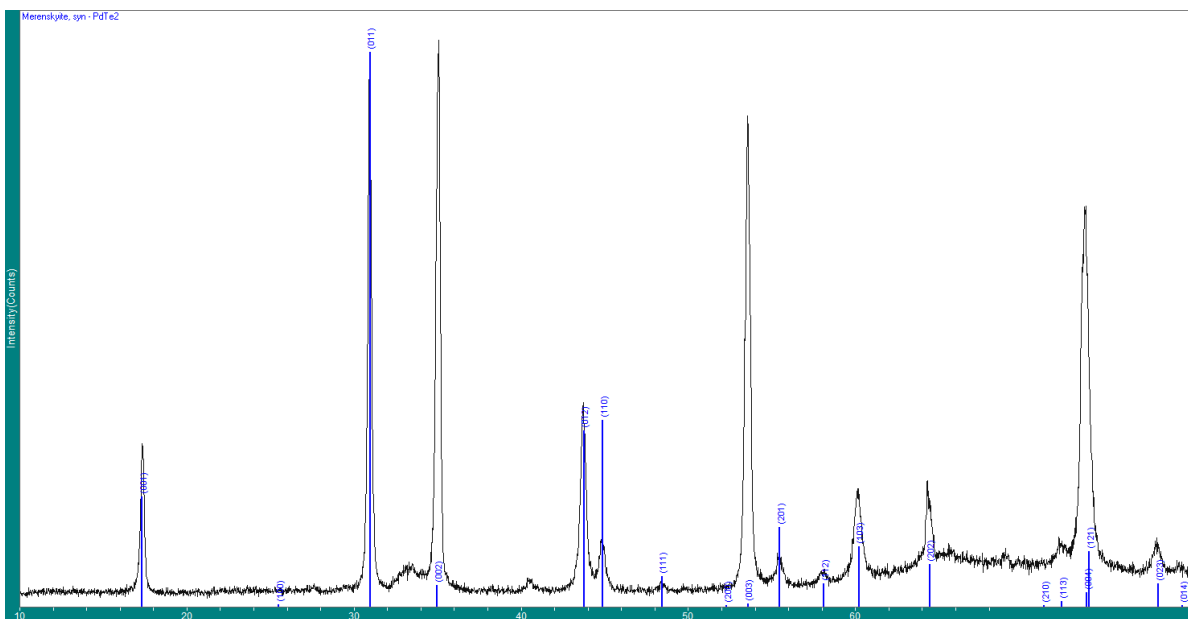


Figure 5.4: X-ray diffraction of the as-grown single crystal PdTe₂

If a sample can be prepared both by Bridgman and CVT, then Bridgman is preferable since it does not need any transport agent. Transport agents can incorporate with the sample and act as an impurity center. Also, Bridgman yields bigger crystals. CVT is used when the material to be prepared needs a high initial temp (e.g. 1500°C) to grow the material.

5.3 Results and discussion

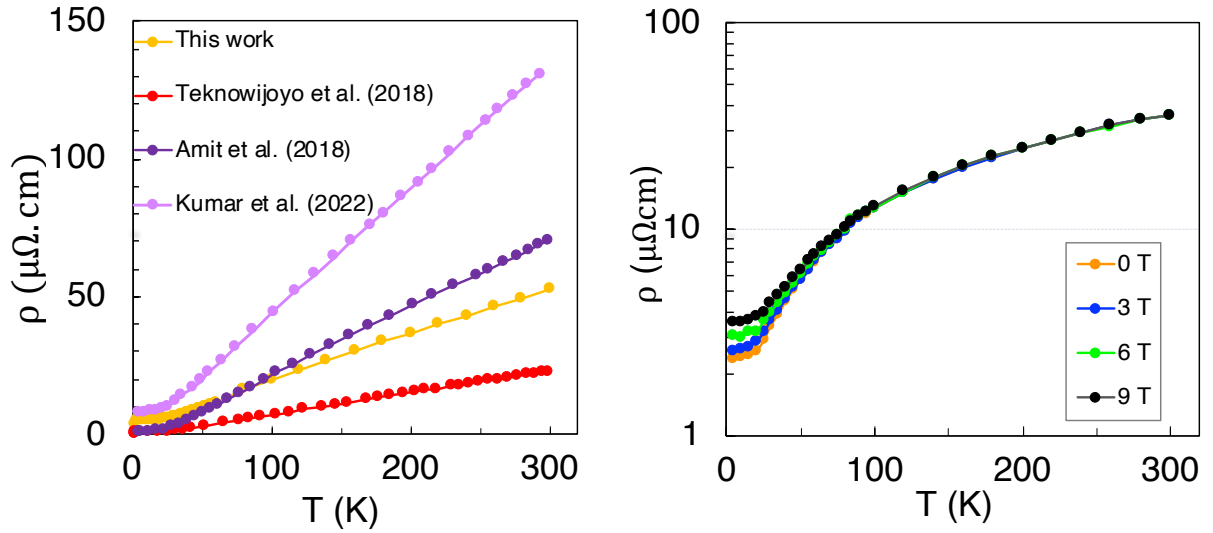


Figure 5.5: Temperature dependent variation of resistivity at (a) $B = 0$ T, and (b) varying magnetic field in PdTe_2

Temperature-dependent variation in the resistivity (ρ) of the sample under zero magnetic field is plotted in Fig. 5.5. With decreasing temperature, ρ decreases linearly, characteristic of conventional phonon scattering mechanisms commonly observed in metallic materials, and reaches a plateau at the lowest temperature as observed by others [228–230]. From Fig. 5.5 (b) we can see that ρ remains negligibly affected by the presence of magnetic field at high temperature (from 100 K and beyond). Maximum magnetic field-induced variation occurs at the lowest temperature ($T = 2$ K). This can be more clearly observed from the field-dependent MR% (defined as $[(\rho_B - \rho_0)/\rho_0] \times 100$) response illustrated in Fig. 5.6. Well-known topological semimetals show a strong correlation between mobility and magnetoresistance as investigated and confirmed by Singh et al.

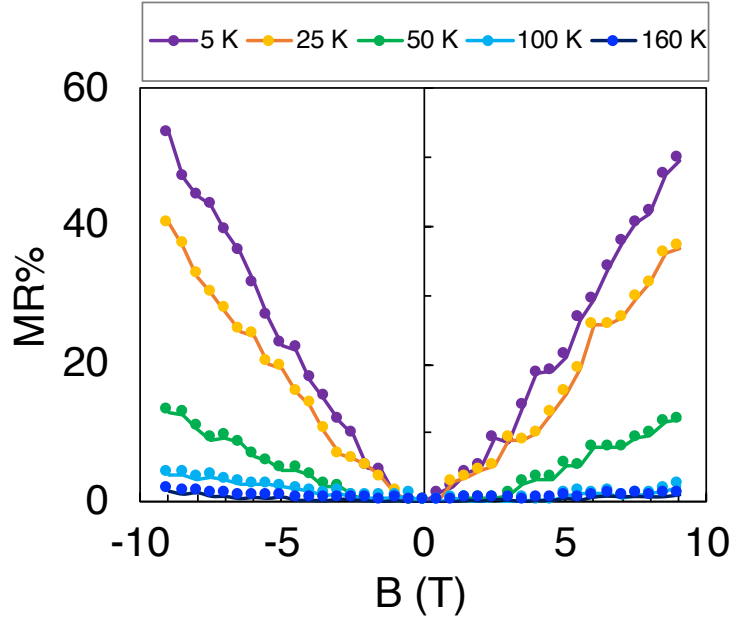


Figure 5.6: Magnetoresistance $[(\rho_B - \rho_0)/\rho_0] \times 100$ of PdTe₂ at varying temperature and magnetic field

[231]. When subjected to magnetic fields, increased mobile carriers undergo a more pronounced Lorentz force, leading to elevated magnetoresistance (MR). Since, PdTe₂ exhibits MR which is a few orders of magnitude smaller than other semimetals such as WTe₂ [232], Cd₃As₂ [233], TaP [166], etc., we can speculate that its carrier has much smaller mobility than these semimetals.

Temperature-dependent Seebeck coefficient measurement is plotted in Fig. 5.7 both in the presence and absence of a magnetic field. Throughout the measured temperature range, the magnitude of the Seebeck coefficient (S) remained below $5 \mu\text{V}\cdot\text{K}^{-1}$. This is consistent with the high degree of carrier compensation due to the semimetallic nature of the sample. Sign of S is positive from 75 K to higher temperatures. Considering this behavior and the magnitude of S we can speculate a slightly hole-dominated transport. At a temperature below 75 K, electrons start to dominate. Consequently, the sign of S turns negative. Application of magnetic field up to 3 T appears to negligibly affect the Seebeck coefficient from 50 K to 380 K. Owing to the reduced mobility as speculated from the magnetoresistance plot, a weak Nernst signal is generated (Fig. 5.8). N exhibits a nV/K signal that is linear concerning the magnetic field. This linear behavior is expected

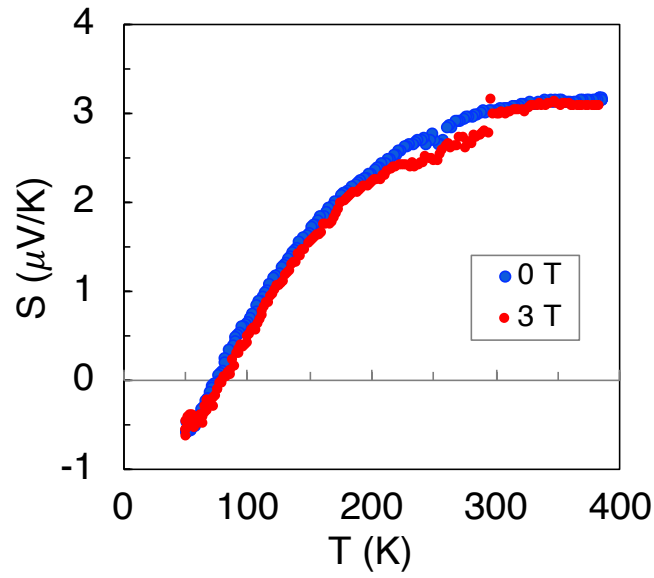


Figure 5.7: Seebeck coefficient (S) of PdTe_2 at varying temperature and magnetic field

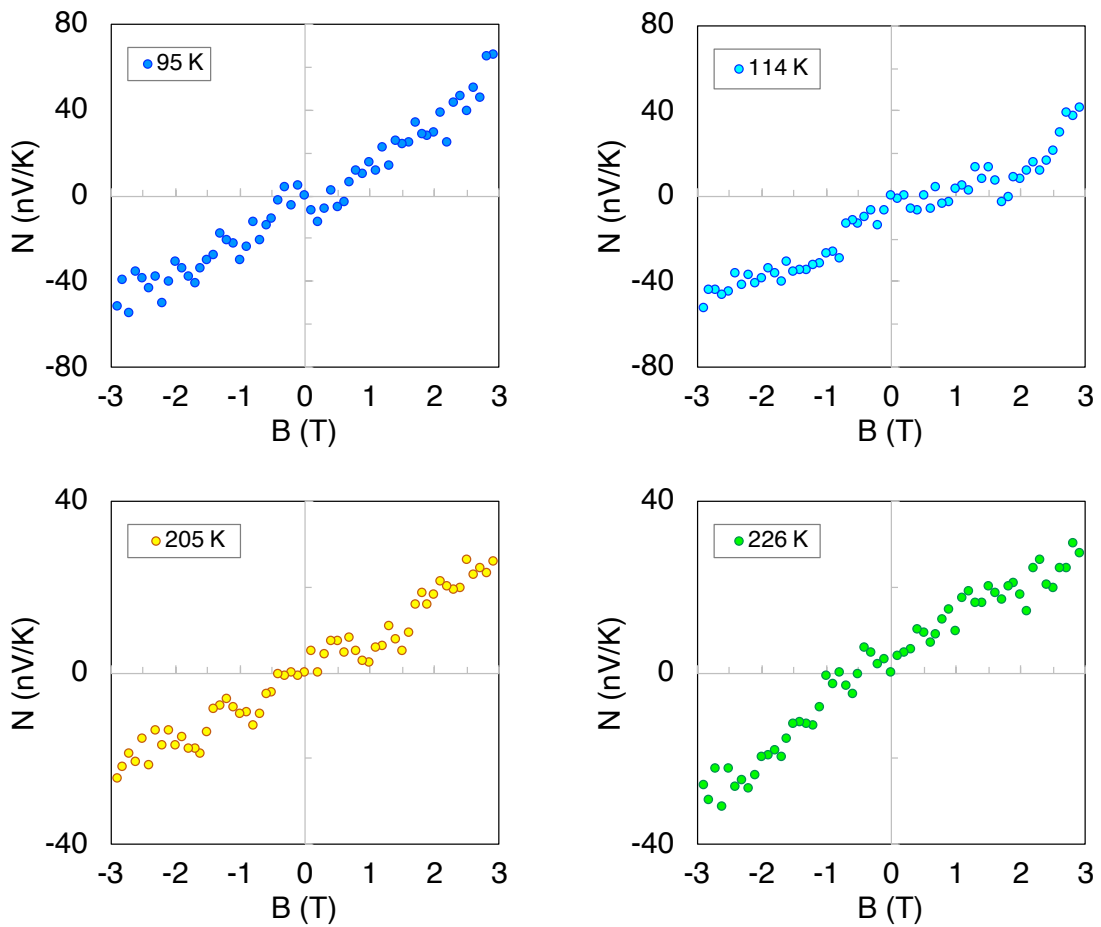


Figure 5.8: Nernst coefficient (S) of PdTe_2 at varying temperature and magnetic field

when $\mu B \ll 1$. This again aligns with the speculation that the mobility of electrons and holes in this sample is low. Over the temperature range that we measured N , we did not see any sharp enhancement in the magnitude of N due to the variation in sample temperature. This is probably due to the Fermi level being too far off than the extent to which temperature variation within 50 K to 385 K induces. Employing gating of the sample, a far greater shift of the Fermi level can be achieved, enabling the Dirac point crossing that can enhance the mobility and Nernst coefficient simultaneously.

5.4 Conclusion

In conclusion, our study on PdTe₂ provides insights into its thermomagnetic properties, highlighting its highly compensated carrier system and low carrier mobility. The Bridgman-grown single crystals offer a platform for further investigations, particularly with controlled gating to manipulate the Fermi level and potentially enhance both mobility and the Nernst coefficient. This work contributes to the growing body of knowledge on topological semimetals, laying the groundwork for future advancements in thermomagnetic device applications.

Chapter 6

Nernst response during the magneto-structural phase transition in FeRh

Collaborators and Personal Contributions: Equimolar FeRh thin-films and their structural characterization were performed by Dr. Steven P Bennett at the US Naval Research Laboratory. First-principle calculation was done by Sree Sourav Das under the supervision of Dr. Mona Zebarjadi (ECE, UVA). Nernst theory for the AF and FM phase was done by Dr. Mona Zebarjadi. Magnetization measurement was performed by Prof Sang-Kwon Lee's group at Chung-Ang University, Korea. The electrical, thermoelectric, and thermomagnetic characterizations were all done by Md Sabbir Akhanda under the supervision of Dr. Mona Zebarjadi (ECE, UVA).

6.1 Background and context

Phase change materials have a wide range of applications from sensors to information and energy storage and conversion. They are known for being capable of absorbing and releasing a large amount of thermal energy during their phase transition. Phase transitions have already been utilized for thermal storage and heat management in buildings, batteries, and energy conversion technologies such as solar thermal, geothermal, ocean thermal, thermoelectric, and magnetocaloric. Often a solid-solid phase transition is accompanied by electronic band structure, lattice geometry changes, and an increase in

entropy. In turn these result in changes in physical properties that can be utilized for device design. Of particular importance is the magneto-structural transition which is characterized by a simultaneous magnetic and structural phase change resulting from a strong coupling between the magnetic spin of a system's electrons and the atoms of its crystal lattice. External perturbations, such as variations in temperature, magnetic field, and strain, act as driving forces and influencing factors for these transitions. First-order magneto-structural phase transition has been observed in several systems and is associated with multi-functionalities of these systems. Variety of unusually powerful magneto-responsive properties such as colossal magnetoresistance [234], giant magnetocaloric effect [235–237], and giant magnetostriction [238] have been reported in this class of materials, prompting the idea of using these transitions for heat-assisted magnetic recording (HAMR) devices [239], sensors, and magnetocaloric microsystems [240].

The binary alloy FeRh with a CsCl-type (B2) intermetallic structure is one of the materials wherein a magneto-structural phase transition has been observed. This material is of particular relevance to semiconducting industry applications due to its near equimolar compositional simplicity and the appearance of its phase transition in the vicinity of room temperatures. The phase transition in FeRh was first observed back in 1938 [241]. Upon heating, the material transitions from the AF phase, also known as the α'' -phase, to the FM phase, also known as the α' -phase, with a subsequent 0.3% linear increase of the lattice constants in all directions preserving its original CsCl structure [242]. Many studies have been conducted to elucidate the fundamental aspects underlying this FeRh transition. Electronic disparities in the density of states (DOS) at the Fermi level of the two phases, backed by a significant increase of the Hall coefficient and a decline in electron carrier concentration in the AF phase can play a pivotal role in driving this transition. Hard x-ray photoemission study also reveals distinct differences between the antiferromagnetic (AF) and ferromagnetic (FM) states throughout the entire valence-band spectrum, elucidated by density functional theory [243, 244]. Recent hypotheses propose that the phase transition in FeRh may be driven by the competing magnetic states of the Rh atom which determine the magnetic state of the system [245, 246]. Gu and Antropov assessing the free energy change of AF and FM states in FeRh utilizing first-principles calculations (the non-collinear version of the linear muffin-tin orbital method)

concluded that the AF–FM transition in FeRh primarily stems from magnon (spin wave) excitation [247]. In a different approach, Barker and Chantrell leveraged atomistic spin dynamics to demonstrate that the first-order FeRh phase transition may result from the competition between bilinear and higher-order four-spin exchange terms in the effective spin Hamiltonian [248]. Variational effect of many external factors such as composition, magnetic field, thickness variation, doping, etc. on manipulating the transition has also been studied extensively [242, 249–253]. For instance, it has been found that minimal compositional variation ($0.48 \leq x < 0.54$ for $\text{Fe}_{1-x}\text{Rh}_x$) is possible without compromising the integrity of the phase transition altogether. Introducing various dopants such as Ni, Au, Cu, Pt, and Pd, the phase transition temperature has successfully been shifted both toward a higher or lower temperature [254–257]. Applying a tensile or compressive strain has also been found to shift the phase transition to a lower or higher temperature respectively [258].

Despite the prolonged investigation of this material thus far, only a handful of studies have been conducted to study its potential in thermal-to-electrical energy conversion using the three thermoelectric phenomena: the Seebeck effect, the Thomson effect, and the Nernst effect. The Seebeck effect involves the generation of a longitudinal voltage (ΔV) along the direction of a temperature gradient (ΔT) and is the basis of conventional thermoelectric devices. In the Thomson effect, heat is absorbed or produced when current flows in a material with a temperature gradient. In the Nernst effect, a transverse voltage (ΔV) is developed in response to a perpendicularly applied temperature gradient and magnetic field. Studying the hall coefficient, heat capacity, and Seebeck coefficient in bulk FeRh during the phase transition Kobayashi et al. reported a significant reconstruction of the Fermi-surface accompanying the phase transition [259]. Reporting a giant Thomson coefficient in Ni-doped bulk FeRh, Modak et al. observed a giant Thomson effect in FeRh which can result in significant Thomson cooling that easily offsets the Joule heating [158]. Yamauchi et al. studied the compositional dependence of the Nernst effect in FeRh/SiO₂ films at room temperature and reported an enhancement when Rh is 48% [260]. Using anomalous Nernst microscopy, Gray et al. [261] reported a positive Nernst response in Pt/FeRh/MgO films while using a conventional probe setup. Saglam et al. [262] observed a sign change of the Nernst coefficient in FeRh/MgO film around the

phase transition. A theoretical explanation of this temperature-dependent sign change in N of FeRh is still missing.

In this study, we experimentally and theoretically investigate the influence of substrate and film quality on the magneto-thermoelectric properties, namely the Seebeck coefficient (S) and the Thomson coefficient (τ), in near-equimolar FeRh thin films. In particular, we discuss the effect of substrate-induced stress in the film using first-principle calculations to explain the substrate-dependent sign change of the Seebeck coefficient in the AF phase and its heightened response in the FM phase. Additionally, using experimental data and an isotropic single band model that accounts for the anisotropic mobility of spin-up and spin-down electrons in the AF phase, we offer an explanation for the negative sign of N of FeRh/Al₂O₃ in the AF phase.

6.2 Materials and methods

6.2.1 Sample preparation

For all three FeRh films (FeRh/Al₂O₃, FeRh/SiO₂, and FeRh/MgO) used in this study, magnetron sputtering was chosen as the growth method. While choosing the substrates, special consideration was given to the substrates featuring a lattice closely aligned with the L1₀ phase (a crystallographic derivative structure of the FCC structure) of FeRh). The rationale behind these choices lies in the crucial role they play in the manifestation of a magneto-structural transition within FeRh. If not grown with high enough crystalline quality FeRh will not display a magneto-structural transition due to its high dependence on defect concentration in the lattice [263–268]. During sample growth, an AJA International Orion II magnetron sputter system was employed with a 4-inch inconel, backlight bulb heated substrate holder raised to 630°C substrate temperature. Before sample growth, the substrates were cleaned of organic contaminants in 10 mTorr Ar by a 10 W RF backscatter. Growths were conducted from a stoichiometric FeRh sintered 2-inch target, mounted on a 2-inch magnetron configured for magnetic targets, gradually raised to a DC power of 75 W in an Ar working gas pressure of 4 mTorr. Films were grown to a thickness of 20, 35, and 80 nm respectively verified by X-ray Fluorescence (XRF) [see Fig. 6.1] and X-ray reflectivity (XRR) [see Fig. 6.2] then analyzed using a fast

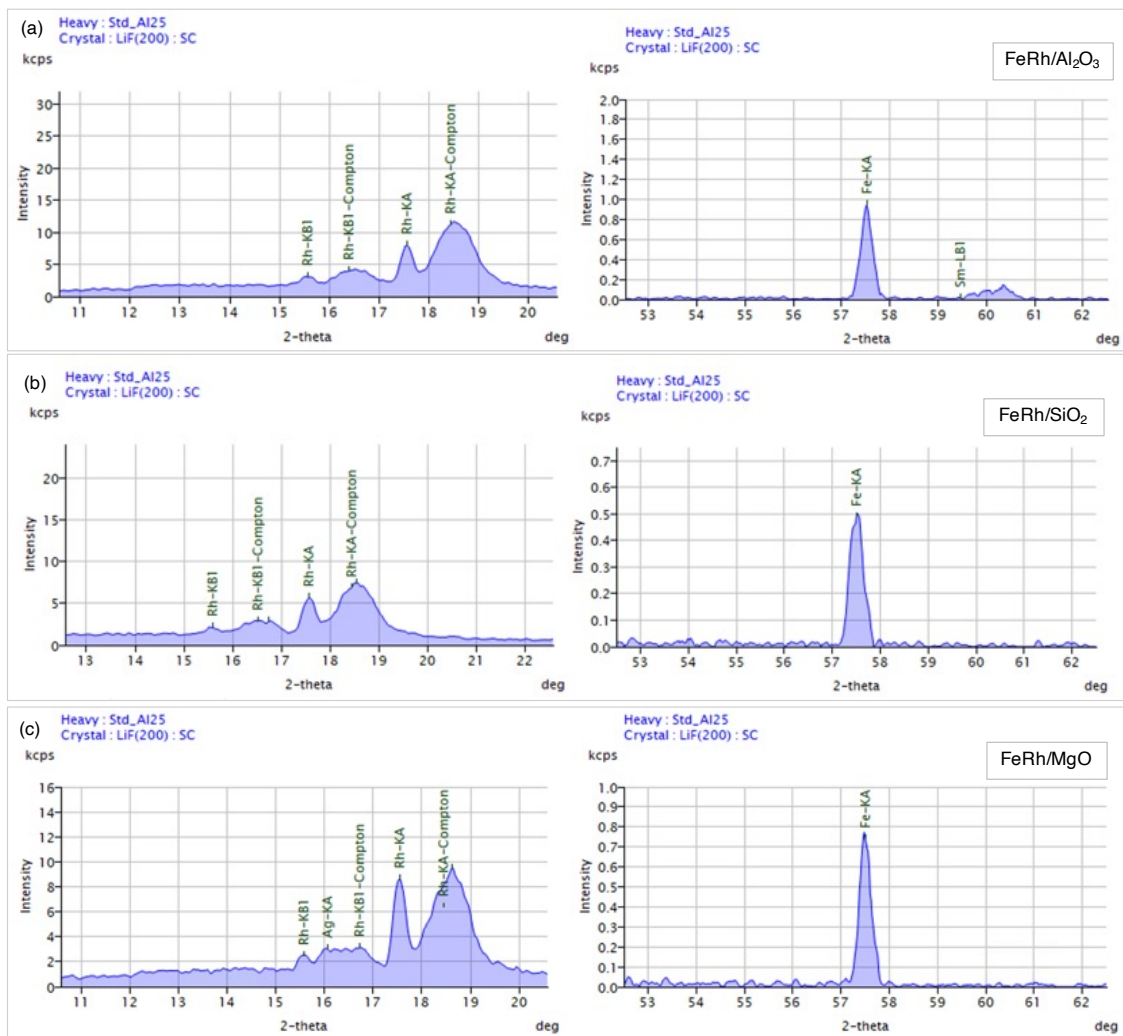


Figure 6.1: X-ray fluorescence study of FeRh/Al₂O₃, FeRh/SiO₂ and FeRh/MgO revealing Fe:Rh Mass% of 38:62, 37:63 and 37.5:62.5 respectively.

Fourier transform. After the growth, the films were annealed at an elevated temperature of 730°C for 1 hour in a high vacuum (4×10^{-8} Torr).

6.2.2 Transport property measurements

The temperature-dependent Seebeck coefficient measurement was conducted within the thermal transport option of a Versalab setup from Quantum Design Inc., utilizing the one-heater two-thermometer configuration. For making the electrical contacts, 0.5 mm wide gold-coated flat copper wires were used. One end of the sample was connected to a resistive heater, while the other end was clamped to the cold foot of the puck, serving as the heat sink. Between the heater and heat sink, two thermal transport shoes, capable of measuring both temperature and voltage, were placed to measure the temperature gradient and the corresponding voltage developed. To measure the resistivity of the samples, a four-point probe configuration was employed, passing current from the heater side towards the cold foot or the heat sink. In the Nernst measurement, an external magnetic field was applied perpendicular to the thermal gradient to generate a transverse voltage. The developed voltage was measured using a Keithley nanovoltmeter. To facilitate the measurement, the voltage lead of the cold side shoe was separated and connected transversely opposite to the hot side shoe along the width of the samples. Estimated errors in the Seebeck, resistivity, and Nernst measurements are approximately 5%, 3%, and 10%, respectively. Major sources of error include fitting errors in the MultiVu software (for Seebeck measurement), errors in measuring the sample size, and inherent instrumental errors.

6.2.3 Computational Methods

The spin-polarized first principle calculations of the density of states were performed using density functional theory (DFT) as implemented in VASP code [269–271] with Projected Augmented Wave (PAW) potentials [272]. We utilized the experimental lattice constant without structural relaxation to elucidate the observed experimental behavior. It is well-established that the choice of functionals in DFT can significantly influence the electronic properties of the system. Therefore, before performing the transport analysis, we investigated the stability of the phases using various functionals. This analysis

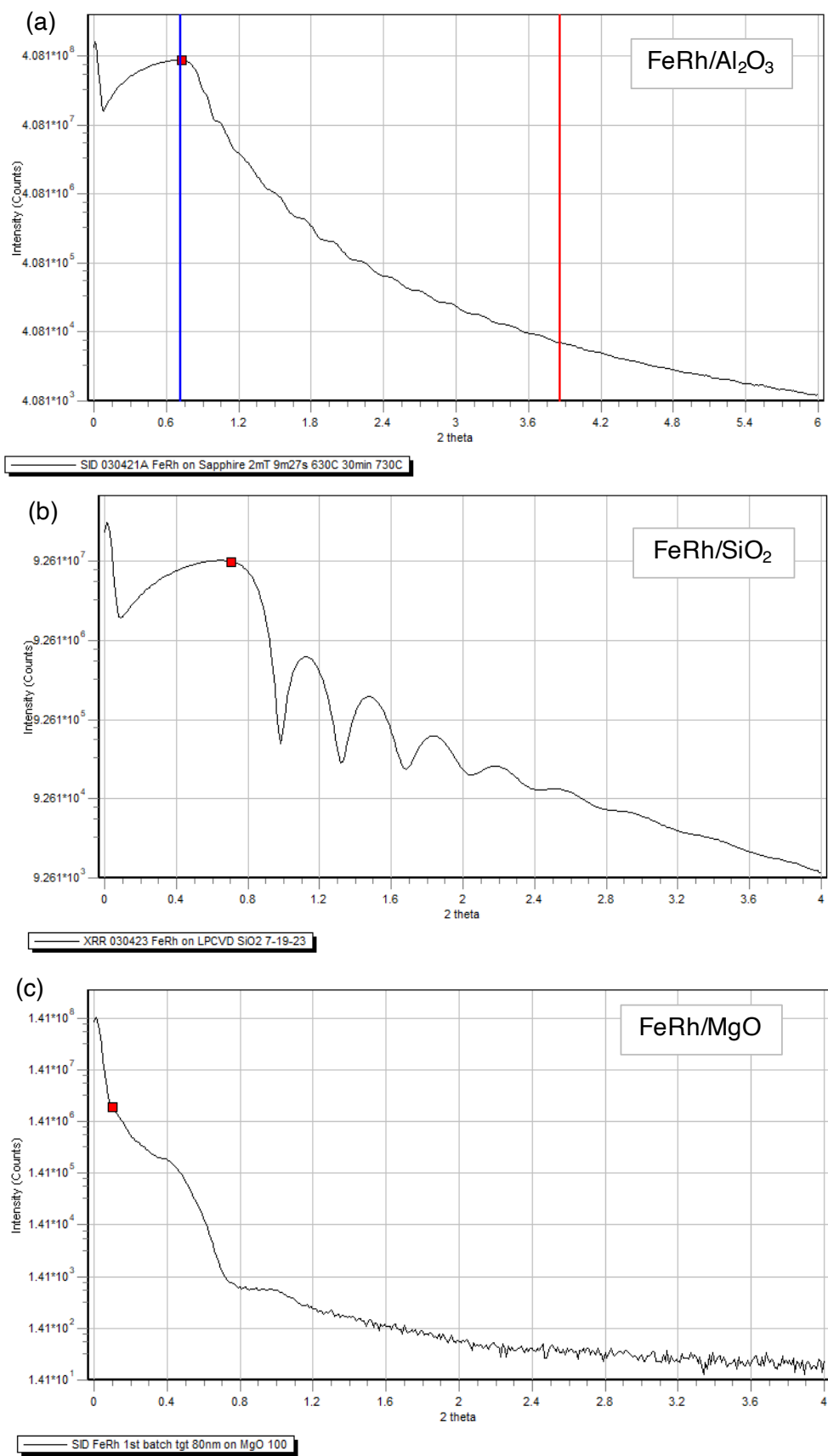


Figure 6.2: X-ray reflectivity data for FeRh/Al₂O₃, FeRh/SiO₂ and FeRh/MgO with FeRh film thickness of 35, 20 and 80 nm respectively.

guided us to focus on a specific functional that yielded stable structures and enabled us to accurately interpret the experimental results. The summary of the obtained local moment for Fe and Rh atoms along with external pressures for different functionals is listed in Table 1. Among these functionals, Perdew Burke and Ernzerhof (PBE) [273] functional demonstrates better results in terms of both local moment and stability compared to findings reported in the other calculations[274–277] in both phases. Additionally, we also applied Hubbard Correction methods[278, 279] by ($U+J$: $U_{\text{Fe}} = 2.0$, $J_{\text{Fe}} = 1.0$, $U_{\text{Rh}} = 1.5$, $J_{\text{Rh}} = 1.0$) parameters to match the calculated local moments with the experimental observations[280, 281]. However, it make the system unstable as indicated by external pressure.

The spin-orbit coupling (SOC) was also considered to complete the study but the density of states (DOS) revealed that the effect of SOC is negligible. Similar results were also reported by other studies [274, 282]. Therefore, SOC effects were not considered for further calculations. For electronic structure calculations, we used a $2 \times 2 \times 2$ supercell comprised of 16 atoms to simulate the AF and FM phases of FeRh. According to PAW pseudopotentials, Fe(3d, 4s) and Rh (4p, 5s, and 4d) orbitals were treated as valance states in this analysis. The plane-wave energy cutoff of 720 eV, which is more than 2.5 times the standard value, was chosen with a self-consistency threshold of 10^{-9} eV. A dense Monkhorst-Pack k-mesh grid of $17 \times 17 \times 17$ was used for sampling the Brillouin zone. As FeRh is metallic in nature, a smearing value of 0.05 eV according to the Methfessel-Paxton scheme was used for self-consistent as well as DOS calculations. The lattice parameters for AF and FM phases were fixed to experimental values $a=2.99$ Å[280] and $a= 3.01$ Å[281], respectively. With these parameters, the magnetic moments obtained from DFT calculations are $\mu_{\text{Fe}}=3.21$ and $\mu_{\text{Rh}}=1.05$ in the FM phase, and $\mu_{\text{Fe}}=3.12$ and $\mu_{\text{Rh}}=0$ in the AF phase. These values are in good agreement with other calculations [274–277] and experimental [283, 284] results. The total energy per atom for the AF phase is 0.02 eV lower than the FM phase at T=0 K.

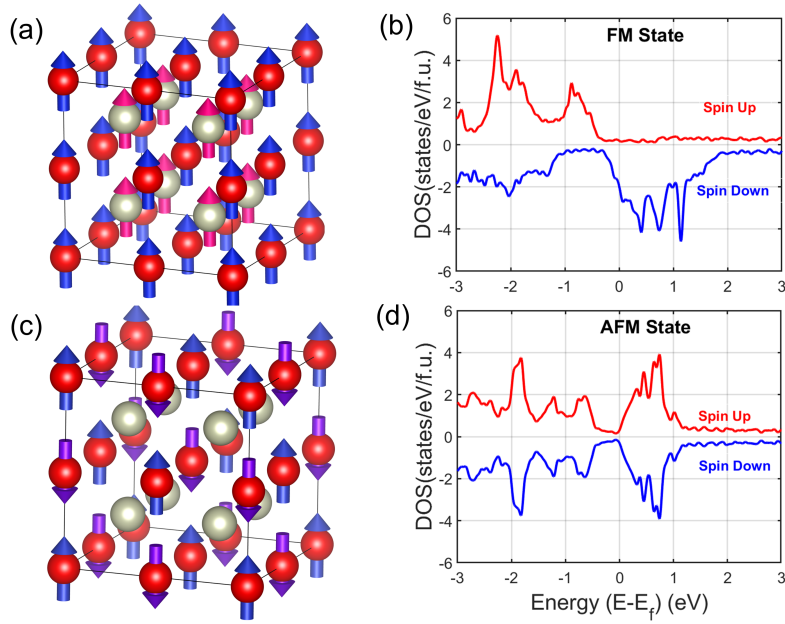


Figure 6.3: Chemically-ordered phase with B2 (CsCl)-type crystal structure [space group 221 ($Pm\bar{3}m$)] illustrating magnetic configuration and density of states of the FM (a-b) & AF (c-d) phase, respectively. Iron and Rhodium atoms are shown in red and silver respectively.

6.3 Results and discussion

6.3.1 Magneto-thermoelectric properties of the FeRh/Al₂O₃ thin film

The crystal structure of the AF and the FM phases along with their corresponding DOS per formula unit (f.u.) are shown in Fig. 6.3(a-d). The spin-polarized DOS for the FM phase was compared using different functionals (see Fig. 6.4) which shows a good consistency with the PBE results, particularly near the Fermi level. Both spin-up and spin-down electrons exhibit similar DOS contributions to transport in the AF phase as shown in Fig. 6.3(d). The influence of different functionals on DOS is also shown in Fig. 6.5 and total DOS varies significantly from 0.35 states/eV/f.u. to 0.8 states/eV/f.u. at Fermi level depending on the functionals. Considering the DOS for both crystal structures, the FM phase has a larger DOS at the Fermi level corresponding to larger carrier density, and has the dominant contribution from spin-down electrons. From PBE calculations, we found a significant rise in DOS from 0.8 states/eV/f.u. for the AF phase to 2.05 states/eV/f.u. for the FM phase. The effect of this rise in DOS is reflected in the

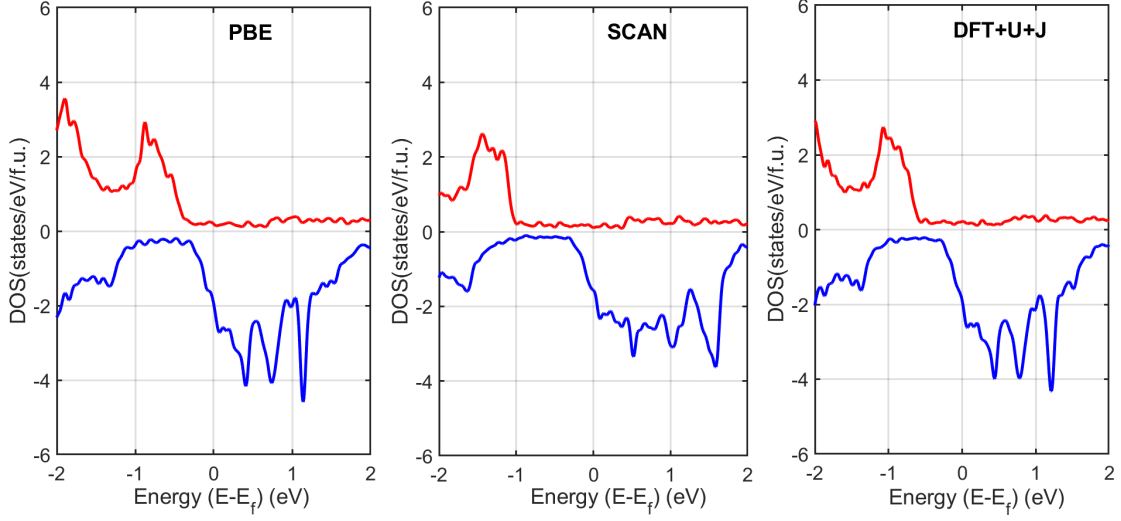


Figure 6.4: Density of States of FM phase of FeRh using PBE, SCAN, and DFT+U+J functionals.

transport parameters we experimentally measured.

Temperature-dependent variation in the resistivity (ρ) and $d\rho/dT$ of the FeRh/Al₂O₃ film is shown in Fig. 6.6(a-b). A hysteresis behavior accompanied by a steep drop in the resistivity due to the AF-FM phase transition appears during a temperature sweep up and down which can be attributed to the increased DOS in the FM phase as mentioned beforehand. The hysteresis spans from 170 K to 325 K under a zero magnetic field with the peaks in $d\rho/dT$ confirming different phase transition temperatures, T_c for the heating and cooling cases. To streamline our discussion, we adopt the notation T_{low} and T_{high} for these two (lower and upper) anchor points henceforth. After systematic 1 T increments of the magnetic field along the [001] direction starting from 0 T up to 3 T, both the T_{low} and T_{high} shift toward lower temperature. In a temperature sweep around the phase transition starting from low temperature and progressing slowly toward high temperature, the AF phase, characterized by adjacent magnetic moments aligned in opposite directions, can overcome the energy barrier to gradually align its magnetic moments parallel to each other to transition to the FM phase. The application of an external magnetic field accelerates this alignment process resulting in the whole hysteresis loop shifting towards lower temperatures [285]. T_{high} shifts in a linear fashion by approximately 5 K for every 1 T magnetic field increment. On the contrary, T_{low} follows a non-linear pattern

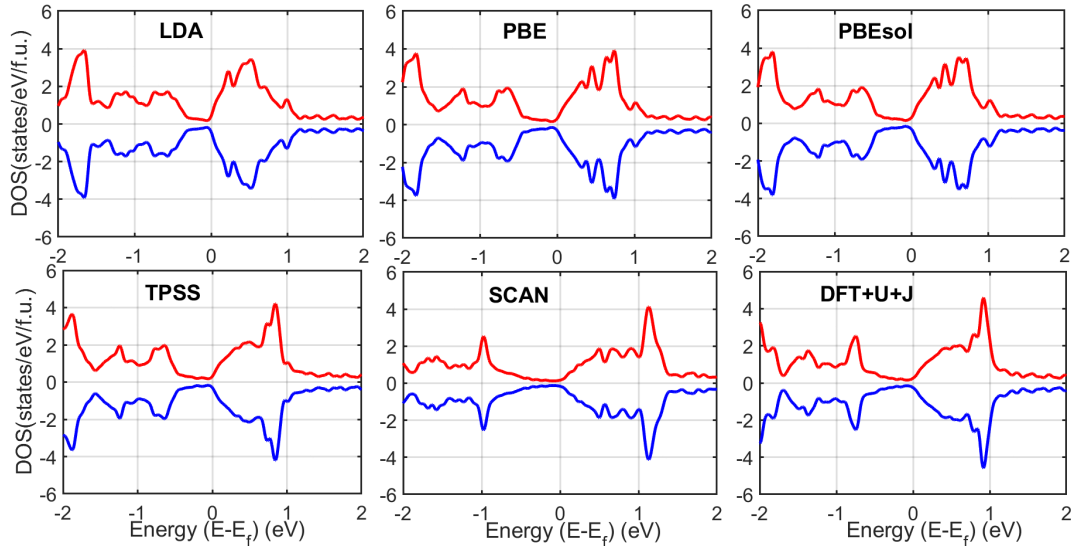


Figure 6.5: Density of States of AF phase of FeRh using LDA, GGA (PBE, PBEsol), MetaGGA (TPSS, SCAN), and DFT+U+J functionals

with approximately 5 K, 15 K, and 30 K shifts in T_{low} during the increments 0-1 T, 1-2 T, and 2-3 T, respectively. This unequal shift experienced by T_{low} and T_{high} results in the loops extending over a greater temperature range at higher fields.

Similar to electrical conductivity, the Seebeck coefficient is an electronic property that depends on the details of the band structure and scattering rates. During the phase transition, the magnetic and crystal structure of FeRh changes driven by the magnetic field and temperature changes. Associated with these, a change in the electronic band structure and phonon dispersion is also to be expected simultaneously. An increased DOS and its slope with respect to energy has been observed in the FM phase and is shown in Fig. 6.3(b). Consequently, the log of DOS is larger in the FM phase (see Fig. 6.7) resulting in a larger S in the FM phase according to the Mott formula [286]. To be precise, we observed S to be approximately six times larger in the FM phase compared to the AF phase (see Fig. 6.3(c)) which matches with the theoretical calculation. An alternative explanation for this enhancement stems from the increase in entropy during the transition. In metals, S is a measure of entropy per charge carrier. Therefore, the increase in S serves as evidence that the electronic entropy increases while transitioning to the FM phase. The total entropy change during this phase transition is measured experimentally to be in the range of 12 to 19 J.kg⁻¹.K⁻¹ [259, 287, 288]. The overall entropy change has elec-

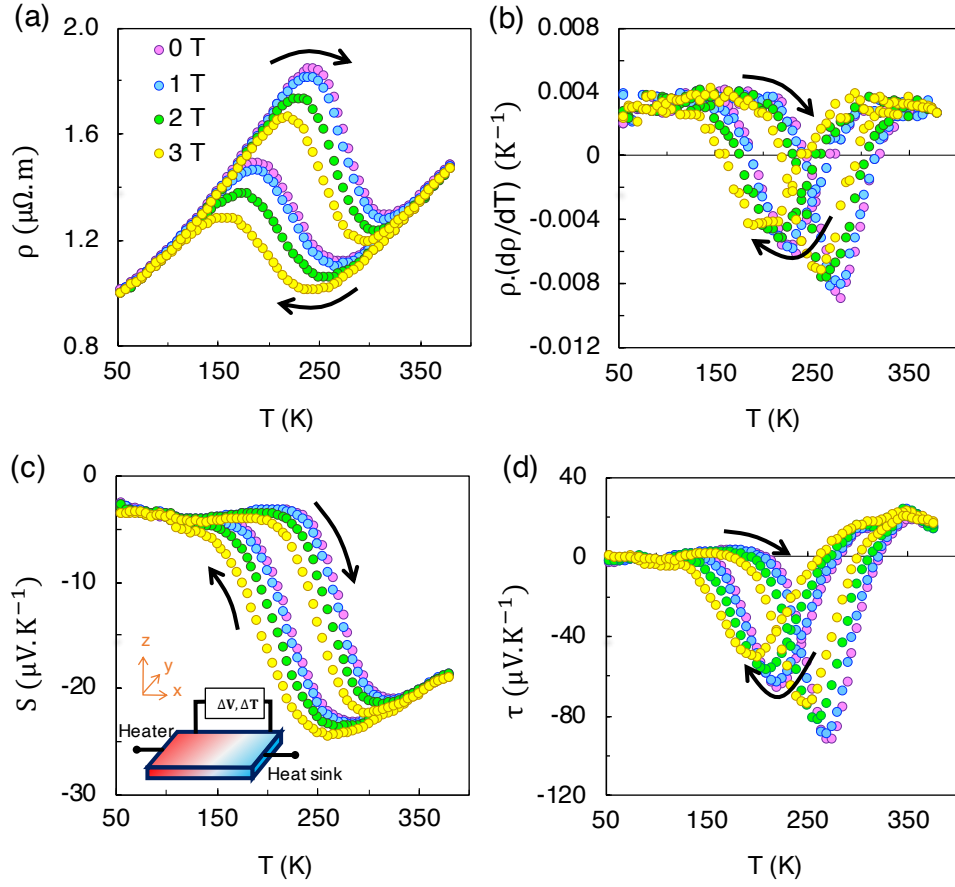


Figure 6.6: Temperature-dependent variations in the resistivity (ρ), $\rho \cdot d\rho/dT$, Seebeck coefficient (S), and Thomson coefficient ($\tau = T \cdot dS/dT$) of FeRh/Al₂O₃. The magnetic field dependence of the thermal hysteresis is shown by different colors as indicated in the legend of (a). The black arrows indicate temperature sweep in the upward and downward direction respectively around the phase transition. Inset of (c) is a schematic representation of the Seebeck coefficient measurement setup

tronic, lattice (phononic), and magnetic contributions. The phononic entropy increase is attributed to phonon softening in the FM phase [289]. Cook et al. were able to separate the contributions to the entropy using low-temperature specific heat, along with sound velocity and photoemission measurements. They reported an electronic entropy change of $8 \pm 1 \text{ J.kg}^{-1} \cdot \text{K}^{-1}$ [287]. An electronic entropy change of about $8.9 \text{ J.kg}^{-1} \cdot \text{K}^{-1}$ was reported by Perez et al. for the case of Ni-doped FeRh bulk polycrystalline sample corresponding to a ΔS of $\approx 40 \mu\text{V.K}^{-1}$ during the phase transition [288].

The T_{low} and T_{high} of the hysteresis loop captured by S are 85 K and 360 K respectively, a range which is comparatively broader than the one observed during the resis-

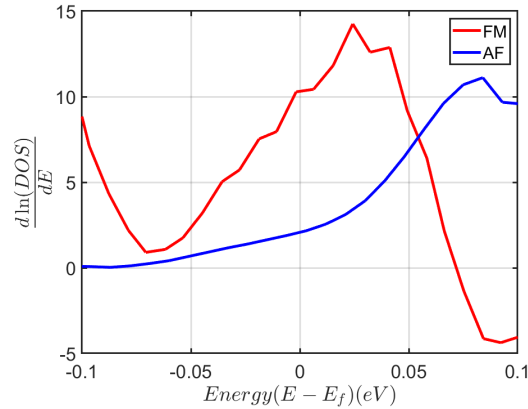


Figure 6.7: Derivative of $\ln(\text{DOS})$ for two phases according to Mott formula.

tivity measurement. The greater magnitude change and broader loop in S compared to ρ also highlights the Seebeck coefficient measurement's superior sensitivity in probing phase transitions wherein a minimal structural change is involved. A similar observation was made by Akhanda et al. while studying $1T'$ - MoTe_2 single crystal [159]. Resistivity changes are not strong since both AF and FM phases of FeRh are metallic. Experimental observation suggests a slight increase in resistivity that can be attributed to the shorter electron mean free path (MFP) in the FM phase [158, 288]. The Seebeck coefficient is not sensitive to the MFP but, it can effectively discern the relative changes in the entropy associated with the phase transition, making it more responsive to the underlying changes.

Though the magnitude of S we observed is much lower than that of conventional thermoelectric materials [35, 290, 291], a Thomson effect-based device designed around the abruptness of the temperature-dependent behavior can provide an alternate thermal-to-electrical energy conversion route. The Thomson effect manifests as a heating or cooling phenomenon when a current is passed through a material in the presence of a temperature gradient [292, 293]. Devices built based on this effect require only a single material type compared to the two types (n-leg and p-leg) needed in a Seebeck effect-based conventional thermoelectric device [294]. The Thomson coefficient (τ) can be expressed as the product of the material's average temperature (T) and the first derivative of S concerning T ($\tau = T \cdot dS/dT$). The Thomson figure of merit is a combination of the thermoelectric figure of merit and the Thomson to Seebeck coefficient ratio [160]. Consequently, the phase transition-induced sharp change in the S has fueled the exploration

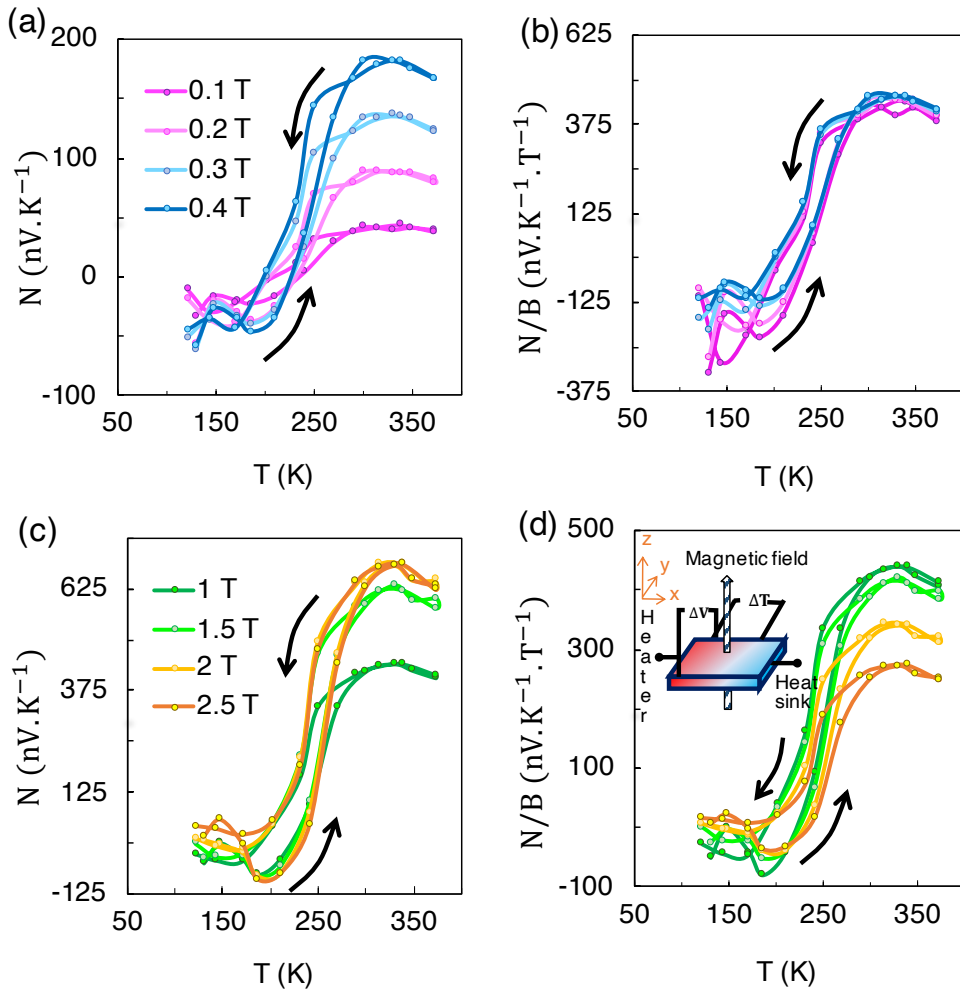


Figure 6.8: The temperature and magnetic field dependence of the Nernst thermopower (N) and the Nernst coefficient (N/B) of FeRh/Al₂O₃. The legends in (b) and (d) align with those in (a) and (c), respectively. The black arrows indicate temperature sweeping up and down around the phase transition. The inset of (d) depicts the Nernst coefficient measurement setup.

of Thomson effect-based devices using FeRh in recent years. This was highlighted in bulk FeRh recently, where a very large τ is reported over an extremely narrow temperature range [158]. The temperature-dependent τ of FeRh/Al₂O₃ is graphically depicted in (see Fig. 6.6(d)). The heating and cooling temperature sweep reveals distinct peaks, a consequence of the hysteresis observed in the Seebeck behavior. Compared to the temperature-dependent Seebeck coefficient behavior which exhibited a peak of 21 $\mu\text{V.K}^{-1}$ in the heating and 23 $\mu\text{V.K}^{-1}$ in the cooling sweep, the Thomson coefficient demonstrates magnitudes of approximately 98 $\mu\text{V.K}^{-1}$ and 66 $\mu\text{V.K}^{-1}$ respectively. The

values reported here for thin film are an order of magnitude smaller than those reported for bulk FeRh[158]. However, the phase transition range is much larger compared to bulk samples, and the Thomson coefficient is nonzero in the 150-350 K temperature range, which is more appropriate for device applications [160].

Next, we study the Nernst thermopower (N) and Nernst coefficient (N/B), the T -dependent response of which is plotted in Fig. 6.8(a-d). We observe a narrower but similarly shaped thermal hysteresis like that in S . The absolute value of N/B is larger in the FM phase (high-temperature phase), which is counter-intuitive since the Nernst coefficient tends to be larger at lower temperatures and when the mobility is larger [35]. Furthermore, we observe that at a given temperature, N/B of the FM phase is constant and is magnetic field independent up to about 1 T. It decreases at larger magnetic fields, indicating higher-order terms are important and the Nernst voltage is no longer linear with respect to magnetic field. The Nernst coefficient is an order of magnitude smaller in these samples compared to the Seebeck coefficient. While this is a ferromagnetic material and it is expected that the anomalous Nernst coefficient has a significant contribution, we would highlight that the nonzero component of the Nernst coefficient at zero magnetic field is extremely small and negligible in both FM and AF phases [262]. As the magnetic field is applied perpendicular to the thin-film plane, even in the FM phase, the magnetization in the cross-plane direction is small at zero magnetic fields. Hence we can explain the behavior of the Nernst using traditional models but with a modified magnetic field. In the FM phase, spin-down is the dominant one as we demonstrated in Fig. 6.3(b). If we assume isotropic bands, we can obtain a simple model for the isothermal Nernst thermopower, N_T in a metal [89] -

$$N_T = S \left(\frac{r}{r + 1.5} \right) \mu_H B_z \quad (6.1)$$

where, S is the Seebeck coefficient, μ_H is the Hall coefficient, and a power law represents the energy (E) dependence of the relaxation times (τ), i.e. $\tau \propto E^r$. B_z is the internal magnetic field experienced by the electrons which is the sum of the external magnetic field and the internal magnetization. Magnetization for these samples is linear to the external field (up to 3T) and at 350 K and it roughly increases the internal field by a factor of 2.2 (see Fig. 6.9). Therefore, we can modify our equation to present the Nernst

coefficient as

$$N = N_T/B_{z(ext)} = 2S\left(\frac{r}{r+1.5}\right)\mu_H \quad (6.2)$$

Combining results from Perez et al. and Modak et al. and considering $\mu_H = 40 \text{ cm}^2/\text{V.s}$ [158, 288], $S = 25 \text{ } \mu\text{V}/\text{K}$ (measured value of Seebeck coefficient at 350 K from this work, see Fig. 6.6), and $r = -0.8$, we obtain $N = 228 \text{ nV}/\text{KT}$ which is close to the experimentally measured value in Fig. 6.8. The r value is obtained by fitting the FM DOS close to the Fermi level with power law and assuming relaxation times are inversely proportional to DOS.

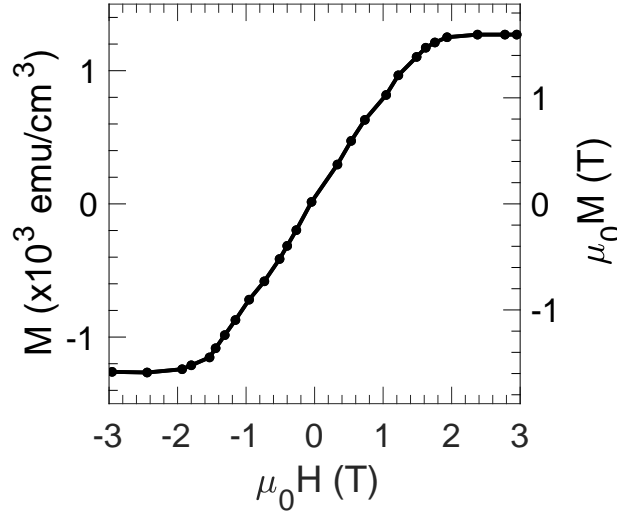


Figure 6.9: Temperature-dependent magnetization of FeRh/Al₂O₃ films in a magnetic field up to $\pm 3 \text{ T}$ at 350 K. The measurement was taken using a PPMS system with a vibrating sample magnetometer (VSM) (Quantum Design, Inc. USA).

The AF phase is more complex as there are two parallel currents of spin-up and spin-down contributing almost equally. The position of the Fermi level is not well established (see Fig. 6.5) as it is close to the minimum of the DOS and can move within the valley when there is a strain in the system, hence the DOS cannot be fitted at the Fermi level with a simple power law. In the mixed phase region, the presence of the ferromagnetic regions results in spin-dependent scattering rates and unequal mobilities for the two types of spins which then results in terms in the Nernst coefficient that have contributions from both bands (mixed terms) [89]. The sign of Nernst in this region then depends on the details of the mobility of spin-up and spin-down carriers and can be

obtained using:

$$N_T = \frac{\sigma_0^{\uparrow 2} N_0^{\uparrow} + \sigma_0^{\downarrow 2} N_0^{\downarrow}}{(\sigma_0^{\uparrow} + \sigma_0^{\downarrow})^2} + \frac{1}{T^2} \frac{\sigma_0^{\uparrow} \beta_0^{\downarrow} \mu_{\beta}^{\downarrow} - \sigma_0^{\downarrow} \beta_0^{\uparrow} \mu_{\beta}^{\downarrow} + \sigma_0^{\downarrow} \beta_0^{\uparrow} \mu_{\beta}^{\uparrow} - \sigma_0^{\uparrow} \beta_0^{\downarrow} \mu_{\beta}^{\uparrow}}{(\sigma_0^{\uparrow} + \sigma_0^{\downarrow})^2} B_z \quad (6.3)$$

Here N_0^{\uparrow} refers to the Nernst coefficient of spin-up carriers in the absence of spin-down carriers. Similarly, σ_0^{\uparrow} refers to the electrical conductivity of spin-up electrons in the absence of spin-down electrons. The same notation is used for spin-down Nernst and electrical conductivity. Hence, the first term is the weighted average of spin-up and spin-down Nernst coefficients. The second term is the mixed term and has the contribution of both spin up and down. μ_{β} is the thermal mobility, β_0 is the thermoelectric response function. These parameters are defined in ref [89].

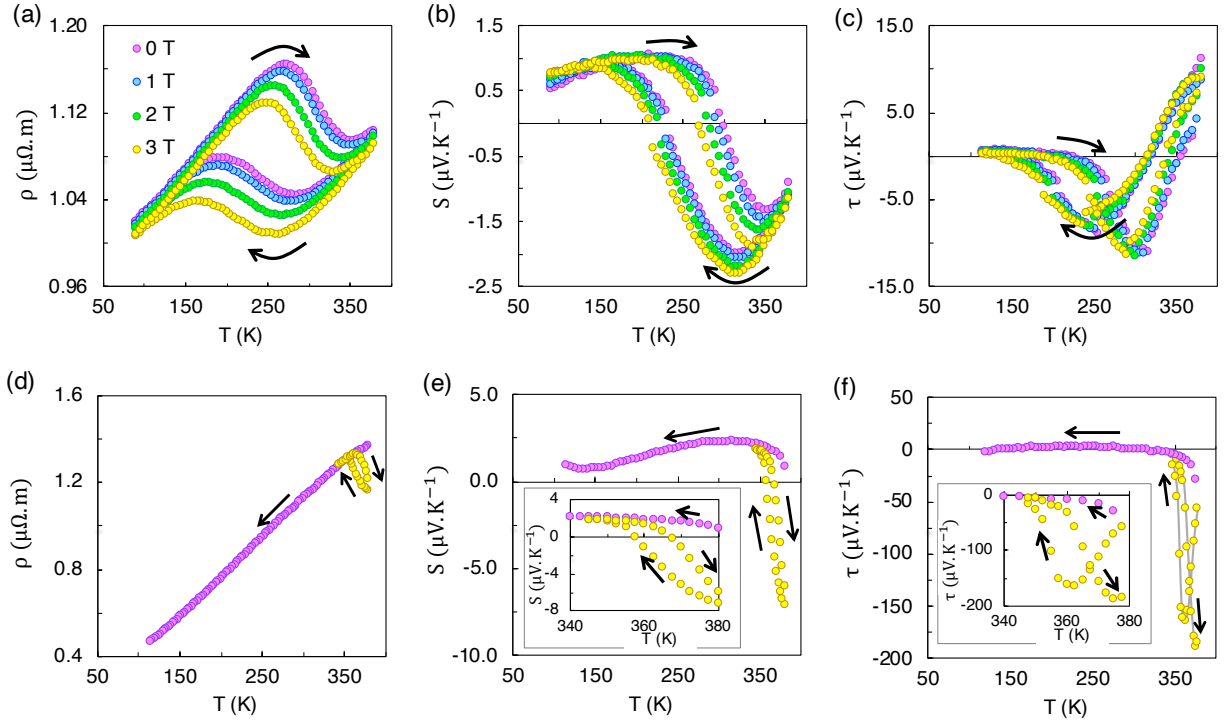


Figure 6.10: Variations in resistivity (ρ), Seebeck coefficient (S), and Thomson coefficient (τ) of FeRh/SiO₂ (a-c) and FeRh/MgO with changing temperature. The legends in Figures 3b and 3c align with those in Figure 3a whereas the legends in Figures 3e and 3f align with those in Figure 3d. The black arrows denote the temperature sweeping up and down around the phase transition.

6.3.2 Substrate dependence of the transport parameters

Temperature-dependent variation of the transport properties namely the resistivity, the Seebeck coefficient, and the Thomson coefficient, of FeRh/SiO₂ and FeRh/MgO are shown in Fig. 6.10(a-f). Comparing these two films, a major shift in the phase transition temperature (T_c) can be observed across [266]. FeRh/Al₂O₃ and FeRh/SiO₂ exhibit similar T_c . On the contrary, the phase transition of FeRh/MgO is largely shifted towards higher temperatures. Due to the limited high-temperature measurement capability of our experimental setup, we could only capture the onset of this transition. Different substrates induce different degrees of strain on the films which can have a significant effect on T_c . FeRh/Al₂O₃ films experience out-of-plane compressive strain and in-plane tensile strain [295]. Despite the similar unit cell volume of FeRh on both substrates, the different degrees of strain induced by the substrates lead to varying tetragonality ratios (c/a). FeRh/MgO exhibits $c/a > 1$, while for the case of FeRh/Al₂O₃, it is less than 1. These differences result in large shifts in T_c [296]. Kumar et al. observed a shift of over 60 K when in-plane stress is changed from compressive to tensile types [297]. In addition to a shift in the T_c , we also observe a change in the degree of abruptness in the transition. Specifically, we observe a slower transition in the case of all three films when compared to bulk FeRh [158]. Among the three films, FeRh/SiO₂ exhibits the broadest while FeRh/MgO exhibits the sharpest transition. This broadening of the overall transition compared to bulk has been ascribed to be a defect-driven phenomenon as argued by Keavney et al. [298]. While examining the average lattice expansion's evolution using spatially resolved diffraction across FeRh film during the phase transition, they found a heterogeneous mix of AF and FM phases. AF and FM phases appear as nucleated islands in the films with new ones forming and joining larger islands at higher or lower temperatures depending on the heating/cooling nature of the temperature sweep. A region of the film around a defect experiences a lower/higher effective transition temperature due to the localized strain or electronic structure change, leading to a distribution of nucleation temperatures across the sample and consequently resulting in a slower transition. So, a film with fewer defects should experience a steeper transition. Comparing the abruptness in the three films, a lesser degree of defect sites in the case of FeRh/MgO can thus be predicted compared to the other two films. If we compare the resistivity

of the three films at around 50 K - 100 K where all three samples are in the AF phase, FeRh/MgO exhibits the smallest resistivity supporting this hypothesis. In fact, FeRh has a minimal lattice mismatch of 0.3% to the FCC cubic lattice of MgO ($a = 4.212 \text{ \AA}$) and a relative 45° in-plane rotation demonstrating excellent epitaxial matching whereas for FeRh(111) films on $\text{Al}_2\text{O}_3(0001)$, a substantial lattice mismatch of -11.3% is observed [299]. Consequently, the transition in FeRh/MgO happens in a relatively shorter temperature range accompanied by the sharpest change in S and the most heightened Thomson peak among the three films. For the part of the phase transition that we could capture, a τ peak of $188 \mu\text{V.K}^{-1}$ in the heating and $163 \mu\text{V.K}^{-1}$ in the cooling temperature sweep was observed.

In the FM phase, the Fermi level is deep in the band and the slope of DOS is positive at the Fermi level (see Fig. 6.3) resulting in an electron-like behavior and a negative Seebeck coefficient for all three films. Consequently, bulk [158] as well as thin-films (this work) always demonstrate a negative Seebeck coefficient in this phase. In the case of AF, however, the Fermi level is very close to a minimum in the DOS as shown in Fig. 6.3. The position of the Fermi level in this case can change toward positive or negative slopes through doping and strain. Bulk FeRh has shown an almost zero Seebeck coefficient [158] whereas a Ni-doped FeRh demonstrates a positive Seebeck coefficient. Our measurement reveals that the use of SiO_2 or MgO as the substrate can also result in a positive sign of S in the AF phase. This change can be attributed to the magnitude and type of strain (tensile or compressive) at the film/substrate interface due to a mismatch of the lattice parameters. An in-plane tensile strain of -0.27% is reported in FeRh films on Al_2O_3 while an in-plane compressive strain of $+0.33\%$ was reported for FeRh/MgO(100) [300]. To demonstrate this, first principle calculations were performed, considering the impact of different levels of tensile and compressive stress in the lattice parameters. As shown in Fig. 6.11, tensile vs compressive strain can move the Fermi level toward more positive or more negative slopes or flat regions in the DOS. Applying a tensile strain of 4% in the in-plane direction leads to a positive slope of the DOS, resulting in a negative Seebeck coefficient. Conversely, subjecting the material to a 4% percent compressive stress in the in-plane direction a gradual movement of the DOS slope towards zero and followed by a negative value can be induced. Therefore, while

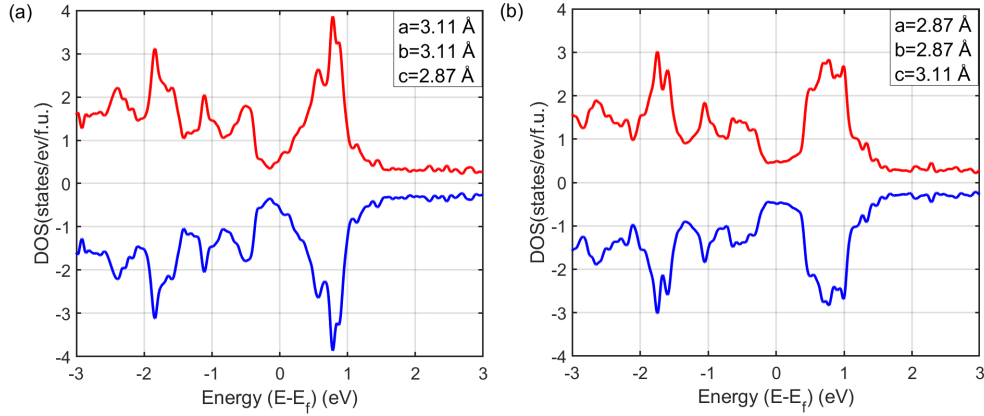


Figure 6.11: Effects of tensile and compressive strain on the DOS of AF phase of FeRh. 4% tensile and compressive strain was applied along in-plane and out-of-plane simultaneously and vice-versa. The degree of strain along with the lattice parameter is also given.

the sign of the Seebeck coefficient remains always negative in the FM phase, it can be zero, negative, or positive in the AF phase depending on the film/substrate combination and its induced strain strength and type.

6.4 Conclusion

We have investigated the magneto-thermoelectric properties encompassing the Seebeck coefficient (S), and the Thomson coefficient (τ) in near equimolar FeRh thin films grown on three different substrates namely, Al_2O_3 (sapphire), SiO_2 , and MgO . The phase transition temperature range and the transport responses are affected by the substrate. We showed that the value of τ depends on the quality of the films and the type of substrate. Due to a difference in the epitaxial growth strains and lattice mismatch values in the film/substrate interface, FeRh/ MgO exhibits the most prominent peak Thomson response. This response is not only closer to bulk values but is also approximately twice as high as that observed in FeRh/ Al_2O_3 and twenty times higher compared to that in FeRh/ SiO_2 . The Seebeck coefficient exhibited different signs in the AF phase, depending on the substrate. Our first principle calculation suggests it to be a consequence of substrate-induced strain variation in the film. Consistent with previous reports, the

phase transition temperature, T_c is lower for FeRh/Al₂O₃ compared to FeRh/MgO and further shifts to a lower temperature with a magnetic field. Additionally, we reported Nernst thermopower (N) in FeRh/Al₂O₃, which is two orders of magnitude smaller than S and changes its sign during the transition. The differing signs in the two phases were explained using an isotropic single-band model, considering an anisotropic mobility of spin-up and spin-down electrons in the AF phase. Despite the AF phase displaying higher mobility, the magnitude of N was higher in the FM phase owing to the contribution from its internal magnetization. A hysteresis loop was evident in the temperature-dependent N response with a shape similar to that observed in S but with a narrower width.

Chapter 7

Nernst effect in the F4TCNQ-doped P3HT polymer

Collaborators and Personal Contributions: The doped P3HT bars, their FTIR and WAXS data were provided by Dr. Christian Müller's group at the Chalmers University of Technology, Sweden. The electrical, thermoelectric and thermomagnetic characterizations were done by Md Sabbir Akhanda under the supervision of Dr. Mona Zebarjadi

7.1 Background and context

Wearable electronic devices are becoming an integral part of our daily life. Today these are widely used in applications ranging from sensing and monitoring health and physical activities to communications, security, and the Internet of Things. With the advances in integrated circuits, today's wearable electronic devices need very low power to operate. Hence, the idea of utilizing our body heat to power these wearable devices employing thermoelectric devices is actively being explored [301–304]. Thermoelectric devices are capable of harvesting low-grade thermal energy and converting it to electricity. Thermoelectric power generation relies on the Seebeck coefficient which is the longitudinal electric voltage response to a temperature gradient. The Nernst effect is less studied compared to the well-known Seebeck effect [305–307]. Among the studies performed so far, all are focused on inorganic materials with the exception of a few focusing on organic superconductors including $(\text{TMTSF})_2\text{PF}_6$ and κ -(BEDT-TTF) $_2\text{Cu}(\text{NCS})_2$ and κ

-(BEDT-TTF)₂Cu[N(CN)₂]Br [305, 308–310]. This trend is also prevalent to some extent even in the case of the well-known Seebeck effect, where the studies reported on inorganics far exceed the studies reported on the organic ones [311–316]. While inorganic materials have demonstrated higher zT values, they have some shortcomings. For instance, they are typically brittle and lack mechanical flexibility. They are expensive to process and often have toxic, expensive, or rare elements like Pb, Bi, and Te in their composition, raising health and economic concerns. Conjugated polymers on the other hand are comparatively inexpensive to produce and have better mechanical flexibility. Conjugated polymers also have a low lattice thermal conductivity because of their complex nanostructure and their inherent disorder and are compatible with solution-based printing technologies. All these characteristics make these materials attractive candidates in the quest to develop inexpensive flexible thermoelectric and thermomagnetic devices [317–325].

In general, improving the thermoelectric power factor of a material is difficult because of the coupled nature of the Seebeck coefficient and the electrical conductivity. In most cases, improving one negatively affects the other. Hence, optimizing the transport parameters to find high zT materials is challenging. Materials that show a decoupling trend i.e. simultaneous increase in the Seebeck coefficient and electrical conductivity are therefore interesting from an optimization point of view [326, 327]. In this work, taking the conjugated polymer P3HT (see chemical structure in Fig. 7.6(a) as the host material and F4TCNQ (2,3,5,6-tetrafluoro-7,7,8,8 tetracyanoquinodimethane) (see chemical structure in Fig. 7.6(b) as the dopant, we investigate the temperature dependence of thermoelectric properties as well as the Nernst response. While the Nernst coefficient values are small, they are comparable to many inorganic ones. We report a simultaneous increase of the Seebeck and the electrical conductivity over an extended range of temperatures.

7.2 Results and discussion

The shape of the dye and the pressure applied along the y-axis force P3HT chains to orient along the flow direction (x-axis) [328, 329]. We measured the electrical conduc-

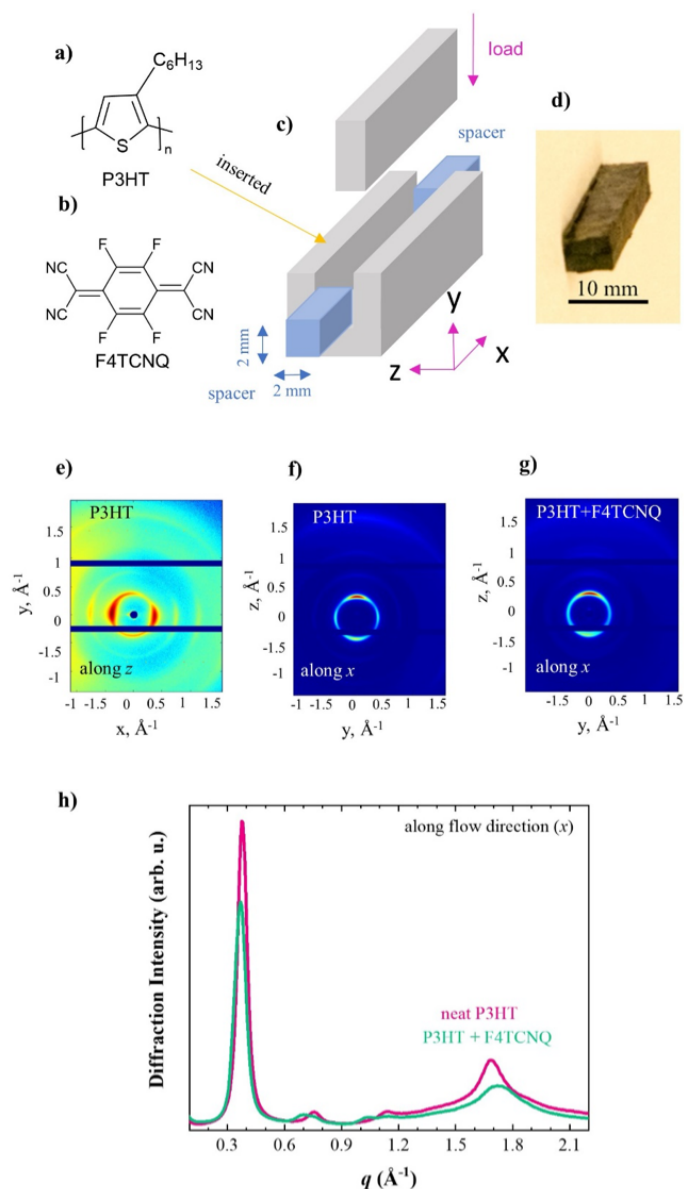


Figure 7.1: Chemical structures of **a)** P3HT and **b)** F4TCNQ. **c)** schematic of the channel die; P3HT is inserted into the channel equipped with 2 spacers and flows along x-axis upon applying force along y-axis accompanied by heating to 100 °C **d)** WAXS images of P3HT bar along **e)** z-axis and **f)** before and **g)** after doping with F4TCNQ. **h)** integrated WAXS diffractogram of the images along x-axis

tivity of sequentially doped P3HT bars (Fig. 7.1(a-d)). The bars S1 and S2 feature an electrical conductivity (σ) of 0.2 ± 0.1 and $0.1 \pm 0.1 \text{ S.cm}^{-1}$ along the x and the z-axis, respectively measured using a two-point method. To further study the anisotropy of the

bars, we recorded WAXS diffractograms (Fig. 7.1(e-f)) along the z and x-axis prior to doping. Images recorded in transmission show higher ordering along the flow direction (x-axis) than transverse to it (z-axis) indicating that the P3HT bar features a high level of anisotropy. The integrated diffractogram of the recorded image along the x-axis shows distinct h00 scattering peaks in case of neat P3HT ($h = 1 - 3$; $q_{100} = 0.37 \text{ \AA}^{-1}$) due to lamellar stacking (Fig. 7.1(h)). A distinct π -stacking peak is observed at $q_{010} = 1.68 \text{ \AA}^{-1}$. Doping with F4TCNQ results in a noticeable change in the position of the diffraction peaks (Fig. 7.1(g)). We observe two h00 scattering peaks, which we assign to the presence of both undoped and doped material. Intercalation of F4TCNQ between the side chains of P3HT increases the distance between adjacent polymer backbones along the lamellar stacking direction, which results in a shift of the h00 scattering peaks to lower q-values. Despite a clear anisotropy in ordering along (x-axis) and transverse (z-axis) to the bar length (Fig. 7.1(e-f)), the conductivity values in these directions are not significantly different. Whereas, it has previously been shown that oriented P3HT chains result in higher conductivity values along the orientation due to higher charge mobility [328]. We speculate that the lack of clear anisotropy in electrical conductivity is due to length of the bar, which limits the dopant diffusion towards the middle. The limitation in the diffusion of F4TCNQ in bulk P3HT samples has been previously reported [328].

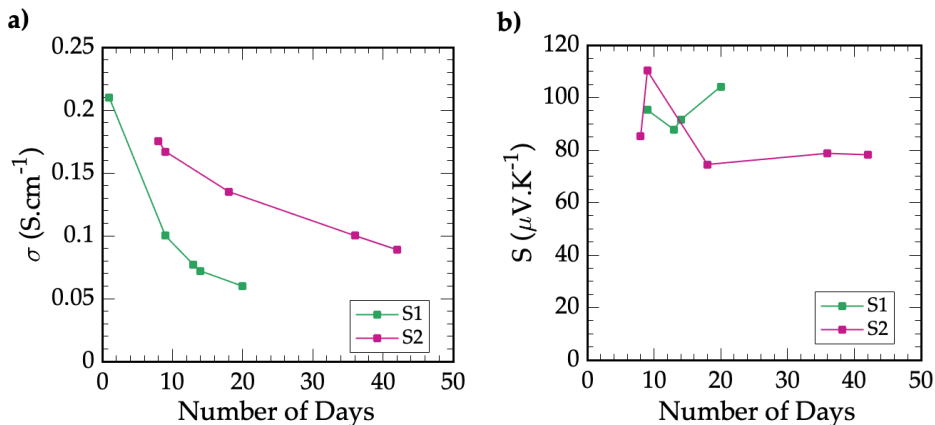


Figure 7.2: Electrical conductivity and Seebeck Coefficient of S1 and S2 obtained from measurements repeated over an extended period of time

To examine the stability of the samples, we repeated the electrical conductivity and the Seebeck coefficient measurements over the span of a few weeks. (see Fig. 7.2) Within

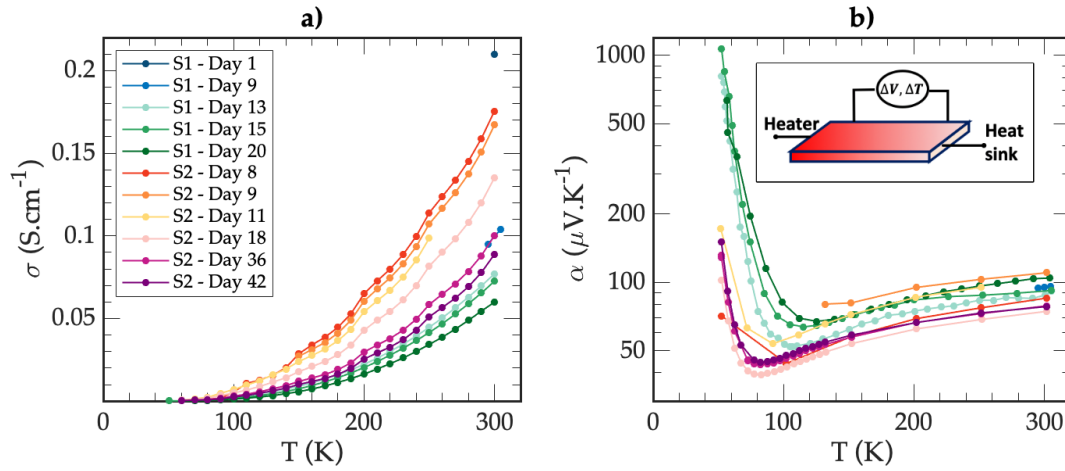


Figure 7.3: Temperature dependence of **a)** electrical conductivity and **b)** Seebeck coefficient of Sample 1 (S1) and Sample 2 (S2) measured over an extended period. Fig. 2b follows the same legend as shown in Fig. 2a. Inset of Fig. 2b shows the schematic of the Seebeck Coefficient measurement connections.

this time period, the samples were exposed to air. The freshest S1 sample (day 1) had an electrical conductivity of 0.21 S.cm^{-1} at 300 K. After 8 days, it's conductivity was reduced by 52 %. Data collected over the subsequent days up to day 20 shows that the electrical conductivity reduction rate decreases everyday and eventually slows down from about 6-7% per day to 2-3 % by day 20. For the sample S2, prepared identically, we saw the rate drops down to 1-2 % after 40 days. Samples thus appear to suffer their biggest loss in terms of electrical conductivity within the first two weeks after which the loss significantly slows down. Stability-wise, we saw an even smaller degree of fluctuations in the Seebeck coefficient for both samples. For sample S1, the Seebeck coefficient at room temperature at day 9 is $95 \mu\text{V.K}^{-1}$. After day 20, it was found to change by only 9.5 %. In the case of sample S2, at 300 K, we saw a change of 13 % from day 8 to day 18. As time progressed, the values stabilized even more and we saw a change of only 5.5 % between day 18 and day 36 while there was no change in value between day 36 and day 42. At day 42, the Seebeck coefficient was measured to be $78 \mu\text{V.K}^{-1}$.

Fig. 7.3 shows the plot of electrical conductivity (four-point method) and Seebeck coefficient measured along the flow direction in the temperature range of 50 K - 305 K. Room temperature electrical conductivities of the samples (S1: 0.1 S.cm^{-1} and S2: 0.17 S.cm^{-1}) are lower compared to those reported for thin-films ($5 - 48 \text{ S.cm}^{-1}$) of the same

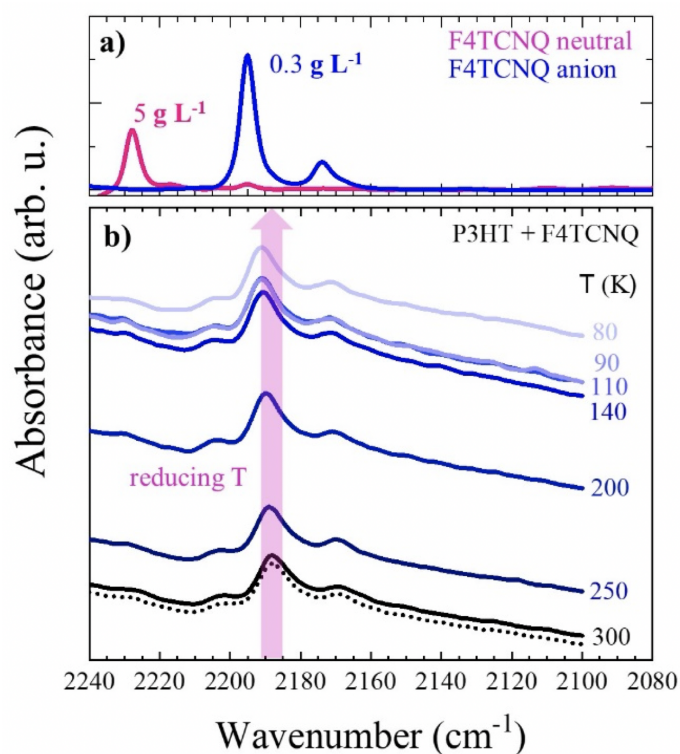


Figure 7.4: FTIR absorption of **a)** F4TCNQ anion (blue) and neutral (pink), **b)** thin film of P3HT doped with F4TCNQ cooled down to 80 K from 300 K (solid lines from black to light blue) and re-heated up to 300 K (dotted black)

host dopant combination by other groups [330–332]. Due to the size of the sample and low diffusion rate, it takes a considerable amount of time for the dopants to diffuse into the samples and in doing so, a doping gradient is created. From a previous study done by Liyang et al. on bulk cube P3HT:F4TCNQ samples (1 mm × 1 mm × 1 mm), we know that the dopant ingresses only about 250 μm over a 14 days of sequential doping. The interior of the cube remained undoped [328]. As a result, only the surface of the bar is heavily doped and conductive while the core of the bar is composed of weakly doped P3HT resulting in a lower overall electrical conductivity compared to uniformly doped thin-films.

Over the entire temperature range, the electrical conductivity increases as the temperature increases. On the contrary, as the temperature increases, the Seebeck coefficient (α) first decreases sharply and then slowly increases. At a temperature around 55 K, the Seebeck coefficient of the two samples can range from several hundred to 1000 $\mu\text{V}\cdot\text{K}^{-1}$ while the electrical conductivity ranges from 10^{-3} to 10^{-4} $\text{S}\cdot\text{cm}^{-1}$. In this temperature

regime, polarons are expected to be in the freeze-out condition. Consequently, the insulating nature of the sample results in a high Seebeck coefficient (e.g. $1078 \mu V.K^{-1}$ on day 14). FTIR absorption was recorded at different temperatures from 300 K to 80 K on a thin film of P3HT doped with F4TCNQ (Fig. 7.4(a-b)) [reprinted from ref Kiefer et al. (2019)[333]]. The anion of F4TCNQ gives rise to distinct absorption peaks at 2195 cm^{-1} and 2175 cm^{-1} that correspond to the cyano stretch vibration (Fig. 7.4(a)) [333]. The shape and size of the peak at 2190 cm^{-1} hardly changes and only shifts to higher energies with decreasing temperature (Fig. 7.4(b)). Therefore, in this range, the sum of the bound and free charges does not change as the temperature changes. Hence, we speculate that, the rise in the electrical conductivity accompanied by a drop in the Seebeck coefficient as temperature increases from 55 K, is mainly due to an increase in the number of free charges while the total number of charges remains constant. Similar Seebeck coefficient and electrical conductivity trends observed in most inorganic samples were explained by a shift of the Fermi level from within the bandgap toward the band edge [35, 334]. This shift is a result of an increase in the amount of free carriers. As the Fermi level shifts more toward the inside of the band gap, the Seebeck coefficient decreases due to the higher symmetry between states above and below the Fermi level [3, 335–337]. The decaying behavior of the Seebeck coefficient, α , with respect to temperatures in P3HT:F4TCNQ can be explained with the following relation obtained using the hopping model for organic thermoelectric materials [338, 339].

$$\alpha = \frac{E_f - E_{trans}}{e.T} \quad (7.1)$$

where, E_{trans} is the transport level, E_f is the Fermi level and e is the elementary charge. An increased number of free charge carriers reduces the activation energy and moves the Fermi level closer to the transport level. Consequently, the Seebeck coefficient decreases. This decreasing trend transitions into a steadily increasing trend at roughly around 100-125 K and 75-100 K for S1 and S2, respectively. For S1, from this transition temperature to 300 K, we see a 70 % and 65 % increase in the Seebeck coefficient on Day 13 and Day 20 respectively. While for S2, on day 18 and Day 36, we recorded an increase of 90 % and 77 % respectively for the same temperature range. In a typical thermoelectric material, an increase in number of carriers typically results in an increase in electrical

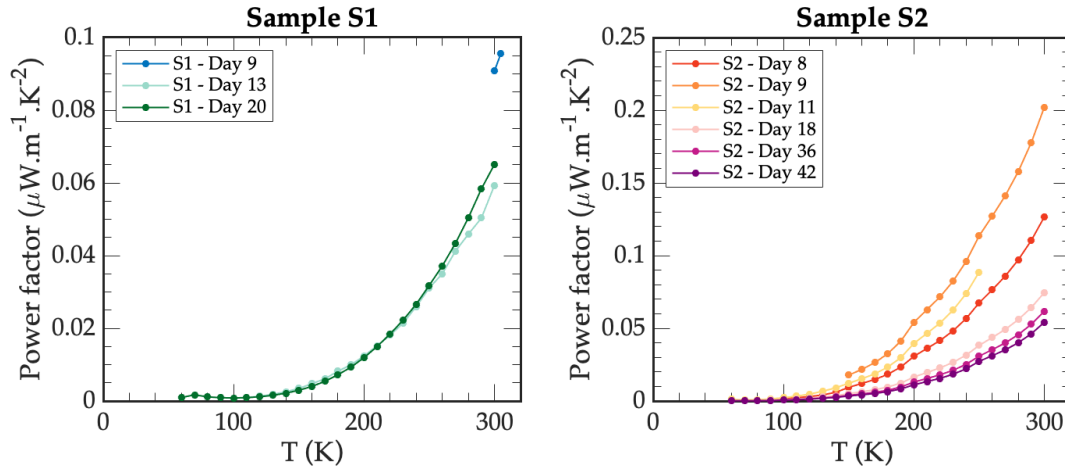


Figure 7.5: Temperature dependence of power factor of Sample S1 and Sample S2 measured over an extended period

conductivity but decrease in the Seebeck coefficient. For polymers, it has been proposed that these two parameters satisfy the following relation: [340]

$$\alpha = \frac{k_B}{e} \left(\frac{\sigma_\alpha}{\sigma} \right)^{\frac{1}{4}} \quad (7.2)$$

where, σ_α is a free parameter set to 1 S.cm^{-1} . Interestingly, both the electrical conductivity and the Seebeck coefficient show an increasing trend starting from the transition temperature (around 100 K for S1 and 70 K for S2) up to 300 K without obeying the above equation. We speculate that, the rise in the electrical conductivity that we see in this region may be originating from the enhancement in mobility with increased temperature but, not from an increase in the free carrier concentration [341]. In this scenario, as we increase the temperature, to keep the number of carriers constant, the Fermi level has to move slightly towards the middle of the band gap. This movement of the Fermi level will result in a rise of the Seebeck coefficient. The power factor defined as $(S^2\sigma)$ also shows an increasing trend in this region (see Fig. 7.5).

The temperature dependence of the average of the Nernst coefficient (N) of the sample S1 measured on Day 11 under three different magnetic field ($B = 1 \text{ T}$, 2 T and 3 T) is shown in Fig. 7.6. The error bar in the figure represents the standard error of the mean of these measurements. Nernst coefficient measured at 290 K is $-0.07 \mu\text{V.K}^{-1}.\text{T}^{-1}$. Decreasing the temperature leads to an increase in the value of the Nernst coefficient. At the lowest temperature measured (80 K) where the sample behaves more like an insula-

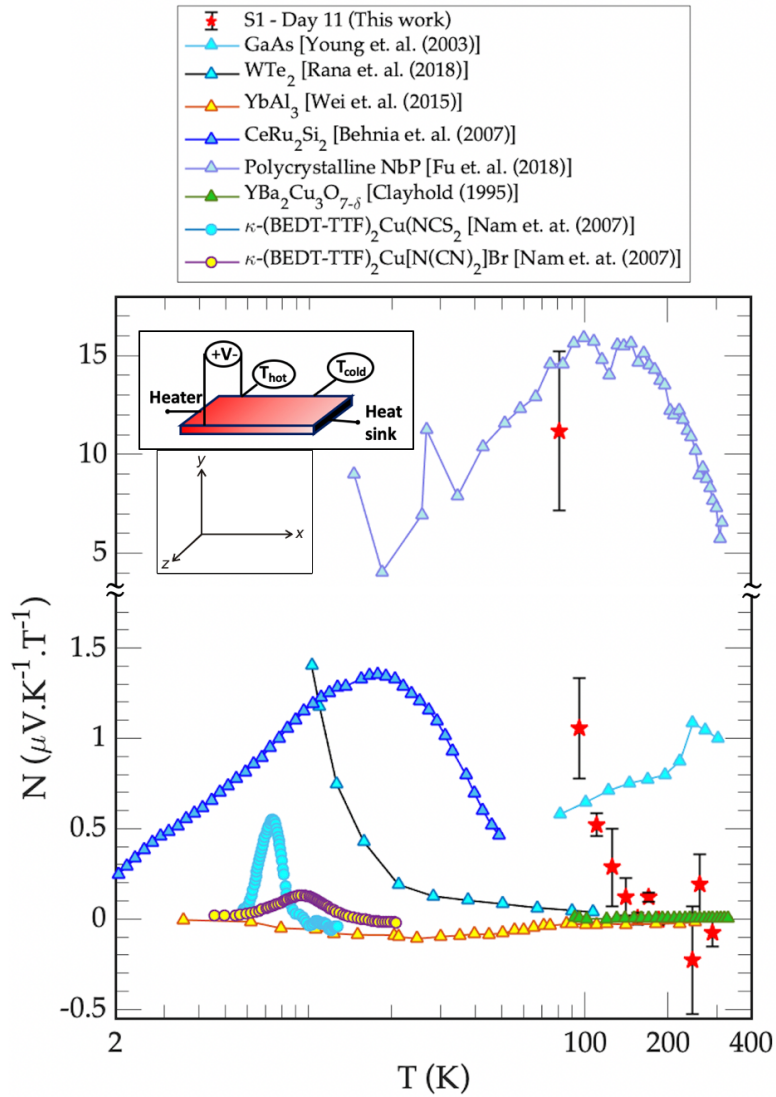


Figure 7.6: Temperature dependence of the Nernst coefficient of Sample 1 (S1) compared with few inorganic and organic materials

tor, we see the largest Nernst signal ($11.2 \mu V.K^{-1}.T^{-1}$) which is approximately 160 times larger than the absolute value of the signal at 290 K. To the best of our knowledge, this is the highest Nernst coefficient to date observed in a polymer. N followed a similar trend to what we observed in the Seebeck measurement. Reports on inorganic materials suggest that a higher mobility to Fermi-energy ratio results in a higher Nernst coefficient. For polymers like P3HT with complex molecular structure, it is hard to draw a similar conclusion without doing detailed theoretical calculation. The values of the Nernst coefficient P3HT:F4TCNQ observed at low temperatures are comparable to many inorganic materials as shown in Fig. 7.6. It is noteworthy to mention that, the value 80 K is greater

than the one observed in the single-crystal Bi_2Te_3 , the most commercially available thermoelectric material, at the same temperature [35]. All these evidences highlights the potential of polymers for thermomagnetic applications [35, 38, 49, 76, 89, 163, 342, 343].

The thermal conductivity (κ) can be written as: $\kappa(T) = a(T).c_p(T).\rho(T)$ where a is the thermal diffusivity in units of $[\text{mm}^2/\text{s}]$, c_p is the specific heat in units of $[\text{J}/(\text{g.K})]$ and ρ is the bulk density in units of $[\text{g}/\text{cm}^3]$. Here, the thermal diffusivity is measured using the laser flash method along the loading direction and was found to be $0.14 \text{ mm}^2/\text{s}$. The density was measured employing the Archimedes' principle and was estimated to be $1.09 \text{ g}/\text{cm}^3$. The room temperature density of a thin-film P3HT has been reported to be $1.11 \text{ g}/\text{cm}^3$ [344]. Taking $1.32 \text{ J}/(\text{g.K})$ as the specific heat, [345] we have estimated that the room temperature thermal conductivity of our sample is approximately $0.2 \text{ W.m}^{-1}.\text{K}^{-1}$ along the loading direction (y-axis). An anisotropic behavior compared to the y-direction is expected for the thermal conductivity measured along the flow (x-axis) direction. Low electrical conductivity of our samples indicate that electronic part of the thermal conductivity will be negligible as Scheunemann and Kemerink showed in 2020 that a polymer with electrical conductivity of 100 S.cm^{-1} will have electronic thermal conductivity in the range of $0.05\text{-}0.1 \text{ W.m}^{-1}.\text{K}^{-1}$ only [346]. Room temperature thermal conductivity of P3HT thin-films reported previously was around $0.185 \text{ W.m}^{-1}.\text{K}^{-1}$ [347, 348].

7.3 Conclusion

In summary, we have studied the transport properties of P3HT bars doped with F4TCNQ. We observed a simultaneous increase in the Seebeck coefficient and the electrical conductivity over an extended temperature range. This result joins a small number of papers reporting a similar simultaneously increasing trend [349–351]. While electrical conductivity increases with temperature in hopping transport, we speculate that the enhancement in the Seebeck coefficient seen in these samples is due to the movement of the Fermi level towards the middle of the band gap due to an increased mobility of the free carriers. At 80 K, we observed a Nernst coefficient (N) which exceeds the N observed in a single-crystal Bi_2Te_3 . Our samples exhibited a thermal conductivity of $0.2 \text{ W.m}^{-1}.\text{K}^{-1}$

at room temperature. The Seebeck coefficient remained relatively stable under ambient conditions over a span of 40 days.

Chapter 8

Outlook

Thermomagnetic materials provide an alternative solution to solid-state cooling and power generation. Thermomagnetic modules and materials have been investigated in parallel to thermoelectric materials for more than a century. However, the study of thermomagnetic materials has attracted much less attention as they generally have lower efficiency at high temperatures. However, these materials and modules have unique advantages and should be regarded as complementary and not as competitors of thermoelectric materials. They are advantageous, for instance, at extremely low temperatures where thermoelectricity is weak. Experimental techniques to measure thermomagnetic transport are more complex and require careful attention to the details of the setup as these are magnetic field-dependent tensor properties. Several competing effects can be responsible for transverse voltage measurements that can introduce errors to the Nernst measurements and have to be carefully separated, such as the thermal Hall effect. Thermomagnetic figure of merit, due to its anisotropy and magnetic-field dependence, is much more difficult to report. There are only a handful of materials for which the thermomagnetic figure of merit is reported. Aside from applications, thermomagnetic transport provides rich physics to study anisotropy, topology, and magnetism features. It is challenging to match the theoretical and experimental Nernst without any fitting parameters due to the small signals and extreme sensitivity of the Nernst thermopower to the details of band structure, scattering rates, and Berry curvature. Nevertheless, through material experimentation and theoretical advancements, guidelines can be developed to identify potential materials with significant thermomagnetic figures of merit.

Bibliography

- [1] H. J. Goldsmid and R. W. Douglas, *The use of semiconductors in thermoelectric refrigeration*, *British Journal of Applied Physics* **5**, 386–390 (1954).
- [2] G. J. Snyder and E. S. Toberer. *Complex thermoelectric materials*. In *Materials for Sustainable Energy: A Collection of Peer-Reviewed Research and Review Articles from Nature Publishing Group*, pages 101–110. World Scientific Publishing Co., (2010).
- [3] G. D. Mahan and J. O. Sofo, *The best thermoelectric*, *Proceedings of the National Academy of Sciences of the United States of America* **93**, 7436–7439 (1996).
- [4] F. J. Disalvo. *Thermoelectric cooling and power generation*, (1999).
- [5] Y. I. Ravich and D. A. Pshena«ê-Severin, *Thermoelectric figure of merit of a p-n junction*, *Semiconductors* **35**, 1161–1165 (2001).
- [6] A. I. Hochbaum, R. Chen, R. D. Delgado, W. Liang, E. C. Garnett, M. Najarian, A. Majumdar, and P. Yang, *Enhanced thermoelectric performance of rough silicon nanowires*, *Nature* **451**, 163–167 (2008).
- [7] A. I. Boukai, Y. Bunimovich, J. Tahir-Kheli, J. K. Yu, W. A. Goddard, and J. R. Heath, *Silicon nanowires as efficient thermoelectric materials*, *Nature* **451**, 168–171 (2008).
- [8] T. C. Harman, P. J. Taylor, M. P. Walsh, and B. E. LaForge, *Quantum dot superlattice thermoelectric materials and devices*, *Science* **297**, 2229–2232 (2002).
- [9] C. Wood, *Materials for thermoelectric energy conversion*, *Reports on Progress in Physics* **51**, 459–539 (1988).
- [10] S. Volz, *Thermal nanosystems and nanomaterials*, Springer Science & Business Media (2009).

- [11] G. S. Nolas, J. L. Cohn, G. A. Slack, and S. B. Schujman, *Semiconducting Ge clathrates: Promising candidates for thermoelectric applications*, Applied Physics Letters **73**, 178–180 (1998).
- [12] M. Zebarjadi, B. Liao, K. Esfarjani, M. Dresselhaus, and G. Chen, *Enhancing the thermoelectric power factor by using invisible dopants*, Advanced Materials **25**, 1577–1582 (2013).
- [13] M. Markov, X. Hu, H. C. Liu, N. Liu, S. J. Poon, K. Esfarjani, and M. Zebarjadi, *Semi-metals as potential thermoelectric materials*, Scientific Reports **8**, 9876 (2018).
- [14] N. Liu, S. E. Rezaei, W. A. Jensen, S. Song, Z. Ren, K. Esfarjani, M. Zebarjadi, and J. A. Floro, *Improved Thermoelectric Performance of Eco-Friendly β -FeSi₂-SiGe Nanocomposite via Synergistic Hierarchical Structuring, Phase Percolation, and Selective Doping*, Advanced Functional Materials **29**, 1903157 (2019).
- [15] M. Dresselhaus, G. Dresselhaus, X. Sun, Z. Zhang, S. Cronin, and T. Koga, *Low-dimensional thermoelectric materials*, Physics of the Solid State **41**, 679–682 (1999).
- [16] G. Chen, M. S. Dresselhaus, G. Dresselhaus, J. P. Fleurial, and T. Caillat, *Recent developments in thermoelectric materials*, International Materials Reviews **48**, 45–66 (2003).
- [17] J. F. Li, W. S. Liu, L. D. Zhao, and M. Zhou. *High-performance nanostructured thermoelectric materials*, (2010).
- [18] M. Zebarjadi, G. Joshi, G. Zhu, B. Yu, A. Minnich, Y. Lan, X. Wang, M. Dresselhaus, Z. Ren, and G. Chen, *Power factor enhancement by modulation doping in bulk nanocomposites*, Nano Letters **11**, 2225–2230 (2011).
- [19] B. Yu, M. Zebarjadi, H. Wang, K. Lukas, H. Wang, D. Wang, C. Opeil, M. Dresselhaus, G. Chen, and Z. Ren, *Enhancement of thermoelectric properties by modulation-doping in silicon germanium alloy nanocomposites*, Nano Letters **12**, 2077–2082 (2012).
- [20] X. Zhang and Y. Pei, *Manipulation of charge transport in thermoelectrics*, npj Quantum Materials **2**, 1–5 (2017).

- [21] H. J. Goldsmid et al., *Introduction to thermoelectricity*, Springer (2010).
- [22] H. Goldsmid, *Thermoelectric refrigeration*, Springer (2013).
- [23] M. Zebarjadi, *Electronic cooling using thermoelectric devices*, Applied Physics Letters **106** (2015).
- [24] M. J. Adams, M. Verosky, M. Zebarjadi, and J. P. Heremans, *High switching ratio variable-temperature solid-state thermal switch based on thermoelectric effects*, International Journal of Heat and Mass Transfer **134**, 114–118 (2019).
- [25] T. Harman, *Theory of the infinite stage Nernst-Ettingshausen refrigerator*, Advanced energy conversion **3**, 667–676 (1963).
- [26] M. M. H. Polash and D. Vashaee, *Infinite-stage Nernst-Ettingshausen cryocooler for practical applications*, Physical Review Applied **15**, 014011 (2021).
- [27] K. F. Hsu, S. Loo, F. Guo, W. Chen, J. S. Dyck, C. Uher, T. Hogan, E. Polychroniadis, and M. G. Kanatzidis, *Cubic $\text{AgPb}_m\text{SbTe}_{2+m}$: Bulk thermoelectric materials with high figure of merit*, Science **303**, 818–821 (2004).
- [28] G. Joshi, H. Lee, Y. Lan, X. Wang, G. Zhu, D. Wang, R. W. Gould, D. C. Cuff, M. Y. Tang, M. S. Dresselhaus, et al., *Enhanced thermoelectric figure-of-merit in nanostructured p-type silicon germanium bulk alloys*, Nano letters **8**, 4670–4674 (2008).
- [29] S. I. Kim, K. H. Lee, H. A. Mun, H. S. Kim, S. W. Hwang, J. W. Roh, D. J. Yang, W. H. Shin, X. S. Li, Y. H. Lee, et al., *Dense dislocation arrays embedded in grain boundaries for high-performance bulk thermoelectrics*, Science **348**, 109–114 (2015).
- [30] A. F. May, J.-P. Fleurial, and G. J. Snyder, *Thermoelectric performance of lanthanum telluride produced via mechanical alloying*, Physical Review B **78**, 125205 (2008).
- [31] D.-Y. Chung, T. P. Hogan, M. Rocci-Lane, P. Brazis, J. R. Ireland, C. R. Kannewurf, M. Bastea, C. Uher, and M. G. Kanatzidis, *A new thermoelectric material: CsBi_4Te_6* , Journal of the American Chemical Society **126**, 6414–6428 (2004).

- [32] W. Liu, X. Tan, K. Yin, H. Liu, X. Tang, J. Shi, Q. Zhang, and C. Uher, *Convergence of conduction bands as a means of enhancing thermoelectric performance of n-type $Mg_2Si_{1-x}Sn_x$ solid solutions*, *Physical review letters* **108**, 166601 (2012).
- [33] P. F. Poudeu, J. D'Angelo, A. D. Downey, J. L. Short, T. P. Hogan, and M. G. Kanatzidis, *High thermoelectric figure of merit and nanostructuring in bulk p-type $Na_{1-x}Pb_mSb_yTe_{m+2}$* , *Angewandte Chemie International Edition* **45**, 3835–3839 (2006).
- [34] K. Biswas, J. He, I. D. Blum, C.-I. Wu, T. P. Hogan, D. N. Seidman, V. P. Dravid, and M. G. Kanatzidis, *High-performance bulk thermoelectrics with all-scale hierarchical architectures*, *Nature* **489**, 414–418 (2012).
- [35] M. S. Akhanda, S. E. Rezaei, K. Esfarjani, S. Krylyuk, A. V. Davydov, and M. Zebarjadi, *Thermomagnetic properties of Bi_2Te_3 single crystal in the temperature range from 55 K to 380 K*, *Physical Review Materials* **5**, 015403 (2021).
- [36] W. Yim and A. Amith, *Bi-Sb alloys for magneto-thermoelectric and thermomagnetic cooling*, *Solid-State Electronics* **15**, 1141–1165 (1972).
- [37] J. Xiang, S. Hu, M. Lyu, W. Zhu, C. Ma, Z. Chen, F. Steglich, G. Chen, and P. Sun, *Large transverse thermoelectric figure of merit in a topological Dirac semimetal*, *Science China Physics, Mechanics & Astronomy* **63**, 1–7 (2020).
- [38] K. Behnia, M.-A. Méasson, and Y. Kopelevich, *Nernst effect in semimetals: The effective mass and the figure of merit*, *Physical review letters* **98**, 076603 (2007).
- [39] T. Yamashita, Y. Shimoyama, Y. Haga, T. Matsuda, E. Yamamoto, Y. Onuki, H. Sumiyoshi, S. Fujimoto, A. Levchenko, T. Shibauchi, et al., *Colossal thermomagnetic response in the exotic superconductor URu_2Si_2* , *Nature Physics* **11**, 17–20 (2015).
- [40] J. Cohn, B. White, C. Dos Santos, and J. Neumeier, *Giant Nernst effect and bipolarity in the quasi-one-dimensional metal $Li_{0.9}Mo_6O_{17}$* , *Physical review letters* **108**, 056604 (2012).
- [41] E. F. Scott, K. A. Schlaak, P. Chakraborty, C. Fu, S. N. Guin, S. Khodabakhsh, A. E. P. y Puente, C. Felser, B. Skinner, and S. J. Watzman, *Doping as a tuning mech-*

- anism for magnetothermoelectric effects to improve zT in polycrystalline NbP*, Physical Review B **107**, 115108 (2023).
- [42] P. Li, P. Qiu, Q. Xu, J. Luo, Y. Xiong, J. Xiao, N. Aryal, Q. Li, L. Chen, and X. Shi, *Colossal Nernst power factor in topological semimetal NbSb₂*, Nature Communications **13**, 7612 (2022).
- [43] C. Fu, S. N. Guin, T. Scaffidi, Y. Sun, R. Saha, S. J. Watzman, A. K. Srivastava, G. Li, W. Schnelle, S. S. Parkin, et al., *Largely suppressed magneto-thermal conductivity and enhanced magneto-thermoelectric properties in PtSn₄*, Research **2020** (2020).
- [44] Y. Pan, B. He, T. Helm, D. Chen, W. Schnelle, and C. Felser, *Ultrahigh transverse thermoelectric power factor in flexible Weyl semimetal WTe₂*, Nature communications **13**, 3909 (2022).
- [45] P. Wang, C.-w. Cho, F. Tang, P. Wang, W. Zhang, M. He, G. Gu, X. Wu, Y. Shao, and L. Zhang, *Giant Nernst effect and field-enhanced transversal $z_N T$ in ZrTe₅*, Physical Review B **103**, 045203 (2021).
- [46] A. v. Ettingshausen and W. Nernst, *Ueber das Auftreten electromotorischer Kräfte in Metallplatten, welche von einem Wärmestrome durchflossen werden und sich im magnetischen Felde befinden*, Annalen der Physik und Chemie **265**, 343–347 (1886).
- [47] E. H. Hall, *Measurement of the four magnetic transverse effects*, Physical Review **26**, 820–840 (1925).
- [48] P. W. Bridgman, *The connections between the four transverse galvanomagnetic and thermomagnetic phenomena*, Physical Review **24**, 644–651 (1924).
- [49] J. Clayhold, *Nernst effect in anisotropic metals*, Physical Review B **54**, 6103–6106 (1996).
- [50] V. D. Ky, *Planar Hall and Nernst effect in ferromagnetic metals*, physica status solidi (b) **22**, 729–736 (1967).
- [51] R. B. Horst, *Thermomagnetic Figure of Merit: Bismuth*, Journal of Applied Physics **34**, 3246–3254 (1963).

- [52] R. T. Delves, *Thermomagnetic effects in semiconductors and semimetals*, Reports on Progress in Physics **28**, 249–289 (1965).
- [53] D. Armitage and H. Goldsmid, *Magneto-Seebeck and Nernst effects in cadmium arsenide*, Journal of Physics C: Solid State Physics **2**, 2389 (1969).
- [54] W. Williams, *Some Adiabatic and Isothermal Effects in Bismuth Telluride*, Proceedings of the Physical Society **73**, 739–744 (1959).
- [55] M. K. Zhitinskaya, S. A. Nemov, and T. E. Svechnikova, *Effect of inhomogeneities of Bi_2T_3 crystals on the transverse Nernst-Ettingshausen effect*, Semiconductors **31**, 375–377 (1997).
- [56] R. Mansfield and W. Williams, *The Electrical Properties of Bismuth Telluride*, Proceedings of the Physical Society **72**, 733–741 (1958).
- [57] E. H. Putley, *Thermoelectric and galvanomagnetic effects in lead selenide and telluride*, Proceedings of the Physical Society. Section B **68**, 35–42 (1955).
- [58] A. W. Smith, *The Hall effect and allied phenomena in rare metals and alloys*, Physical Review **8**, 79 (1916).
- [59] A. W. Smith, *The transverse thermomagnetic effect in nickel and cobalt*, Physical Review (Series I) **33**, 295 (1911).
- [60] E. H. Hall and L. Campbell. *On the Electromagnetic and the Thermomagnetic Transverse and Longitudinal Effects in Soft Iron*. In *Proceedings of the American Academy of Arts and Sciences*, volume 46, pages 625–668. JSTOR, (1911).
- [61] A. W. Smith, *The Hall Effect and Some Allied Effects*, Physical Review **1**, 339 (1913).
- [62] M. Steele and J. Babiskin, *Oscillatory thermomagnetic properties of a bismuth single crystal at liquid helium temperatures*, Physical Review **98**, 359 (1955).
- [63] C. Herring, T. Geballe, and J. Kunzler, *Analysis of Phonon-Drag Thermomagnetic Effects in n-Type Germanium*, Bell System Technical Journal **38**, 657–747 (1959).
- [64] O. E. Buckley, *The Hall effect and allied phenomena in silicon*, Physical Review **4**, 482 (1914).

- [65] E. Putley, *Thermoelectric and galvanomagnetic effects in lead selenide and telluride*, Proceedings of the Physical Society. Section B **68**, 35 (1955).
- [66] F. E. Jaumot, *Thermoelectric effects*, Proceedings of the IRE **46**, 538–554 (1958).
- [67] P. Price, *Theory of transport effects in semiconductors: The nernst coefficient, and its relation to thermoelectric power*, Physical Review **102**, 1245 (1956).
- [68] T. Harman, J. Honig, S. Fischler, A. Paladino, and M. Button, *Experiments on Room-Temperature Nernst-Ettingshausen Refrigerators*, Journal of Engineering for Industry **87**, 21–24 (1965).
- [69] T. Harman, J. Honig, S. Fischler, A. Paladino, and M. J. Button, *Oriented single-crystal Bismuth Nernst-Ettingshausen refrigerators*, Applied Physics Letters **4**, 77–79 (1964).
- [70] G. L. Guthrie, *Optimization of the Cross-Sectional Geometry of Nernst-Ettingshausen Devices*, Journal of Applied Physics **36**, 3118–3122 (1965).
- [71] D. A. Wright, *Theory of the Nernst-Ettingshausen generator*, British Journal of Applied Physics **13**, 583–586 (1962).
- [72] J. Honig and B. Tarmy, *Refined Treatment of the Theory Pertaining to Operating Characteristics of Anisotropic Nernst-Ettingshausen Devices*, Journal of Applied Physics **35**, 722–723 (1964).
- [73] P. He, S. S.-L. Zhang, D. Zhu, S. Shi, O. G. Heinonen, G. Vignale, and H. Yang, *Nonlinear planar Hall effect*, Physical review letters **123**, 016801 (2019).
- [74] M. Hirschberger, L. Spitz, T. Nomoto, T. Kurumaji, S. Gao, J. Masell, T. Nakajima, A. Kikkawa, Y. Yamasaki, H. Sagayama, et al., *Topological Nernst effect of the two-dimensional skyrmion lattice*, Physical Review Letters **125**, 076602 (2020).
- [75] Y. Shiomi, N. Kanazawa, K. Shibata, Y. Onose, and Y. Tokura, *Topological Nernst effect in a three-dimensional skyrmion-lattice phase*, Physical Review B **88**, 064409 (2013).
- [76] K. Behnia, *The Nernst effect and the boundaries of the Fermi liquid picture*, Journal of Physics Condensed Matter **21**, 113101 (2009).

- [77] K. Behnia and H. Aubin, *Nernst effect in metals and superconductors: a review of concepts and experiments*, Reports on Progress in Physics **79**, 046502 (2016).
- [78] M. Ikhlas, T. Tomita, T. Koretsune, M.-T. Suzuki, D. Nishio-Hamane, R. Arita, Y. Otani, and S. Nakatsuji, *Large anomalous Nernst effect at room temperature in a chiral antiferromagnet*, Nature Physics **13**, 1085–1090 (2017).
- [79] S. Meyer, Y.-T. Chen, S. Wimmer, M. Althammer, T. Wimmer, R. Schlitz, S. Geprägs, H. Huebl, D. Ködderitzsch, H. Ebert, et al., *Observation of the spin Nernst effect*, Nature materials **16**, 977–981 (2017).
- [80] Z. Shi, S.-J. Xu, L. Ma, S.-M. Zhou, and G.-Y. Guo, *Anomalous Nernst Effect in Epitaxial $L_{10}FePd_{1-x}Pt_x$ Alloy Films: Berry Curvature and Thermal Spin Current*, Physical Review Applied **13**, 054044 (2020).
- [81] G. Moreau, *Sur les phénomènes thermomagnétiques*, Journal de Physique Théorique et Appliquée **9**, 497–506 (1900).
- [82] R. Mansfield and W. Williams, *The electrical properties of bismuth telluride*, Proceedings of the Physical Society **72**, 733 (1958).
- [83] E. Sondheimer, *The theory of the galvanomagnetic and thermomagnetic effects in metals*, Proceedings of the Royal Society of London. Series A. Mathematical and Physical Sciences **193**, 484–512 (1948).
- [84] A. Sommerfeld and N. H. Frank, *The Statistical theory of thermoelectric, galvano-and thermomagnetic phenomena in metals*, Reviews of Modern Physics **3**, 1 (1931).
- [85] E. Putley, *Thermo-and Galvano-Magnetic Coefficients for Semiconductors*, Proceedings of the Physical Society. Section B **65**, 991 (1952).
- [86] H. Nakamura, K. Ikeda, and S. Yamaguchi. *Physical model of Nernst element*. In *Seventeenth International Conference on Thermoelectrics. Proceedings ICT98 (Cat. No. 98TH8365)*, pages 97–100. IEEE, (1998).
- [87] H. Okumura, Y. Hasegawa, H. Nakamura, and S. Yamaguchi. *A computational model of thermoelectric and thermomagnetic semiconductors*. In *Eighteenth International*

- Conference on Thermoelectrics. Proceedings, ICT'99 (Cat. No. 99TH8407)*, pages 209–212. IEEE, (1999).
- [88] D. Pikulin, C.-Y. Hou, and C. Beenakker, *Nernst effect beyond the relaxation-time approximation*, *Physical Review B* **84**, 035133 (2011).
- [89] M. Zebarjadi, S. E. Rezaei, M. S. Akhanda, and K. Esfarjani, *Nernst coefficient within relaxation time approximation*, *Physical Review B* **103**, 144404 (2021).
- [90] Z. Zhu, H. Yang, B. Fauque, Y. Kopelevich, and K. Behnia, *Nernst effect and dimensionality in the quantum limit*, *Nature Physics* **6**, 26–29 (2010).
- [91] E. Thanou-Christodoulaki, C. Papastaikoudis, and G. Mair, *Quantum oscillations of the Nernst effect in single crystals of gallium*, *Journal of Physics F: Metal Physics* **12**, 1421 (1982).
- [92] Z. Alisultanov, *On the theory of Nernst-Ettingshausen oscillations in monolayer and bilayer graphene*, *Physics Letters A* **378**, 2329–2331 (2014).
- [93] Y. V. Sharlai and G. Mikitik, *Oscillations of the Nernst coefficient in bismuth*, *Physical Review B* **83**, 085103 (2011).
- [94] G. Pizzi, D. Volja, B. Kozinsky, M. Fornari, and N. Marzari, *BoltzWann: A code for the evaluation of thermoelectric and electronic transport properties with a maximally-localized Wannier functions basis*, *Computer Physics Communications* **185**, 422–429 (2014).
- [95] G. K. Madsen and D. J. Singh, *BoltzTraP. A code for calculating band-structure dependent quantities*, *Computer Physics Communications* **175**, 67–71 (2006).
- [96] S. E. Rezaei, M. Zebarjadi, and K. Esfarjani, *Calculation of thermomagnetic properties using first-principles density functional theory*, *Computational Materials Science* **210**, 111412 (2022).
- [97] S. E. Rezaei, M. Zebarjadi, and K. Esfarjani, *First-principles-aided evaluation of the Nernst coefficient beyond the constant relaxation time approximation*, *Computational Materials Science* **225**, 112193 (2023).

- [98] A. M. Ganose, J. Park, A. Faghaninia, R. Woods-Robinson, K. A. Persson, and A. Jain, *Efficient calculation of carrier scattering rates from first principles*, *Nature communications* **12**, 2222 (2021).
- [99] Z. Soleimani, S. Zoras, B. Ceranic, S. Shahzad, and Y. Cui, *A review on recent developments of thermoelectric materials for room-temperature applications*, *Sustainable Energy Technologies and Assessments* **37**, 100604 (2020).
- [100] M. Yao, C. Opeil, S. Wilson, and M. Zebarjadi, *Experimental determination of phonon thermal conductivity and Lorenz ratio of single-crystal bismuth telluride*, *MRS Communications* **7**, 922–927 (2017).
- [101] I. T. Witting, T. C. Chasapis, F. Ricci, M. Peters, N. A. Heinz, G. Hautier, and G. J. Snyder, *The Thermoelectric Properties of Bismuth Telluride*, *Advanced Electronic Materials* **5**, 1800904 (2019).
- [102] P. Graziosi, C. Kumarasinghe, and N. Neophytou, *Impact of the scattering physics on the power factor of complex thermoelectric materials*, *Journal of Applied Physics* **126**, 155701 (2019).
- [103] M. Markov, S. E. Rezaei, S. N. Sadeghi, K. Esfarjani, and M. Zebarjadi, *Thermoelectric properties of semimetals*, *Physical Review Materials* **3**, 095401 (2019).
- [104] D. X. Qu, Y. S. Hor, J. Xiong, R. J. Cava, and N. P. Ong, *Quantum oscillations and hall anomaly of surface states in the topological insulator Bi_2Te_3* , *Science* **329**, 821–824 (2010).
- [105] C. B. Satterthwaite and R. W. Ure, *Electrical and Thermal Properties of Bi_2Te_3* , *Physical Review* **108**, 1164–1170 (1957).
- [106] H. Zhang, C. X. Liu, X. L. Qi, X. Dai, Z. Fang, and S. C. Zhang, *Topological insulators in Bi_2Se_3 , Bi_2Te_3 and Sb_2Te_3 with a single Dirac cone on the surface*, *Nature Physics* **5**, 438–442 (2009).
- [107] P. Larson, S. Mahanti, and M. Kanatzidis, *Electronic structure and transport of Bi_2Te_3 and BaBiTe_3* , *Physical Review B - Condensed Matter and Materials Physics* **61**, 8162–8171 (2000).

- [108] S. J. Youn and A. J. Freeman, *First-principles electronic structure and its relation to thermoelectric properties of Bi_2Te_3* , *Physical Review B - Condensed Matter and Materials Physics* **63**, 085112 (2001).
- [109] T. J. Scheidemantel, C. Ambrosch-Draxl, T. Thonhauser, J. V. Badding, and J. O. Sofo, *Transport coefficients from first-principles calculations*, *Physical Review B* **68**, 125210 (2003).
- [110] M. Kim, A. J. Freeman, and C. B. Geller, *Screened exchange LDA determination of the ground and excited state properties of thermoelectrics: Bi_2Te_3* , *Physical Review B* **72**, 035205 (2005).
- [111] B.-L. Huang and M. Kaviani, *Ab initio and molecular dynamics predictions for electron and phonon transport in bismuth telluride*, *Physical Review B* **77**, 125209 (2008).
- [112] B. Y. Yavorsky, N. F. Hinsche, I. Mertig, and P. Zahn, *Electronic structure and transport anisotropy of Bi_2Te_3 and Sb_2Te_3* , *Physical Review B - Condensed Matter and Materials Physics* **84**, 165208 (2011).
- [113] B. Ryu and M.-W. Oh, *Computational Simulations of Thermoelectric Transport Properties*, *Journal of the Korean Ceramic Society* **53**, 273–281 (2016).
- [114] T. Fang, X. Li, C. Hu, Q. Zhang, J. Yang, W. Zhang, X. Zhao, D. Singh, and T. Zhu, *Complex Band Structures and Lattice Dynamics of Bi_2Te_3 -Based Compounds and Solid Solutions*, *Advanced Functional Materials* **29**, 1900677 (2019).
- [115] H. J. Goldsmid, *The Electrical Conductivity and Thermoelectric Power of Bismuth Telluride*, *Proceedings of the Physical Society* **71**, 633–646 (1958).
- [116] J. R. Drabble, R. D. Groves, and R. Wolfe, *Galvanomagnetic Effects in n-Type Bismuth Telluride*, *Proceedings of the Physical Society* **71**, 430–443 (1958).
- [117] J. R. Drabble, *Galvanomagnetic effects in p-type bismuth telluride*, *Proceedings of the Physical Society* **72**, 380–390 (1958).
- [118] P. A. Walker, *The Thermal Conductivity and Thermoelectric Power of Bismuth Telluride at Low Temperatures*, *Proceedings of the Physical Society* **76**, 113–126 (1960).

- [119] H. J. Goldsmid, *Heat Conduction in Bismuth Telluride*, Proceedings of the Physical Society **72**, 17–26 (1958).
- [120] H. J. Goldsmid, *The Ettingshausen figure of merit of bismuth and bismuth - antimony alloys*, British Journal of Applied Physics **14**, 271–274 (1963).
- [121] T. C. Harman and J. M. Honig, *Theory of galvano-thermomagnetic energy conversion devices. II. Refrigerators and heat pumps*, Journal of Applied Physics **33**, 3188–3194 (1962).
- [122] M. Mizuguchi and S. Nakatsuji. *Energy-harvesting materials based on the anomalous Nernst effect*, (2019).
- [123] N. Roschewsky, E. S. Walker, P. Gowtham, S. Muschinske, F. Hellman, S. R. Bank, and S. Salahuddin, *Spin-orbit torque and Nernst effect in Bi-Sb/Co heterostructures*, Physical Review B **99**, 195103–195104 (2019).
- [124] A. Bose, A. S. Shukla, S. Dutta, S. Bhuktare, H. Singh, and A. A. Tulapurkar, *Control of magnetization dynamics by spin-Nernst torque*, Phys. Rev. B **98**, 184412 (2018).
- [125] C. Champness and A. Kipling, *The nernst and magnetoresistance effects in nonstoichiometric bismuth telluride*, Journal of Physics and Chemistry of Solids **27**, 1409–1421 (1966).
- [126] R. Mansfield and W. Williams, *The electrical properties of bismuth telluride*, Proceedings of the Physical Society **72**, 733 (1958).
- [127] T. Hirahara, T. Nagao, I. Matsuda, G. Bihlmayer, E. V. Chulkov, Y. M. Koroteev, P. M. Echenique, M. Saito, and S. Hasegawa, *Role of Spin-Orbit Coupling and Hybridization Effects in the Electronic Structure of Ultrathin Bi Films*, Physical Review Letters **97**, 146803 (2006).
- [128] K. Xiong, W. Wang, H. N. Alshareef, R. P. Gupta, J. B. White, B. E. Gnade, and K. Cho, *Electronic structures and stability of Ni/Bi₂Te₃ and Co/Bi₂Te₃ interfaces*, Journal of Physics D: Applied Physics **43**, 115303 (2010).

- [129] H. Zhang, X. Luo, C. Wang, Y. Xiong, S. Li, and X. Chen, *Characterization of nanocrystalline bismuth telluride (Bi_2Te_3) synthesized by a hydrothermal method*, *Journal of Crystal Growth* **265**, 558–562 (2004).
- [130] S. Shigetomi and S. Mori, *Electrical Properties of Bi_2Te_3* , *Journal of the Physical Society of Japan* **11**, 915–919 (1956).
- [131] C. H. Champness and A. L. Kipling, *The Hall and Seebeck effects in nonstoichiometric bismuth telluride*, *Canadian Journal of Physics* **44**, 769–788 (1966).
- [132] J. P. Heremans, R. J. Cava, and N. Samarth, *Tetradymites as thermoelectrics and topological insulators*, *Nature Reviews Materials* **2**, 17049 (2017).
- [133] S. Cai, J. Guo, V. A. Sidorov, Y. Zhou, H. Wang, G. Lin, X. Li, Y. Li, K. Yang, A. Li, et al., *Independence of topological surface state and bulk conductance in three-dimensional topological insulators*, *Npj Quantum Materials* **3**, 62 (2018).
- [134] J. Liang, L. Cheng, J. Zhang, H. Liu, and Z. Zhang, *Maximizing the thermoelectric performance of topological insulator Bi_2Te_3 films in the few-quintuple layer regime*, *Nanoscale* **8**, 8855–8862 (2016).
- [135] G. S. Nolas, J. Yang, and H. J. Goldsmid. *Semiconductors and Thermoelectric Materials*. In *Thermal Conductivity*, pages 123–152. Springer US, (2006).
- [136] W. Thomson, *On a mechanical theory of thermo-electric currents*, *Proceedings of the Royal Society of Edinburgh* **3**, 91–98 (1851).
- [137] K. Behnia, *Fundamentals of Thermoelectricity*, Oxford University Press (2015).
- [138] A. C. Smith, J. F. Janak, and R. B. Adler. *Electronic conduction in solids*. Technical report, McGraw-Hill,, (1967).
- [139] F. J. Di Salvo, D. Moncton, and J. Waszczak, *Electronic properties and superlattice formation in the semimetal TiSe_2* , *Physical Review B* **14**, 4321 (1976).
- [140] N. Wakabayashi, H. Smith, K. Woo, and F. Brown, *Phonons and charge density waves in $1T\text{-TiSe}_2$* , *Solid State Communications* **28**, 923–926 (1978).

- [141] S. Jaswal, *Lattice dynamics of TiSe₂*, Physical Review B **20**, 5297 (1979).
- [142] K. Rossnagel, L. Kipp, and M. Skibowski, *Charge-density-wave phase transition in 1T-TiSe₂: Excitonic insulator versus band-type Jahn-Teller mechanism*, Physical Review B **65**, 235101 (2002).
- [143] A. Wegner, J. Zhao, J. Li, J. Yang, A. Anikin, G. Karapetrov, K. Esfarjani, D. Louca, and U. Chatterjee, *Evidence for pseudo-Jahn-Teller distortions in the charge density wave phase of 1T-TiSe₂*, Physical Review B **101**, 195145 (2020).
- [144] H. Cercellier, C. Monney, F. Clerc, C. Battaglia, L. Despont, M. Garnier, H. Beck, P. Aebi, L. Patthey, H. Berger, et al., *Evidence for an excitonic insulator phase in 1T-TiSe₂*, Physical review letters **99**, 146403 (2007).
- [145] J. van Wezel, P. Nahai-Williamson, and S. S. Saxena, *Exciton-phonon-driven charge density wave in TiSe₂*, Physical Review B **81**, 165109 (2010).
- [146] R. Bachrach, M. Skibowski, and F. C. Brown, *Angle-Resolved Photoemission from TiSe₂ Using Synchrotron Radiation*, Physical Review Letters **37**, 40 (1976).
- [147] R. Friend, D. Jerome, W. Liang, C. Mikkelsen, and A. Yoffe, *Semimetallic character of TiSe₂ and semiconductor character of TiS₂ under pressure*, Journal of Physics C: Solid State Physics **10**, L705 (1977).
- [148] J. C. Rasch, T. Stemmler, B. Müller, L. Dudy, and R. Manzke, *1T-TiSe₂: Semimetal or Semiconductor?*, Physical review letters **101**, 237602 (2008).
- [149] N. Stoffel, S. Kevan, and N. Smith, *Experimental band structure of 1T-TiSe₂ in the normal and charge-density-wave phases*, Physical Review B **31**, 8049 (1985).
- [150] M. D. Watson, O. J. Clark, F. Mazzola, I. Marković, V. Sunko, T. K. Kim, K. Rossnagel, and P. D. King, *Orbital- and *k_z*-selective hybridization of Se 4*p* and Ti 3*d* states in the charge density wave phase of TiSe₂*, Physical review letters **122**, 076404 (2019).
- [151] G. Li, W. Hu, D. Qian, D. Hsieh, M. Hasan, E. Morosan, R. J. Cava, and N. Wang, *Semimetal-to-Semimetal Charge Density Wave Transition in 1T-TiSe₂*, Physical review letters **99**, 027404 (2007).

- [152] T. Pillo, J. Hayoz, H. Berger, F. Lévy, L. Schlapbach, and P. Aebi, *Photoemission of bands above the Fermi level: The excitonic insulator phase transition in 1 T- TiSe 2*, Physical Review B **61**, 16213 (2000).
- [153] T. Kidd, T. Miller, M. Chou, and T.-C. Chiang, *Electron-hole coupling and the charge density wave transition in TiSe 2*, Physical review letters **88**, 226402 (2002).
- [154] P. Knowles, B. Yang, T. Muramatsu, O. Moulding, J. Buhot, C. J. Sayers, E. Da Como, and S. Friedemann, *Fermi surface reconstruction and electron dynamics at the charge-density-wave transition in ti s e 2*, Physical Review Letters **124**, 167602 (2020).
- [155] S. Wang, J. Yang, T. Toll, J. Yang, W. Zhang, and X. Tang, *Conductivity-limiting bipolar thermal conductivity in semiconductors*, Scientific reports **5**, 10136 (2015).
- [156] R. Modak, M. Murata, D. Hou, A. Miura, R. Iguchi, B. Xu, R. Guo, J. Shiomi, Y. Sakuraba, and K. I. Uchida, *Phase-transition-induced giant Thomson effect for thermoelectric cooling*, Applied Physics Reviews **9**, 011414 (2022).
- [157] K. I. Uchida, M. Murata, A. Miura, and R. Iguchi, *Observation of the Magneto-Thomson Effect*, Physical Review Letters **125**, 106601 (2020).
- [158] R. Modak, M. Murata, D. Hou, A. Miura, R. Iguchi, B. Xu, R. Guo, J. Shiomi, Y. Sakuraba, and K.-i. Uchida, *Phase-transition-induced giant Thomson effect for thermoelectric cooling*, Applied Physics Reviews **9** (2022).
- [159] M. S. Akhanda, S. Krylyuk, D. A. Dickie, A. V. Davydov, F. Han, M. Li, and M. Zebarjadi, *Phase-transition-induced thermal hysteresis in Type-II Weyl semimetals MoTe₂ and Mo_{1-x}W_xTe₂*, Materials Today Physics **29**, 100918 (2022).
- [160] M. Zebarjadi and O. Akbari, *A Model for Material Metrics in Thermoelectric Thomson Coolers*, Entropy **25**, 1540 (2023).
- [161] H. Jones and C. Zener, *The theory of the change in resistance in a magnetic field*, Proceedings of the Royal Society of London. Series A, Containing Papers of a Mathematical and Physical Character **145**, 268–277 (1934).

- [162] D. J. Campbell, C. Eckberg, P. Y. Zavalij, H.-H. Kung, E. Razzoli, M. Michiardi, C. Jozwiak, A. Bostwick, E. Rotenberg, A. Damascelli, et al., *Intrinsic insulating ground state in transition metal dichalcogenide TiSe_2* , *Physical Review Materials* **3**, 053402 (2019).
- [163] K. G. Rana, F. K. Dejene, N. Kumar, C. R. Rajamathi, K. Sklarek, C. Felser, and S. S. Parkin, *Thermopower and Unconventional Nernst Effect in the Predicted Type-II Weyl Semimetal WTe_2* , *Nano Letters* **18**, 6591–6596 (2018).
- [164] S. J. Watzman, T. M. McCormick, C. Shekhar, S.-C. C. Wu, Y. Sun, A. Prakash, C. Felser, N. Trivedi, and J. P. Heremans, *Dirac dispersion generates unusually large Nernst effect in Weyl semimetals*, *Physical Review B* **97**, 161404 (2018).
- [165] F. Caglieris, C. Wuttke, S. Sykora, V. Süß, C. Shekhar, C. Felser, B. Büchner, and C. Hess, *Anomalous Nernst effect and field-induced Lifshitz transition in the Weyl semimetals TaP and TaAs* , *Physical Review B* **98**, 201107 (2018).
- [166] F. Han, N. Andrejevic, T. Nguyen, V. Kozii, Q. T. Nguyen, T. Hogan, Z. Ding, R. Pablo-Pedro, S. Parjan, B. Skinner, et al., *Quantized thermoelectric Hall effect induces giant power factor in a topological semimetal*, *Nature communications* **11**, 6167 (2020).
- [167] Y.-f. Yang, *Universal behavior in the Nernst effect of heavy fermion materials*, *Physical Review Research* **2**, 033105 (2020).
- [168] A. Al-Hilli and B. Evans, *The preparation and properties of transition metal dichalcogenide single crystals*, *Journal of Crystal Growth* **15**, 93–101 (1972).
- [169] W. Dawson and D. Bullett, *Electronic structure and crystallography of MoTe_2 and WTe_2* , *Journal of Physics C: Solid State Physics* **20**, 6159 (1987).
- [170] X. Zhang, S. Y. Teng, A. C. M. Loy, B. S. How, W. D. Leong, and X. Tao, *Transition metal dichalcogenides for the application of pollution reduction: A review*, *Nanomaterials* **10**, 1012 (2020).
- [171] H. Weyl, *Gravitation and the electron*, *Proceedings of the National Academy of Sciences* **15**, 323–334 (1929).

- [172] A. A. Burkov, *Topological semimetals*, Nature Materials **15**, 1145–1148 (2016).
- [173] S.-Y. Xu, I. Belopolski, N. Alidoust, M. Neupane, G. Bian, C. Zhang, R. Sankar, G. Chang, Z. Yuan, C.-C. Lee, S.-M. Huang, H. Zheng, J. Ma, D. S. Sanchez, B. Wang, A. Bansil, F. Chou, P. P. Shibayev, H. Lin, S. Jia, and M. Z. Hasan, *Discovery of a Weyl fermion semimetal and topological Fermi arcs*, Science (New York, N.Y.) **349**, 613–7 (2015).
- [174] F. C. Chen, H. Y. Lv, X. Luo, W. J. Lu, Q. L. Pei, G. T. Lin, Y. Y. Han, X. B. Zhu, W. H. Song, and Y. P. Sun, *Extremely large magnetoresistance in the type-II Weyl semimetal $MoTe_2$* , Physical Review B **94**, 235154 (2016).
- [175] S. Thirupathaiah, R. Jha, B. Pal, J. S. Matias, P. K. Das, P. K. Sivakumar, I. Vobornik, N. C. Plumb, M. Shi, R. A. Ribeiro, and D. D. Sarma, *$MoTe_2$: An uncompensated semimetal with extremely large magnetoresistance*, Physical Review B **95**, 241105 (2017).
- [176] J. Yang, J. Colen, J. Liu, M. C. Nguyen, G. wei Chern, and D. Louca, *Elastic and electronic tuning of magnetoresistance in $MoTe_2$* , Science Advances **3**, eaao4949 (2017).
- [177] M. N. Ali, J. Xiong, S. Flynn, J. Tao, Q. D. Gibson, L. M. Schoop, T. Liang, N. Hal-dolaarachchige, M. Hirschberger, N. P. Ong, and R. J. Cava, *Large, non-saturating magnetoresistance in WTe_2* , Nature **514**, 205–208 (2014).
- [178] Y. Wang, E. Liu, H. Liu, Y. Pan, L. Zhang, J. Zeng, Y. Fu, M. Wang, K. Xu, Z. Huang, Z. Wang, H. Z. Lu, D. Xing, B. Wang, X. Wan, and F. Miao, *Gate-tunable negative longitudinal magnetoresistance in the predicted type-II Weyl semimetal WTe_2* , Nature Communications **7**, 1–6 (2016).
- [179] E. Zhang, R. Chen, C. Huang, J. Yu, K. Zhang, W. Wang, S. Liu, J. Ling, X. Wan, H. Z. Lu, and F. Xiu, *Tunable Positive to Negative Magnetoresistance in Atomically Thin WTe_2* , Nano Letters **17**, 878–885 (2017).
- [180] J. X. Gong, J. Yang, M. Ge, Y. J. Wang, D. D. Liang, L. Luo, X. Yan, W. L. Zhen, S. R. Weng, L. Pi, C. J. Zhang, and W. K. Zhu, *Non-Stoichiometry Effects on the Extreme Magnetoresistance in Weyl Semimetal WTe_2* , Chinese Physics Letters **35**, 097101 (2018).

- [181] Y. Qi, P. G. Naumov, M. N. Ali, C. R. Rajamathi, W. Schnelle, O. Barkalov, M. Hanfland, S. C. Wu, C. Shekhar, Y. Sun, V. Süß, M. Schmidt, U. Schwarz, E. Pippel, P. Werner, R. Hillebrand, T. Förster, E. Kampert, S. Parkin, R. J. Cava, C. Felser, B. Yan, and S. A. Medvedev, *Superconductivity in Weyl semimetal candidate MoTe₂*, *Nature Communications* **7**, 1–7 (2016).
- [182] C. Heikes, I. L. Liu, T. Metz, C. Eckberg, P. Neves, Y. Wu, L. Hung, P. Piccoli, H. Cao, J. Leao, J. Paglione, T. Yildirim, N. P. Butch, and W. Ratcliff, *Mechanical control of crystal symmetry and superconductivity in Weyl semimetal MoTe₂*, *Physical Review Materials* **2**, 74202 (2018).
- [183] W. Wang, S. Kim, M. Liu, F. A. Cevallos, R. J. Cava, and N. P. Ong, *Evidence for an edge supercurrent in the Weyl superconductor MoTe₂*, *Science* **368**, 534–537 (2020).
- [184] P. Lu, J. S. Kim, J. Yang, H. Gao, J. Wu, D. Shao, B. Li, D. Zhou, J. Sun, D. Akinwande, D. Xing, and J. F. Lin, *Origin of superconductivity in the Weyl semimetal WTe₂ under pressure*, *Physical Review B* **94**, 224512 (2016).
- [185] Y. T. Chan, P. L. Alireza, K. Y. Yip, Q. Niu, K. T. Lai, and S. K. Goh, *Nearly isotropic superconductivity in the layered Weyl semimetal WTe₂ at 98.5 kbar*, *Physical Review B* **96**, 180504 (2017).
- [186] C. Huang, A. Narayan, E. Zhang, Y. Liu, X. Yan, J. Wang, C. Zhang, W. Wang, T. Zhou, C. Yi, S. Liu, J. Ling, H. Zhang, R. Liu, R. Sankar, F. Chou, Y. Wang, Y. Shi, K. T. Law, S. Sanvito, P. Zhou, Z. Han, and F. Xiu, *Inducing Strong Superconductivity in WTe₂ by a Proximity Effect*, *ACS Nano* **12**, 7185–7196 (2018).
- [187] Q. Li, C. He, Y. Wang, E. Liu, M. Wang, Y. Wang, J. Zeng, Z. Ma, T. Cao, C. Yi, N. Wang, K. Watanabe, T. Taniguchi, L. Shao, Y. Shi, X. Chen, S. J. Liang, Q. H. Wang, and F. Miao, *Proximity-Induced Superconductivity with Subgap Anomaly in Type II Weyl Semi-Metal WTe₂*, *Nano Letters* **18**, 7962–7968 (2018).
- [188] D. D. Liang, Y. J. Wang, W. L. Zhen, J. Yang, S. R. Weng, X. Yan, Y. Y. Han, W. Tong, W. K. Zhu, L. Pi, and C. J. Zhang, *Origin of planar Hall effect in type-II Weyl semimetal MoTe₂*, *AIP Advances* **9**, 055015 (2019).

- [189] P. Li, C. Zhang, Y. Wen, L. Cheng, G. Nichols, D. G. Cory, G. X. Miao, and X. X. Zhang, *Anisotropic planar Hall effect in the type-II topological Weyl semimetal WTe_2* , *Physical Review B* **100**, 205128 (2019).
- [190] B. Zhao, D. Khokhriakov, Y. Zhang, H. Fu, B. Karpiak, A. M. Hoque, X. Xu, Y. Jiang, B. Yan, and S. P. Dash, *Observation of charge to spin conversion in Weyl semimetal WTe_2 at room temperature*, *Physical Review Research* **2**, 13286 (2020).
- [191] R. A. John, J. Acharya, C. Zhu, A. Surendran, S. K. Bose, A. Chaturvedi, N. Tiwari, Y. Gao, Y. He, K. K. Zhang, M. Xu, W. L. Leong, Z. Liu, A. Basu, and N. Mathews, *Optogenetics inspired transition metal dichalcogenide neuristors for in-memory deep recurrent neural networks*, *Nature Communications* **11**, 3211 (2020).
- [192] X. J. Yan, Y. Y. Lv, L. Li, X. Li, S. H. Yao, Y. B. Chen, X. P. Liu, H. Lu, M. H. Lu, and Y. F. Chen, *Composition dependent phase transition and its induced hysteretic effect in the thermal conductivity of $W_xMo_{1-x}Te_2$* , *Applied Physics Letters* **110** (2017).
- [193] A. Crepaldi, G. Autès, A. Sterzi, G. Manzoni, M. Zacchigna, F. Cilento, I. Vobornik, J. Fujii, P. Bugnon, A. Magrez, H. Berger, F. Parmigiani, O. V. Yazyev, and M. Griioni, *Persistence of a surface state arc in the topologically trivial phase of $MoTe_2$* , *Physical Review B* **95**, 041408 (2017).
- [194] J. Jiang, Z. K. Liu, Y. Sun, H. F. Yang, C. R. Rajamathi, Y. P. Qi, L. X. Yang, C. Chen, H. Peng, C. C. Hwang, S. Z. Sun, S. K. Mo, I. Vobornik, J. Fujii, S. S. Parkin, C. Felser, B. H. Yan, and Y. L. Chen, *Signature of type-II Weyl semimetal phase in $MoTe_2$* , *Nature Communications* **8**, 1–6 (2017).
- [195] K. Deng, G. Wan, P. Deng, K. Zhang, S. Ding, E. Wang, M. Yan, H. Huang, H. H. Zhang, Z. Xu, J. Denlinger, A. Fedorov, H. Yang, W. Duan, H. Yao, Y. Wu, S. Fan, H. H. Zhang, X. Chen, and S. Zhou, *Experimental observation of topological Fermi arcs in type-II Weyl semimetal $MoTe_2$* , *Nature Physics* **12**, 1105–1110 (2016).
- [196] L. Huang, T. M. McCormick, M. Ochi, Z. Zhao, M. T. Suzuki, R. Arita, Y. Wu, D. Mou, H. Cao, J. Yan, N. Trivedi, and A. Kaminski, *Spectroscopic evidence for a type II Weyl semimetallic state in $MoTe_2$* , *Nature Materials* **15**, 1155–1160 (2016).

- [197] I. Belopolski, S. Y. Xu, Y. Ishida, X. Pan, P. Yu, D. S. Sanchez, H. Zheng, M. Neupane, N. Alidoust, G. Chang, T. R. Chang, Y. Wu, G. Bian, S. M. Huang, C. C. Lee, D. Mou, L. Huang, Y. Song, B. Wang, G. Wang, Y. W. Yeh, N. Yao, J. E. Rault, P. L. Fèvre, F. Bertran, H. T. Jeng, T. Kondo, A. Kaminski, H. Lin, Z. Liu, F. Song, S. Shin, and M. Z. Hasan, *Fermi arc electronic structure and Chern numbers in the type-II Weyl semimetal candidate $Mo_xW_{1-x}Te_2$* , Physical Review B **94**, 085127 (2016).
- [198] I. Belopolski, D. S. Sanchez, Y. Ishida, X. Pan, P. Yu, S. Y. Xu, G. Chang, T. R. Chang, H. Zheng, N. Alidoust, G. Bian, M. Neupane, S. M. Huang, C. C. Lee, Y. Song, H. Bu, G. Wang, S. Li, G. Eda, H. T. Jeng, T. Kondo, H. Lin, Z. Liu, F. Song, S. Shin, and M. Z. Hasan, *Discovery of a new type of topological Weyl fermion semimetal state in $Mo_xW_{1-x}Te_2$* , Nature Communications **7**, 1–9 (2016).
- [199] S. Jia, S.-Y. Xu, and M. Z. Hasan, *Weyl semimetals, Fermi arcs and chiral anomalies*, Nature Materials **15**, 1140–1144 (2016).
- [200] H. Zheng and M. Z. Hasan. *Quasiparticle interference on type-I and type-II weyl semimetal surfaces: A review*, (2018).
- [201] D. Puotinen and R. E. Newnham, *The crystal structure of $MoTe_2$* , Acta Crystallographica **14**, 691–692 (1961).
- [202] B. E. Brown, *The crystal structures of WTe_2 and high-temperature $MoTe_2$* , Acta Crystallographica **20**, 268–274 (1966).
- [203] R. Clarke, E. Marseglia, and H. P. Hughes, *A low-temperature structural phase transition in β - $MoTe_2$* , Philosophical Magazine B: Physics of Condensed Matter; Statistical Mechanics, Electronic, Optical and Magnetic Properties **38**, 121–126 (1978).
- [204] J. C. Park, S. J. Yun, H. Kim, J. H. Park, S. H. Chae, S. J. An, J. G. Kim, S. M. Kim, K. K. Kim, and Y. H. Lee, *Phase-Engineered Synthesis of Centimeter-Scale $1T'$ – and $2H$ –Molybdenum Ditelluride Thin Films*, ACS Nano **9**, 6548–6554 (2015).
- [205] T.-R. Chang, S.-Y. Xu, G. Chang, C.-C. Lee, S.-M. Huang, B. Wang, G. Bian, H. Zheng, D. S. Sanchez, I. Belopolski, N. Alidoust, M. Neupane, A. Bansil, H.-T.

- Jeng, H. Lin, and M. Z. Hasan, *Prediction of an arc-tunable Weyl Fermion metallic state in $Mo_xW_{1-x}Te_2$* , *Nature Communications* **7**, 10639 (2016).
- [206] A. N. Domozhirova, A. A. Makhnev, E. I. Shreder, S. V. Naumov, A. V. Lukoyanov, V. V. Chistyakov, J. C. A. Huang, A. A. Semiannikova, P. S. Korenistov, and V. V. Marchenkov, *Electronic properties of WTe_2 and $MoTe_2$ single crystals*, *Journal of Physics: Conference Series* **1389**, 012149 (2019).
- [207] S. M. Oliver, R. Beams, S. Krylyuk, I. Kalish, A. K. Singh, A. Bruma, F. Tavazza, J. Joshi, I. R. Stone, S. J. Stranick, A. V. Davydov, and P. M. Vora, *The structural phases and vibrational properties of $Mo_{1-x}W_xTe_2$ alloys*, *2D Materials* **4** (2017).
- [208] H. J. Kim, S. H. Kang, I. Hamada, and Y. W. Son, *Origins of the structural phase transitions in $MoTe_2$ and WTe_2* , *Physical Review B* **95**, 180101 (2017).
- [209] R. Dahal, L. Z. Deng, N. Poudel, M. Gooch, Z. Wu, H. C. Wu, H. D. Yang, C. K. Chang, and C. W. Chu, *Tunable structural phase transition and superconductivity in the Weyl semimetal $Mo_{1-x}W_xTe_2$* , *Physical Review B* **101**, 140505 (2020).
- [210] W. Thomson, *4. On a Mechanical Theory of Thermo-Electric Currents.*, *Proceedings of the Royal Society of Edinburgh* **3**, 91–98 (1857).
- [211] H. Reith, K. Nielsch, N. F. Hinsche, F. Rittweger, M. Hölzer, P. Zahn, A. Ernst, and I. Mertig. *Ab initio description of the thermoelectric properties of heterostructures in the diffusive limit of transport*, (2016).
- [212] F. Han, N. Andrejevic, T. Nguyen, V. Kozii, Q. T. Nguyen, T. Hogan, Z. Ding, R. Pablo-Pedro, S. Parjan, B. Skinner, A. Alatas, E. Alp, S. Chi, J. Fernandez-Baca, S. Huang, L. Fu, and M. Li, *Quantized thermoelectric Hall effect induces giant power factor in a topological semimetal*, *Nature Communications* **11**, 1–7 (2020).
- [213] H. Sakai, K. Ikeura, M. S. Bahramy, N. Ogawa, D. Hashizume, J. Fujioka, Y. Tokura, and S. Ishiwata, *Critical enhancement of thermopower in a chemically tuned polar semimetal $MoTe_2$* , *Science Advances* **2**, e1601378 (2016).

- [214] K. Ikeura, H. Sakai, M. S. Bahramy, and S. Ishiwata, *Rich structural phase diagram and thermoelectric properties of layered tellurides $\text{Mo}_{1-x}\text{Nb}_x\text{Te}_2$* , *APL Materials* **3**, 41514 (2015).
- [215] S. Paul, S. Karak, M. Mandal, A. Ram, S. Marik, R. P. Singh, and S. Saha, *Tailoring the phase transition and electron-phonon coupling in $1T'$ - MoTe_2 by charge doping: A Raman study*, *Physical Review B* **102**, 054103 (2020).
- [216] H. Takahashi, T. Akiba, K. Imura, T. Shiino, K. Deguchi, N. K. Sato, H. Sakai, M. S. Bahramy, and S. Ishiwata, *Anticorrelation between polar lattice instability and superconductivity in the Weyl semimetal candidate MoTe_2* , *Physical Review B* **95**, 100501 (2017).
- [217] H.-J. Noh, J. Jeong, E.-J. Cho, K. Kim, B. Min, and B.-G. Park, *Experimental realization of type-II Dirac fermions in a PdTe_2 superconductor*, *Physical review letters* **119**, 016401 (2017).
- [218] H. Huang, S. Zhou, and W. Duan, *Type-II Dirac fermions in the PtSe_2 class of transition metal dichalcogenides*, *Physical Review B* **94**, 121117 (2016).
- [219] F. Fei, X. Bo, R. Wang, B. Wu, J. Jiang, D. Fu, M. Gao, H. Zheng, Y. Chen, X. Wang, et al., *Nontrivial Berry phase and type-II Dirac transport in the layered material PdTe_2* , *Physical Review B* **96**, 041201 (2017).
- [220] B. Marfoua and J. Hong, *High thermoelectric performance in hexagonal 2D PdTe_2 monolayer at room temperature*, *ACS applied materials & interfaces* **11**, 38819–38827 (2019).
- [221] C. Liu, C.-S. Lian, M.-H. Liao, Y. Wang, Y. Zhong, C. Ding, W. Li, C.-L. Song, K. He, X.-C. Ma, et al., *Two-dimensional superconductivity and topological states in PdTe_2 thin films*, *Physical Review Materials* **2**, 094001 (2018).
- [222] H. Leng, C. Paulsen, Y. Huang, and A. De Visser, *Type-I superconductivity in the Dirac semimetal PdTe_2* , *Physical Review B* **96**, 220506 (2017).

- [223] J. Guo, Y. Zhang, S. Yue, C. Li, and Z. Wang, *Achieving significant enhancement of thermoelectric power factor of hexagonal PdTe₂ monolayer by using strain engineering*, *Journal of Physics and Chemistry of Solids* **181**, 111531 (2023).
- [224] S. Li, X. Zhang, and H. Bao, *Thermal transport by electrons and phonons in PdTe₂: an ab initio study*, *Physical Chemistry Chemical Physics* **23**, 5956–5962 (2021).
- [225] P. W. Bridgman. *Certain physical properties of single crystals of tungsten, antimony, bismuth, tellurium, cadmium, zinc, and tin*. In *Papers 32-58*, pages 1851–1932. Harvard University Press, (1964).
- [226] D. C. Stockbarger, *The production of large single crystals of lithium fluoride*, *Review of Scientific Instruments* **7**, 133–136 (1936).
- [227] A. F. May, J. Yan, and M. A. McGuire, *A practical guide for crystal growth of van der Waals layered materials*, *Journal of Applied Physics* **128** (2020).
- [228] S. Teknowijoyo, N. H. Jo, M. S. Scheurer, M. A. Tanatar, K. Cho, S. L. Bud'ko, P. P. Orth, P. C. Canfield, and R. Prozorov, *Nodeless superconductivity in the type-II Dirac semimetal PdTe₂: London penetration depth and pairing-symmetry analysis*, *Physical Review B* **98**, 024508 (2018).
- [229] Amit and Y. Singh, *Heat capacity evidence for conventional superconductivity in the type-II Dirac semimetal PdTe₂*, *Phys. Rev. B* **97**, 054515 (2018).
- [230] Y. Kumar, P. Sharma, M. Sharma, and V. Awana, *Investigation of structural and magneto-transport properties of PdTe₂ single crystals*, *Applied Physics A* **128**, 880 (2022).
- [231] S. Singh, V. Süß, M. Schmidt, C. Felser, and C. Shekhar, *Strong correlation between mobility and magnetoresistance in Weyl and Dirac semimetals*, *Journal of Physics: Materials* **3**, 024003 (2020).
- [232] M. N. Ali, J. Xiong, S. Flynn, J. Tao, Q. D. Gibson, L. M. Schoop, T. Liang, N. Hal-dolaarachchige, M. Hirschberger, N. P. Ong, et al., *Large, non-saturating magnetoresistance in WTe₂*, *Nature* **514**, 205–208 (2014).

- [233] T. Liang, Q. Gibson, M. N. Ali, M. Liu, R. Cava, and N. Ong, *Ultrahigh mobility and giant magnetoresistance in the Dirac semimetal Cd₃As₂*, *Nature materials* **14**, 280–284 (2015).
- [234] L. Morellon, J. Stankiewicz, B. Garcia-Landa, P. A. Algarabel, and M. R. Ibarra, *Giant magnetoresistance near the magnetostructural transition in Gd₅(Si_{1.8}Ge_{2.2})*, *Applied physics letters* **73**, 3462–3464 (1998).
- [235] V. Pecharsky, A. Holm, K. Gschneidner Jr, and R. Rink, *Massive Magnetic-Field-Induced Structural Transformation in Gd₅Ge₄ and the Nature of the Giant Magnetocaloric Effect*, *Physical review letters* **91**, 197204 (2003).
- [236] J. Liu, T. Gottschall, K. P. Skokov, J. D. Moore, and O. Gutfleisch, *Giant magnetocaloric effect driven by structural transitions*, *Nature materials* **11**, 620–626 (2012).
- [237] S. Mandal and T. K. Nath, *Magneto-structural transitions driven giant magnetocaloric effect in Ni₄₂Mn₄₃Cr₄Sn₁₁ Shape Memory Heusler Alloy near room temperature*, *Intermetallics* **162**, 108019 (2023).
- [238] D. Filippov, R. Levitin, A. Vasil'ev, T. Voloshok, H. Kageyama, and R. Suryanarayanan, *Spontaneous and field-induced magnetostructural transitions, giant magnetostriction, and specific heat in Ca_{0.85}Sm_{0.15}MnO₃*, *Physical Review B* **65**, 100404 (2002).
- [239] M. H. Kryder, E. C. Gage, T. W. McDaniel, W. A. Challener, R. E. Rottmayer, G. Ju, Y.-T. Hsia, and M. F. Erden, *Heat assisted magnetic recording*, *Proceedings of the IEEE* **96**, 1810–1835 (2008).
- [240] A. M. Tishin and Y. I. Spichkin, *The magnetocaloric effect and its applications*, CRC Press (2016).
- [241] M. Fallot. *Les alliages du fer avec les métaux de la famille du platine*. In *Annales de physique*, volume 11, pages 291–332, (1938).
- [242] A. Zakharov, A. Kadomtseva, R. Levitin, and E. Ponyatovskii, *Magnetic and magnetoelastic properties of a metamagnetic Iron-Rhodium alloy*, *Sov. Phys. JETP* **19**, 1348–1353 (1964).

- [243] C. Koenig, *Self-consistent band structure of paramagnetic, ferromagnetic and antiferromagnetic ordered FeRh*, Journal of Physics F: Metal Physics **12**, 1123 (1982).
- [244] A. Gray, D. Cooke, P. Krüger, C. Bordel, A. Kaiser, S. Moyerman, E. Fullerton, S. Ueda, Y. Yamashita, A. Gloskovskii, et al., *Electronic structure changes across the metamagnetic transition in FeRh via hard X-ray photoemission*, Physical review letters **108**, 257208 (2012).
- [245] M. Gruner, E. Hoffmann, and P. Entel, *Instability of the Rhodium magnetic moment as the origin of the metamagnetic phase transition in α -FeRh*, Physical Review B **67**, 064415 (2003).
- [246] L. M. Sandratskii and P. Mavropoulos, *Magnetic excitations and femtomagnetism of FeRh: A first-principles study*, Physical Review B **83**, 174408 (2011).
- [247] R. Gu and V. Antropov, *Dominance of the spin-wave contribution to the magnetic phase transition in FeRh*, Physical Review B **72**, 012403 (2005).
- [248] J. Barker and R. W. Chantrell, *Higher-order exchange interactions leading to metamagnetism in FeRh*, Physical Review B **92**, 094402 (2015).
- [249] K. Y. Guslienko, O. Chubykalo-Fesenko, O. Mryasov, R. Chantrell, and D. Weller, *Magnetization reversal via perpendicular exchange spring in FePt/FeRh bilayer films*, Physical Review B **70**, 104405 (2004).
- [250] P.-W. Huang and R. Victora, *Approaching the grain-size limit for jitter using FeRh/FePt in heat-assisted magnetic recording*, IEEE Transactions on Magnetics **50**, 1–4 (2014).
- [251] P. Kushwaha, P. Bag, and R. Rawat, *Room temperature giant baroresistance and magnetoresistance and its tunability in Pd doped FeRh*, Applied Physics Letters **106** (2015).
- [252] G. Brown, *Magnetic heat pumping near room temperature*, Journal of Applied Physics **47**, 3673–3680 (1976).
- [253] V. Franco, J. Blázquez, B. Ingale, and A. Conde, *The magnetocaloric effect and magnetic refrigeration near room temperature: materials and models*, Annual Review of Materials Research **42**, 305–342 (2012).

- [254] K. Kamenev, Z. Arnold, J. Kamarád, and N. Baranov, *Pressure induced antiferromagnetism in $(\text{Fe}_{1-x}\text{Ni}_x)_49\text{Rh}_{51}$ alloys*, Journal of alloys and compounds **252**, 1–5 (1997).
- [255] P. H. Walter, *Exchange inversion in ternary modifications of Iron Rhodium*, Journal of Applied Physics **35**, 938–939 (1964).
- [256] R. Barua, F. Jiménez-Villacorta, and L. Lewis, *Predicting magnetostructural trends in FeRh-based ternary systems*, Applied Physics Letters **103** (2013).
- [257] N. Baranov and E. Barabanova, *Electrical resistivity and magnetic phase transitions in modified FeRh compounds*, Journal of Alloys and Compounds **219**, 139–148 (1995).
- [258] A. Ceballos, Z. Chen, O. Schneider, C. Bordel, L.-W. Wang, and F. Hellman, *Effect of strain and thickness on the transition temperature of epitaxial FeRh thin-films*, Applied Physics Letters **111** (2017).
- [259] Y. Kobayashi, K. Muta, and K. Asai, *The Hall effect and thermoelectric power correlated with the giant magnetoresistance in modified FeRh compounds*, Journal of Physics: Condensed Matter **13**, 3335 (2001).
- [260] T. Yamauchi, Y. Hamada, Y. Kurokawa, and H. Yuasa, *Anomalous Nernst effect dependence on composition in $\text{Fe}_{100-x}\text{Rh}_x$ alloys*, Japanese journal of applied physics **61**, SC1019 (2022).
- [261] I. Gray, G. M. Stiehl, J. T. Heron, A. B. Mei, D. G. Schlom, R. Ramesh, D. C. Ralph, and G. D. Fuchs, *Imaging uncompensated moments and exchange-biased emergent ferromagnetism in FeRh thin films*, Physical Review Materials **3**, 124407 (2019).
- [262] H. Saglam, C. Liu, Y. Li, J. Sklenar, J. Gibbons, D. Hong, V. Karakas, J. E. Pearson, O. Ozatay, W. Zhang, et al., *Anomalous Hall and Nernst Effects in FeRh*, arXiv preprint arXiv:2012.14383 (2020).
- [263] S. Bennett, A. Herklotz, C. Cress, A. Ievlev, C. Rouleau, I. Mazin, and V. Lauter, *Magnetic order multilayering in FeRh thin films by He-Ion irradiation*, Materials Research Letters **6**, 106–112 (2018).

- [264] C. D. Cress, D. Wickramaratne, M. R. Rosenberger, Z. Hennighausen, P. G. Callahan, S. W. LaGasse, N. Bernstein, O. M. van't Erve, B. T. Jonker, S. B. Qadri, et al., *Direct-write of nanoscale domains with tunable metamagnetic order in FeRh thin films*, ACS Applied Materials & Interfaces **13**, 836–847 (2020).
- [265] C. D. Cress, O. van't Erve, J. Prestigiacomo, S. W. LaGasse, A. Glavic, V. Lauter, and S. P. Bennett, *Domain state exchange bias in a single layer FeRh thin film formed via low energy ion implantation*, Journal of Materials Chemistry C **11**, 903–909 (2023).
- [266] S. P. Bennett, S. W. LaGasse, M. Currie, O. V. Erve, J. C. Prestigiacomo, C. D. Cress, and S. B. Qadri, *N⁺ irradiation and substrate-induced variability in the metamagnetic phase transition of FeRh films*, Coatings **11**, 661 (2021).
- [267] T. Goto, H. Ogata, T. Sato, K. Yamaguchi, T. Shima, and H. Yoshida, *Growth of FeRh thin films and magnetic properties of FePt/FeRh bilayers*, Journal of Magnetism and Magnetic Materials **272**, E791–E792 (2004).
- [268] Y. Ohtani and I. Hatakeyama, *Features of broad magnetic transition in FeRh thin film*, Journal of magnetism and magnetic materials **131**, 339–344 (1994).
- [269] G. Kresse and J. Furthmüller, *Efficiency of Ab-initio total energy calculations for metals and semiconductors using a plane-wave basis set*, Computational materials science **6**, 15–50 (1996).
- [270] G. Kresse and J. Hafner, *Ab initio molecular dynamics for liquid metals*, Physical review B **47**, 558 (1993).
- [271] G. Kresse and J. Furthmüller, *Efficient iterative schemes for Ab initio total-energy calculations using a plane-wave basis set*, Physical review B **54**, 11169 (1996).
- [272] G. Kresse and D. Joubert, *From ultrasoft pseudopotentials to the projector augmented-wave method*, Physical review b **59**, 1758 (1999).
- [273] J. P. Perdew, K. Burke, and M. Ernzerhof, *Generalized gradient approximation made simple*, Physical review letters **77**, 3865 (1996).
- [274] M. J. Jiménez, A. B. Schvval, and G. F. Cabeza, *Ab initio study of FeRh alloy properties*, Computational Materials Science **172**, 109385 (2020).

- [275] H. Takahashi, M. Araidai, S. Okada, and K. Shiraishi, *Theoretical Investigation on Electronic and Magnetic Structures of FeRh*, *Journal of the Magnetism Society of Japan* **40**, 77–80 (2016).
- [276] M. Wolloch, M. E. Gruner, W. Keune, P. Mohn, J. Redinger, F. Hofer, D. Suess, R. Podloucky, J. Landers, S. Salamon, et al., *Impact of lattice dynamics on the phase stability of metamagnetic FeRh: Bulk and thin films*, *Physical Review B* **94**, 174435 (2016).
- [277] R. M. Vieira, O. Eriksson, A. Bergman, and H. C. Herper, *High-throughput compatible approach for entropy estimation in magnetocaloric materials: FeRh as a test case*, *Journal of Alloys and Compounds* **857**, 157811 (2021).
- [278] B. Himmetoglu, A. Floris, S. De Gironcoli, and M. Cococcioni, *Hubbard-corrected DFT energy functionals: The LDA+U description of correlated systems*, *International Journal of Quantum Chemistry* **114**, 14–49 (2014).
- [279] E. R. Ylvisaker, W. E. Pickett, and K. Koepf, *Anisotropy and magnetism in the LSDA+U method*, *Physical Review B* **79**, 035103 (2009).
- [280] J. Kouvel and C. Hartelius, *Anomalous magnetic moments and transformations in the ordered alloy FeRh*, *Journal of Applied Physics* **33**, 1343–1344 (1962).
- [281] L. Lewis, C. Marrows, and S. Langridge, *Coupled magnetic, structural, and electronic phase transitions in FeRh*, *Journal of Physics D: Applied Physics* **49**, 323002 (2016).
- [282] I. Radu, C. Stamm, N. Pontius, T. Kachel, P. Ramm, J.-U. Thiele, H. Dürr, and C. Back, *Laser-induced generation and quenching of magnetization on FeRh studied with time-resolved X-ray magnetic circular dichroism*, *Physical Review B* **81**, 104415 (2010).
- [283] G. Shirane, C. Chen, P. Flinn, and R. Nathans, *Hyperfine fields and magnetic moments in the Fe-Rh system*, *Journal of Applied Physics* **34**, 1044–1045 (1963).
- [284] G. Shirane, R. Nathans, and C. Chen, *Magnetic moments and unpaired spin densities in the Fe-Rh alloys*, *Physical Review* **134**, A1547 (1964).

- [285] S. Roy, G. Perkins, M. Chattopadhyay, A. Nigam, K. Sokhey, P. Chaddah, A. Caplin, and L. Cohen, *First order magnetic transition in doped CeFe₂ alloys: Phase coexistence and metastability*, *Physical review letters* **92**, 147203 (2004).
- [286] N. F. Mott and E. A. Davis, *Electronic processes in non-crystalline materials*, Oxford university press (2012).
- [287] D. W. Cooke, F. Hellman, C. Baldasseroni, C. Bordel, S. Moyerman, and E. Fullerton, *Thermodynamic measurements of Fe-Rh alloys*, *Physical review letters* **109**, 255901 (2012).
- [288] N. Pérez, A. Chirkova, K. P. Skokov, T. G. Woodcock, O. Gutfleisch, N. V. Baranov, K. Nielsch, and G. Schierning, *Electronic entropy change in Ni-doped FeRh*, *Materials Today Physics* **9**, 100129 (2019).
- [289] M. Belov, A. Syzdykova, and I. Abrikosov, *Temperature-dependent lattice dynamics of antiferromagnetic and ferromagnetic phases of FeRh*, *Physical Review B* **101**, 134303 (2020).
- [290] A. M. Dehkordi, M. Zebarjadi, J. He, and T. M. Tritt, *Thermoelectric power factor: Enhancement mechanisms and strategies for higher performance thermoelectric materials*, *Materials Science and Engineering: R: Reports* **97**, 1–22 (2015).
- [291] M. Zebarjadi, K. Esfarjani, M. Dresselhaus, Z. Ren, and G. Chen, *Perspectives on thermoelectrics: from fundamentals to device applications*, *Energy & Environmental Science* **5**, 5147–5162 (2012).
- [292] W. Thomson, *4. on a mechanical theory of thermo-electric currents*, *Proceedings of the Royal society of Edinburgh* **3**, 91–98 (1857).
- [293] W. Thomson, *IX.—On the dynamical theory of heat. Part V. Thermoelectric currents*, *Earth and Environmental Science Transactions of The Royal Society of Edinburgh* **21**, 123–171 (1857).
- [294] T. Chiba, R. Iguchi, T. Komine, Y. Hasegawa, and K.-i. Uchida, *Temperature profile of the Thomson-effect-induced heat release/absorption in junctionless single conductors*, *Japanese Journal of Applied Physics* **62**, 037001 (2023).

- [295] M. Loving, R. Barua, C. Le Graët, C. Kinane, D. Heiman, S. Langridge, C. Marrows, and L. Lewis, *Strain-tuning of the magnetocaloric transition temperature in model FeRh films*, *Journal of Physics D: Applied Physics* **51**, 024003 (2017).
- [296] I. Fina and J. Fontcuberta, *Strain and voltage control of magnetic and electric properties of FeRh films*, *Journal of Physics D: Applied Physics* **53**, 023002 (2019).
- [297] H. Kumar, D. R. Cornejo, S. L. Morelhao, S. Kycia, I. Montellano, N. R. Alvarez, G. Alejandro, and A. Butera, *Strain effects on the magnetic order of epitaxial FeRh thin films*, *Journal of Applied Physics* **124** (2018).
- [298] D. J. Keavney, Y. Choi, M. V. Holt, V. Uhlíř, D. Arena, E. E. Fullerton, P. J. Ryan, and J.-W. Kim, *Phase coexistence and kinetic arrest in the magnetostructural transition of the ordered alloy FeRh*, *Scientific reports* **8**, 1778 (2018).
- [299] J. A. Arregi, O. Caha, and V. Uhlíř, *Evolution of strain across the magnetostructural phase transition in epitaxial FeRh films on different substrates*, *Physical Review B* **101**, 174413 (2020).
- [300] S. Maat, J.-U. Thiele, and E. E. Fullerton, *Temperature and field hysteresis of the antiferromagnetic-to-ferromagnetic phase transition in epitaxial FeRh films*, *Physical Review B* **72**, 214432 (2005).
- [301] L. E. Bell, *Cooling, Heating, Generating Power, and Recovering Waste Heat with Thermoelectric Systems*, *Science* **321**, 1457–1461 (2008).
- [302] X. Gou, H. Xiao, and S. Yang, *Modeling, experimental study and optimization on low-temperature waste heat thermoelectric generator system*, *Applied Energy* **87**, 3131–3136 (2010).
- [303] J. Yang. *Potential applications of thermoelectric waste heat recovery in the automotive industry*. In *International Conference on Thermoelectrics, ICT, Proceedings*, volume 2005, pages 170–174. Institute of Electrical and Electronics Engineers Inc., (2005).
- [304] S. Kumar, S. D. Heister, X. Xu, J. R. Salvador, and G. P. Meisner, *Thermoelectric generators for automotive waste heat recovery systems part I: Numerical modeling and baseline model analysis*, *Journal of Electronic Materials* **42**, 665–674 (2013).

- [305] W. Wu, N. P. Ong, and P. M. Chaikin, *Giant angular-dependent Nernst effect in the quasi-one-dimensional organic conductor (TMTSF)₂PF₆*, Phys. Rev. B **72**, 235116 (2005).
- [306] E. S. Choi, J. S. Brooks, H. Kang, Y. J. Jo, and W. Kang, *Resonant Nernst Effect in the Metallic and Field-Induced Spin Density Wave States of (TMTSF)₂ClO₄*, Phys. Rev. Lett. **95**, 187001 (2005).
- [307] M. S. Nam, C. Mézière, P. Batail, L. Zorina, S. Simonov, and A. Ardavan, *Superconducting fluctuations in organic molecular metals enhanced by Mott criticality*, Scientific Reports **3**, 1–6 (2013).
- [308] W. Wu, I. J. Lee, and P. M. Chaikin, *Giant Nernst Effect and Lock-In Currents at Magic Angles in (TMTSF)₂PF₆*, Phys. Rev. Lett. **91**, 056601 (2003).
- [309] S. Tsuchiya, J.-i. Yamada, S. Tanda, K. Ichimura, T. Terashima, N. Kurita, K. Kodama, and S. Uji, *Fluctuating superconductivity in the strongly correlated two-dimensional organic superconductor κ -(BEDT-TTF)₂Cu(NCS)₂ in an in-plane magnetic field*, Phys. Rev. B **85**, 220506 (2012).
- [310] M. S. Nam, A. Ardavan, S. J. Blundell, and J. A. Schlueter, *Fluctuating superconductivity in organic molecular metals close to the Mott transition*, Nature **449**, 584–587 (2007).
- [311] J. Wei, L. Yang, Z. Ma, P. Song, M. Zhang, J. Ma, F. Yang, and X. Wang, *Review of current high-ZT thermoelectric materials*, Journal of Materials Science **55**, 12642–12704 (2020).
- [312] J. L. Lan, Y. C. Liu, B. Zhan, Y. H. Lin, B. Zhang, X. Yuan, W. Zhang, W. Xu, and C. W. Nan, *Enhanced thermoelectric properties of Pb-doped BiCuSeO ceramics*, Advanced Materials **25**, 5086–5090 (2013).
- [313] S. Butt, M. U. Farooq, W. Mahmood, S. Salam, M. Sultan, M. A. Basit, J. Ma, Y. Lin, and C. W. Nan, *One-step rapid synthesis of Cu₂Se with enhanced thermoelectric properties*, Journal of Alloys and Compounds **786**, 557–564 (2019).

- [314] C. Zhang, M. de la Mata, Z. Li, F. J. Belarre, J. Arbiol, K. A. Khor, D. Poletti, B. Zhu, Q. Yan, and Q. Xiong, *Enhanced thermoelectric performance of solution-derived bismuth telluride based nanocomposites via liquid-phase sintering*, *Nano Energy* **30**, 630–638 (2016).
- [315] N. K. Singh, J. Pandey, S. Acharya, and A. Soni, *Charge carriers modulation and thermoelectric performance of intrinsically p-type Bi_2Te_3 by Ge doping*, *Journal of Alloys and Compounds* **746**, 350–355 (2018).
- [316] W. Wei, C. Chang, T. Yang, J. Liu, H. Tang, J. Zhang, Y. Li, F. Xu, Z. Zhang, J. F. Li, and G. Tang, *Achieving High Thermoelectric Figure of Merit in Polycrystalline SnSe via Introducing Sn Vacancies*, *Journal of the American Chemical Society* **140**, 499–505 (2018).
- [317] H. Wang and C. Yu, *Organic Thermoelectrics: Materials Preparation, Performance Optimization, and Device Integration*, *Joule* **3**, 53–80 (2019).
- [318] C. Yu, Y. S. Kim, D. Kim, and J. C. Grunlan, *Thermoelectric Behavior of Segregated-Network Polymer Nanocomposites*, *Nano Letters* **8**, 4428–4432 (2008).
- [319] D. Kim, Y. Kim, K. Choi, J. C. Grunlan, and C. Yu, *Improved Thermoelectric Behavior of Nanotube-Filled Polymer Composites with Poly(3,4-ethylenedioxythiophene) Poly(styrenesulfonate)*, *ACS Nano* **4**, 513–523 (2010).
- [320] O. Bubnova, Z. U. Khan, A. Malti, S. Braun, M. Fahlman, M. Berggren, and X. Crispin, *Optimization of the thermoelectric figure of merit in the conducting polymer poly(3,4-ethylenedioxythiophene)*, *Nature Materials* **10**, 429–433 (2011).
- [321] G.-H. Kim, L. Shao, K. Zhang, and K. P. Pipe, *Engineered doping of organic semiconductors for enhanced thermoelectric efficiency*, *Nature Materials* **12**, 719–723 (2013).
- [322] H. Wang, J.-H. Hsu, S.-I. Yi, S. L. Kim, K. Choi, G. Yang, and C. Yu, *Thermally Driven Large N-Type Voltage Responses from Hybrids of Carbon Nanotubes and Poly(3,4-ethylenedioxythiophene) with Tetrakis(dimethylamino)ethylene*, *Advanced Materials* **27**, 6855–6861 (2015).

- [323] W. Zhou, Q. Fan, Q. Zhang, L. Cai, K. Li, X. Gu, F. Yang, N. Zhang, Y. Wang, H. Liu, W. Zhou, and S. Xie, *High-performance and compact-designed flexible thermoelectric modules enabled by a reticulate carbon nanotube architecture*, *Nature Communications* **8**, 14886 (2017).
- [324] C. Cho, K. L. Wallace, P. Tzeng, J.-H. Hsu, C. Yu, and J. C. Grunlan, *Outstanding Low Temperature Thermoelectric Power Factor from Completely Organic Thin Films Enabled by Multidimensional Conjugated Nanomaterials*, *Advanced Energy Materials* **6**, 1502168 (2016).
- [325] C. Cho, B. Stevens, J. Hsu, R. Bureau, D. A. Hagen, O. Regev, C. Yu, and J. C. Grunlan, *Completely Organic Multilayer Thin Film with Thermoelectric Power Factor Rivaling Inorganic Tellurides*, *Advanced Materials* **27**, 2996–3001 (2015).
- [326] L. Müller, S.-Y. Rhim, V. Sivanesan, D. Wang, S. Hietzschold, P. Reiser, E. Mankel, S. Beck, S. Barlow, S. R. Marder, A. Pucci, W. Kowalsky, and R. Lovrincic, *Electric-Field-Controlled Dopant Distribution in Organic Semiconductors*, *Advanced Materials* **29**, 1701466 (2017).
- [327] J. Li, C. W. Rochester, I. E. Jacobs, E. W. Aasen, S. Friedrich, P. Stroeve, and A. J. Moulé, *The effect of thermal annealing on dopant site choice in conjugated polymers*, *Organic Electronics* **33**, 23–31 (2016).
- [328] L. Yu, D. Scheunemann, A. Lund, D. Kiefer, and C. Müller, *Sequential doping of solid chunks of a conjugated polymer for body-heat-powered thermoelectric modules*, *Applied Physics Letters* **119**, 181902 (2021).
- [329] L. Yu, E. Pavlica, R. Li, Y. Zhong, C. Silva, G. Bratina, C. Müller, A. Amassian, and N. Stingelin, *Conjugated Polymer Mesocrystals with Structural and Optoelectronic Coherence and Anisotropy in Three Dimensions*, *Advanced Materials* **34**, 2103002 (2022).
- [330] A. Hamidi-Sakr, L. Biniek, J. L. Bantignies, D. Maurin, L. Herrmann, N. Leclerc, P. Lévêque, V. Vijayakumar, N. Zimmermann, and M. Brinkmann, *A Versatile Method to Fabricate Highly In-Plane Aligned Conducting Polymer Films with Anisotropic Charge Transport and Thermoelectric Properties: The Key Role of Alkyl Side Chain Layers on the Doping Mechanism*, *Advanced Functional Materials* **27**, 1700173 (2017).

- [331] E. Jang, A. Poosapati, and D. Madan, *Enhanced Thermoelectric Properties of F4TCNQ Doped P3HT and Its Use as a Binder for Sb₂Te₃ Based Printed Thermoelectric Films*, ACS Applied Energy Materials **1**, 1455–1462 (2018).
- [332] E. Lim, K. A. Peterson, G. M. Su, and M. L. Chabynyc, *Thermoelectric Properties of Poly(3-hexylthiophene) (P3HT) Doped with 2,3,5,6-Tetrafluoro-7,7,8,8-tetracyanoquinodimethane (F4TCNQ) by Vapor-Phase Infiltration*, Chemistry of Materials **30**, 998–1010 (2018).
- [333] D. Kiefer, R. Kroon, A. I. Hofmann, H. Sun, X. Liu, A. Giovannitti, D. Stegerer, A. Cano, J. Hynynen, L. Yu, Y. Zhang, D. Nai, T. F. Harrelson, M. Sommer, A. J. Moulé, M. Kemerink, S. R. Marder, I. McCulloch, M. Fahlman, S. Fabiano, and C. Müller, *Double doping of conjugated polymers with monomer molecular dopants*, Nature Materials **18**, 149–155 (2019).
- [334] M. Hamid Elsheikh, D. A. Shnawah, M. F. M. Sabri, S. B. M. Said, M. Haji Hassan, M. B. Ali Bashir, and M. Mohamad. *A review on thermoelectric renewable energy: Principle parameters that affect their performance*, (2014).
- [335] R. P. CHASMAR and R. STRATTON, *The Thermoelectric Figure of Merit and its Relation to Thermoelectric Generatorst*, Journal of Electronics and Control **7**, 52–72 (1959).
- [336] A. Mehdizadeh Dehkordi, M. Zebarjadi, J. He, and T. M. Tritt. *Thermoelectric power factor: Enhancement mechanisms and strategies for higher performance thermoelectric materials*, (2015).
- [337] J. O. Sofo and G. D. Mahan, *Optimum band gap of a thermoelectric material*, Physical Review B **49**, 4565–4570 (1994).
- [338] R. Noriega, J. Rivnay, K. Vandewal, F. P. V. Koch, N. Stingelin, P. Smith, M. F. Toney, and A. Salleo, *A general relationship between disorder, aggregation and charge transport in conjugated polymers*, Nature Materials **12**, 1038–1044 (2013).
- [339] R. Schmechel, *Hopping transport in doped organic semiconductors: A theoretical approach and its application to p-doped zinc-phthalocyanine*, Journal of Applied Physics **93**, 4653–4660 (2003).

- [340] A. M. Glauddell, J. E. Cochran, S. N. Patel, and M. L. Chabiny, *Impact of the doping method on conductivity and thermopower in semiconducting polythiophenes*, *Advanced Energy Materials* **5**, 1401072 (2015).
- [341] D. T. Scholes, P. Y. Yee, J. R. Lindemuth, H. Kang, J. Onorato, R. Ghosh, C. K. Luscombe, F. C. Spano, S. H. Tolbert, and B. J. Schwartz, *The Effects of Crystallinity on Charge Transport and the Structure of Sequentially Processed F4TCNQ-Doped Conjugated Polymer Films*, *Advanced Functional Materials* **27**, 1702654 (2017).
- [342] D. L. Young, J. F. Geisz, and T. J. Coutts, *Nitrogen-induced decrease of the electron effective mass in $GaAs_{1-x}N_x$ thin films measured by thermomagnetic transport phenomena*, *Applied Physics Letters* **82**, 1236–1238 (2003).
- [343] B. Wei, J. Zhang, P. Sun, W. Wang, N. Wang, and F. Steglich, *Nernst effect of the intermediate valence compound $YbAl_3$: revisiting the thermoelectric properties*, *Journal of Physics: Condensed Matter* **27**, 105601 (2015).
- [344] E. Miller, M. Jones, M. Henry, P. Chery, K. Miller, and E. Jankowski, *Optimization and Validation of Efficient Models for Predicting Polythiophene Self-Assembly*, *Polymers* **10**, 1305 (2018).
- [345] S. Hiura, N. Okada, J. Wakui, H. Narita, S. Kanehashi, and T. Shimomura, *Thermoelectric Properties of Poly(3-Hexylthiophene) Nanofiber Mat with a Large Void Fraction*, *Materials* **10**, 468 (2017).
- [346] D. Scheunemann, V. Vijayakumar, H. Zeng, P. Durand, N. Leclerc, M. Brinkmann, and M. Kemerink, *Rubbing and Drawing: Generic Ways to Improve the Thermoelectric Power Factor of Organic Semiconductors?*, *Advanced Electronic Materials* **6**, 2000218 (2020).
- [347] J. C. Duda, P. E. Hopkins, Y. Shen, and M. C. Gupta, *Thermal transport in organic semiconducting polymers*, *Applied Physics Letters* **102**, 251912 (2013).
- [348] C. Bounioux, P. Díaz-Chao, M. Campoy-Quiles, M. S. Martín-González, A. R. Goñi, R. Yerushalmi-Rozen, and C. Müller, *Thermoelectric composites of poly(3-*

- hexylthiophene*) and carbon nanotubes with a large power factor, *Energy and Environmental Science* **6**, 918–925 (2013).
- [349] V. Linseis, Z. M. Hassan, H. Reith, J. Garcia, K. Nielsch, H. Baumgart, E. Redel, and P. Woias, *Complete Thermoelectric Characterization of PEDOT:PSS Thin Films with a Novel ZT Test Chip Platform*, *physica status solidi (a)* **215**, 1700930 (2018).
- [350] Q. Jiang, C. Liu, D. Zhu, H. Song, J. Xu, H. Shi, D. Mo, Z. Wang, and Z. Zhu, *Simultaneous Enhancement of the Electrical Conductivity and Seebeck Coefficient of PEDOT-block-PEG/SWCNTs Nanocomposites*, *Journal of Electronic Materials* **44**, 1585–1591 (2015).
- [351] C. Liu, J. Xu, B. Lu, R. Yue, and F. Kong, *Simultaneous Increases in Electrical Conductivity and Seebeck Coefficient of PEDOT:PSS Films by Adding Ionic Liquids into a Polymer Solution*, *Journal of Electronic Materials* **41**, 639–645 (2012).